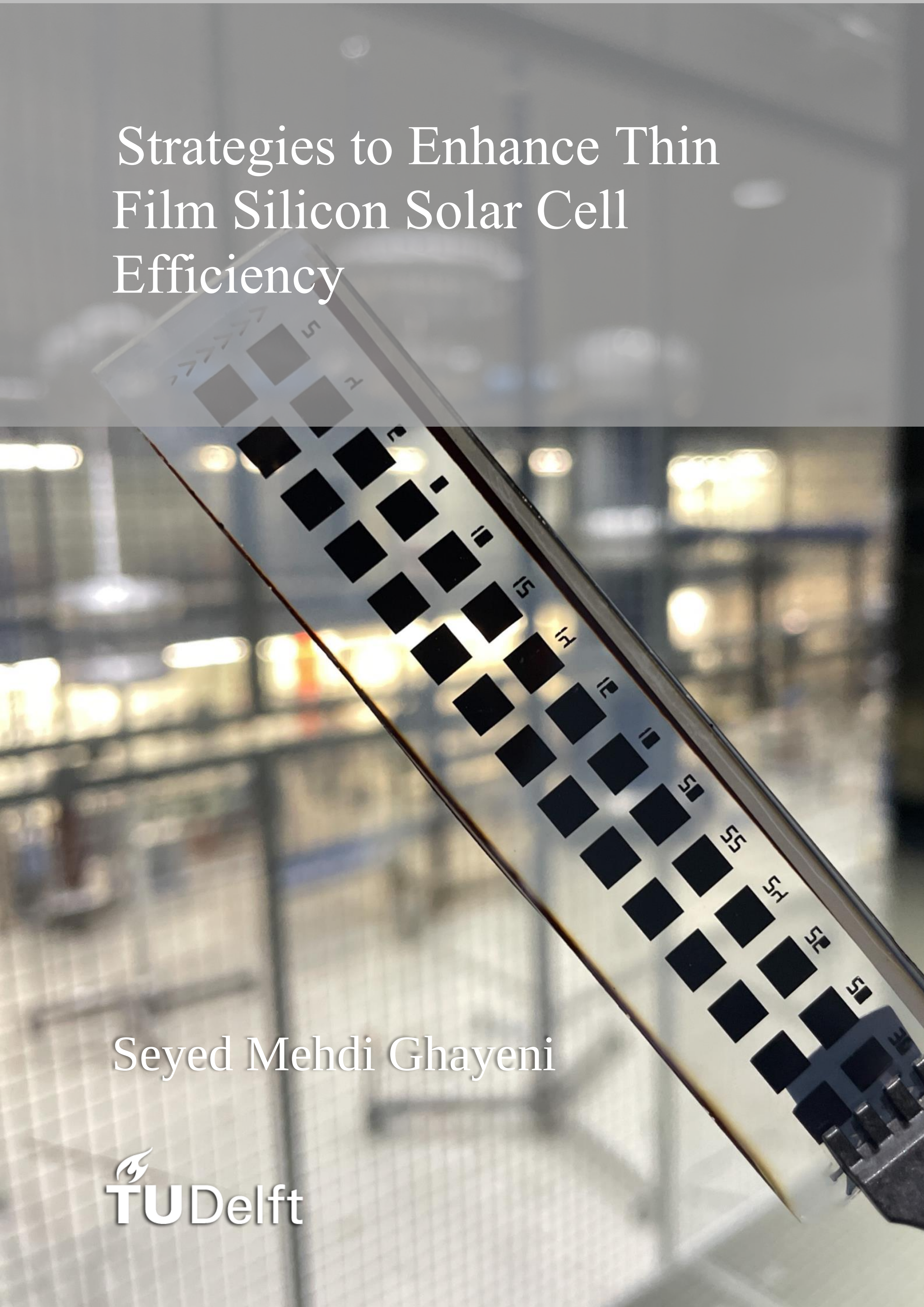

Strategies to Enhance Thin Film Silicon Solar Cell Efficiency

Seyed Mehdi Ghayeni

Strategies to Enhance Thin Film Silicon Solar Cell Efficiency

Thesis report by

Seyed Mehdi Ghayeni

to obtain the degree of

Master of Science

in Sustainable Energy Technology

at the Delft University of Technology,
to be defended publicly on August 17, 2023 at 03:00 PM.

Student number: 5652871

Thesis committee: Prof. dr. A. H. M Smets, TU Delft, ESE- PVMD, Supervisor
Dr. ir. R. Santbergen, TU Delft, ESE- PVMD, Assistant Professor
Dr. ir. Hani Vahedi, TU Delft, ESE- DCES, Assistant Professor
Ir. Govind Padmakumar, TU Delft, ESE- PVMD, Supervisor

Abstract

Thin-film silicon solar cells are an innovative approach to utilizing solar energy. Thanks to their flexibility, lower material usage, and production cost, they have the potential to be used in a range of applications. The conversion efficiencies of thin-film silicon solar cells need to be improved to make them commercially viable. This involves further optimizing the different layers of the solar cells. During this project, different strategies for enhancing thin film silicon solar cells were studied, including the deposition conditions for nc-Si:H layer, the sacrificial texturing used, the use of an additional back reflector layer, and the type of TCO layer used.

A more consistent quality of the nc-Si:H samples were obtained by varying the hydrogen flow rate compared to the silane flow rate in the processing chamber. Using a silane flow rate of 2.3 sccm and a hydrogen flow rate of 120 sccm, a silane concentration 2.6 was achieved, resulting in nc-Si:H layer with a crystallinity of 60%, close to the desired amorphous-nanocrystalline silicon transition region.

The texturing used in the glass sample can play a significant role in scattering the incident light into the solar cell. Craters of different sizes are formed depending on the material used for the sacrificial layer. Making smaller craters on top of larger craters using modulated surface textures (MST) is also possible. Using intrinsic Zinc Oxide (i-ZnO) sacrificial texturing resulted in the highest spectral utilization in single junction nc-Si: H with a Jsc of 25.2 mA/cm^2. Indium-doped tin oxide (ITO) sacrificial texturing created micro-sized textures, resulting in the highest spectral utilization in micromorph samples (Jsc of 24.6 mA/cm^2). Using an MST of ITO and i-ZnO also resulted in high spectral utilization with a Jsc of 24.3 mA/cm^2 in micromorph cells.

Having an additional back reflector on top of the metal back contact can further improve photon absorption in solar cells. Using a material with a low refractive index, such as i-ZnO, increased the spectral utilization and improved the short-circuit current (Jsc) by approximately 10%. Depositing the i-ZnO back reflector layer using a higher heater temperature (300°C), improved the spectral utilization of the sample further by 9%.

The transparent conductive oxide (TCO) layer must be highly transparent and conductive. Usually, ITO is used as a TCO layer, although it has limited absorption in the infrared region and lower conductivity at higher temperatures. A TCO with higher optoelectrical properties was obtained using a bilayer of hydrogenated indium oxide (IOH) and i-ZnO. nc-Si:H samples with the TCO bilayer showed a higher spectral utilization and an improvement in their Jsc by 9-12%. The performance of micromorph samples with TCO bilayer was also higher with Jsc improvement of 6%. The influence of the bilayer thickness on the performance of micromorph samples was also inspected, and it was found that using a thicker bilayer with a thickness of 1100 nm instated of 600nm boosted the performance of the sample further and improved its Jsc by 3%.

Acknowledgement

I want to begin by expressing my gratitude for the amazing opportunity that I had working on an innovative technology like thin film silicon solar cells with all its challenges and rewards. After spending the past nine months working on the different strategies for optimizing the efficiency of the various layers in thin-film silicon solar cells, I found some interesting results, which I hope will contribute to further research in the academic community. Doing a master's degree at TUdelft was an eye-opening experience as I discovered my passion for solar energy through this program, which I see myself pursuing in my future career.

Firstly, I begin by thanking Allah (god) for all the blessings and guidance that I have been offered in life. Without my faith, I would not have found my purpose and happiness in life. Next, I want to thank my parents and family from the depth of my heart for the continuous support, love, and care they provided me along the journey. Without them, I would not have made it this far in life, and my childhood dream of studying abroad would not have become a reality. They believed in me and supported me during the most challenging times of my life, and ensured I pushed myself and never gave up. I am beyond grateful to be able to thank you in my Master's thesis, and I will make sure that one day I pay you back.

Special thanks to the most enthusiastic professor Dr. Arno Smets for the knowledge and the useful discussions that we had. It was indeed a pleasure working under your supervision, and I am glad that I was introduced to this thesis topic during the Master's thesis event. I want to express my sincere gratitude to my daily supervisor Govind Padmakumar for the guidance and support throughout this project. Your passion for the topic made it exciting to work on this project and carry out experiments. Special thanks to Paula Perez for the useful insights and skills that helped me during this project. Also, thanks to Federica Saitta for her expertise and patience in helping me take the SEM images. Not to forget, thanks to the guardian angles Martijn Tijssen and Stefaan Heirman who helped countless times when the machines in the EKL and ESP lab did not function properly. Special mention to my amazing colleagues and friends Shriram, Tristian, Shloka, Matthais, Salem, Devansh, and many more for making my time at TUdelft memorable and making this thesis much more enjoyable.

Lastly, special thanks to special people in my life - Ali Solyemani, Nasser al Muttahar, Mohammed Kadhim, Mohammed al Khamis, Ali Warraq, and Hussain al Naqeeb. Your presence in my life is truly a blessing, and am beyond grateful to know you.

Contents

Chapter 1: Introduction *1*

Chapter 2: Fundamentals *3*

2.1 The working principle of a solar cell 3

2.2 Thin-film silicon solar cells 4
- Hydrogenated amorphous silicon (a-Si:H) 4
- Thin-film silicon solar cells design 5

2.3 Silicon Deposition techniques 6
- Plasma-enhanced chemical vapor deposition (PECVD) 6
- Physical vapor deposition (PVD) 7
- Dry Etching (DE) 8

2.4 Characterization methods 8
- Current-Voltage measurements (J-V) 8
- External Quantum Efficiency - EQE 9
- Reflectance and Transmittance (RT) 10
- Raman spectroscopy 10
- Scanning Electron Microscopy (SEM) 11

2.5 Cell Architecture 11
- Glass Substrate 11
- Texturing 11
- Transparent conductive oxide layer (TCO) 12
- Front contact 12
- Silicon layer 12

Chapter 3. nc-Si:H bulk layer - A Preliminary Study *15*

3.1 Introduction: Crystallinity versus Flow parameters 15
- Experimental Details 16
- 3.1.1 Silane flow varied at constant hydrogen flow rate 16
- Results and Discussion 17
- 3.1.2 Hydrogen flow rate varied at constant silane flow rate 19
- Results and Discussion 20
- 3.1.3 Comparison of the two sample batches 22

3.2 Calibrating the PECVD machine for optimal SC 24
- Experimental Details 24
- Silane flow varied at constant hydrogen flow rate 25
- Results and Discussion 25
- Deposition Rates 26

Chapter 4: Performance improvements of Nc:Si-H *27*

4.1 Texturing 27
- Literature Review 27
- Experimental Details 29
- Results and Discussion 30
- Nc-Si:H Samples 30
- Key takeaways 34
- Nc-Si:H subcells in Micromorph Tandem solar cells 35
- Key takeaways 38

4.2 Back Reflector 39

Literature Review 39
Experimental Details 39
Results and Discussion 41
ITO textured samples with i-ZnO and without i-ZnO layer 41
AZO textured samples with i-ZnO and without i-ZnO layer 43
ITO textured with i-ZnO layer deposited at 25°C vs 300°C 45
Key takeaways 47

4.3 TCO Layer **47**
Literature Review 47
Experimental Details 48
Results and Discussion 49
Nc-Si:H 49
AZO textured samples with ITO vs Bilayer TCO 49
ITO textured samples with ITO vs Bilayer TCO 52
Micromorph 54
AZO textured samples with ITO vs Bilayer TCO. 54
ITO textured samples with ITO vs Bilayer TCO 56
ITO textured samples with Bilayer (100+500nm) vs (100+1000nm) 58
Key takeaways 61

Chapter 5: Conclusion 62

References 64

Appendix 67

Chapter 1: Introduction

With the rapidly growing global population, the demand for energy is at an all-time rise. It is urgent necessity to meet this demand while limiting the rate of carbon emissions. Over the next 20 years, the energy demand on a worldwide scale is expected to increase by 48%, based on a report by the U.S Energy Information Administration [1]. An estimate by the Energy Institute accounted that fossil fuels are currently supplying 82% of the global energy demand [2]. With the heavy reliance on fossil fuels, carbon emissions have also increased, reaching 36.6Gt in the year 2021 [3]. With that, the global warming issue is alarming with 2022 being the sixth warmest year since global records started in 1880, with a temperature of 0.86°C above the average 20th-century temperature of 13.9°C [4]. To limit carbon emissions and the accompanying harm of global warming, the Paris Agreement was established in 2015 as an international treaty on climate change with 196 parties to set emissions-reduction pledges. The goal of the Paris Agreement is to set the average temperature on a global scale to well below 2°C, with a maximum of 1.5°C by the end of the century. To reach the goals of the Paris Agreement, the reliance on fossil fuels as a primary source to meet the global energy demand needs to be shifted towards renewables [5]. Renewable energy sources only accounted 12.3% of global energy demand in 2022, to ensure a safer future, the energy supply from renewables needs to be improved significantly[6]. One of the primary sources of renewable energy that has a high potential is Solar energy. The power from solar irradiation on the earth's surface for one hour is sufficient to supply the yearly global energy demand [7]. Thus, utilizing the maximum possible solar energy is essential to supply the energy demand.

First-generation crystalline silicon (c-Si) photovoltaics technology has been known to provide high conversion efficiencies, with records reaching up to 26.1% by NREL [8]. However, using c-Si photovoltaics comes with a few main drawbacks, including the energy-intensive nature of the production process that requires high temperatures and the higher amount of Si consumption and waste during production due to the considerable wafer thickness (100-300 µm) [9]. Moreover, c-Si PV wafers are generally heavy, rigid, and fragile. A promising alternative to c-Si PVs is the second-generation technology of thin-film. Among the common thin-film PV technology are a-Si, CdTe, and CIGS, with a-Si:H being the safest and cheapest due to the abundance and nature of Si. Thin-film silicon solar cell allow for roll-to-roll (R2R) manufacturing that is cost effective and scalable while consuming significantly lower Si in their production due to their lower thickness (3-10 µm) [8]. Furthermore, thin-film silicon solar cells need lower processing temperatures to generate lightweight and flexible cells, reducing transportation and installation costs while allowing them to be used on a broader range of applications. However, one of the main limitations of thin-film silicon solar cells (a-Si:H) is the lower conversion efficiency ranging between 7-14% as compared to c-Si PVs, with conversion efficiencies reaching 19-23% [8][10]. As the technology for c-Si PV is mature, the production costs of c-Si PV modules decreased significantly over the past ten years while their efficiencies have increased, allowing them to dominate 90% of the market share. This has caused a decrease in the demand for second-generation thin film silicon solar cells due to their lower efficiencies and issues with their stability [8]. Thus, in order to make thin film silicon technology commercially viable, the conversion efficiency needs to be improved to produce cells that can generate electricity at a lower cost. Increasing the efficiency of thin-film silicon solar cells will allow for better utilization of the solar spectrum and higher generation of electrical energy leading to lower energy costs. This, along with the advantage of R2R manufacturing of thin-film solar cells, can provide a great incentive to raise the demand for the thin-film technology and make it competitive to c-Si PV.

To reach high efficiency goals with thin-film silicon solar cells, the different layers that make up the solar cells need to be optimized. The focus of this work is to study the different layers involved in thin-film silicon solar cells and strategies to improve them. This thesis addresses the following research questions.

1. Which processing conditions in terms of precursor gas flows is ideal to hydrogenated nanocrystalline silicon depositions?
2. How does texturing of superstrates influence the performance of nc-Si:H and micromorph tandem cells?
3. How will the solar cell benefit optically with an additional intrinsic Zinc Oxide layer at the back side of the silicon stack?
4. Does the double layer bilayer transparent conductive oxides as front contact allows a performance boost of nanocrystalline and micromorph tandem cells?

The work done during this project is reported in the following order:
In Chapter 2, the fundamentals of a solar cell and theoretical background on nc-Si:H are explained. The chapter also goes through the device architecture and the characterization methods used during this project. Chapter 3 addresses the first research question with help of an experiment in which varying hydrogen and silane flow rates are done. This chapter walk through determining the quality of the grown nano crystalline layer. This chapter also goes through the calibrating conditions for stable depositions. Chapter 4 discusses the research questions two, three and four. The chapter goes through the experiments and results that were done for inspecting the influence of sacrificial texturing, the utilization of i-ZnO back reflector, and the influence of using a TCO bilayer on the solar cell's performance. Lastly, chapter 5 concludes the report with the primary outcomes of this project and recommendations for further research.

Chapter 2: Fundamentals

This chapter is introducing the fundamental mechanisms involved in a solar cell operation. It introduces the thin film solar cell technology and the materials used prominently in it. This chapter also covers a short discussion on various deposition techniques and characterization techniques of solar cells.

2.1 The working principle of a solar cell

The main principle on which solar cells operate is based on the photovoltaic effect, which occurs at the junction of two different materials upon exposure to electromagnetic radiation generating a potential difference at their junction [9]. The process occurs in the following main steps illustrated by the simple solar cell model in Figure 1 below.

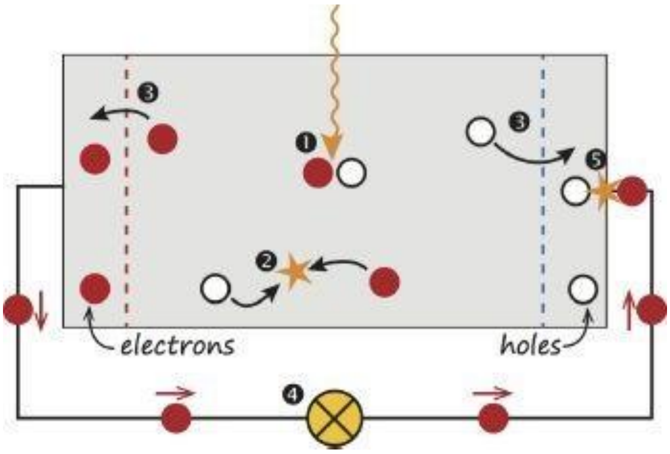

Figure 1 Simple model of a solar cell. With Step.1 showing absorption and generation, Step.2 recombination, Step.3 separation, Step.4 flow of current through external circuit, Step.5 recombination [9]

- Generation

When photons with sufficient energy equal to the band gap of a material are absorbed, they excite an electron from the valence band to the conduction band leading to electron-hole pair generation.

- Separation

If the generated electron and hole pairs are not separated, the energy will be lost due to radiative and non-radiative recombination. To utilize the energy stored in electron-hole pairs, the electrons and holes are separated using a semi-permeable membrane allowing the one-way flow of electrons at one end and the one-way flow of holes at the other end.

- Collection

The separated electron and holes can be used to perform work in an external circuit using electrical contacts. The electrons flow through an external circuit where they perform work before they recombine with the holes in the back contact.

2.2 Thin-film silicon solar cells

Hydrogenated amorphous silicon (a-Si:H)

Hydrogenated amorphous silicon (a-Si:H) is a commonly used material in thin-film silicon solar cells. It is characterized by its disordered lattice that lacks a long-range periodic crystalline silicon network. The silicon and hydrogen atoms in the lattice are arranged in a random order resulting in a large number of dangling bonds (silicon atoms with unbonded covalent bonds) and defects in the lattice of pure amorphous silicon. Pure amorphous silicon is passivated with hydrogen to reduce its defect density from approx. 10^{19} cm^{-3} to around 10^{16} cm^{-3} and thus reduce the associated recombination. An important feature of a-Si:H is its direct band gap, resulting in a much higher absorption coefficient than c-Si [9].

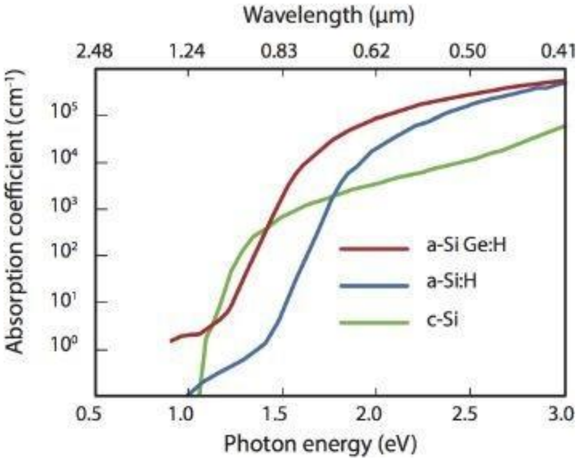

Figure 2 Absorption coefficient of different thin-film silicon matrials [9]

As can be seen in Figure 2, a-Si:H can absorb 100 times more than c-Si at certain wavelength ranges [11]. This allows a-Si: H to be used on much thinner thicknesses (e.g. 0.5 μm) as compared to c-Si (100-300 μm) while having high photon absorption. However, one of the main limitations of a-Si:H is that it suffers from light-induced degradation, also known as Staebler–Wronski effect (SWE). SWE is correlated with metastable defects and structural changes that occur due to the recombination of light-excited charge carriers. Over longer periods, as the defect density in the bulk of the a-Si:H absorber layer increases, the performance of a-Si: H decreases, reaching to 85-90% of its initial efficiency [9]. Depending on the amount of hydrogen incorporated in the silicon network, a-Si: H has a tunable bandgap of 1.6-1.8eV which is higher c-Si (1.12 eV). The higher bandgap of a-Si: H implies that photon absorption is limited to a wavelength range of 800nm, as photons with larger wavelengths do not have enough energy to excite photons in a-Si: H. The higher bandgap of a-Si: H limits it from utilizing the full potential of the AM 1.5 spectrum. In order to extend the spectral utilization and absorption efficiency of a-Si:H, it can be combined with a lower band gap material such as hydrogenated nanocrystalline silicon (nc-Si:H).

Hydrogenated nanocrystalline silicon (nc-Si:H)

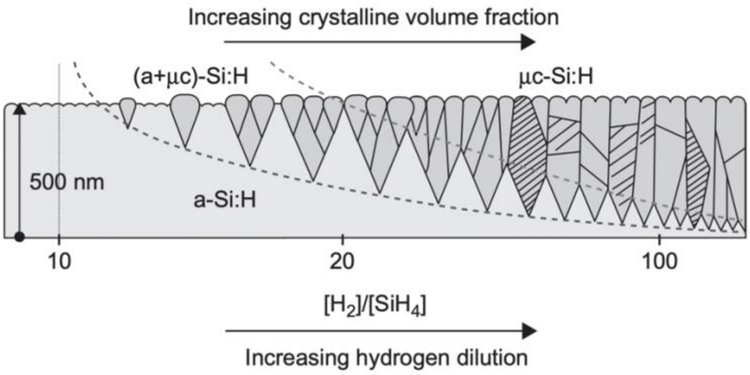

Figure 3 The change in the crystallinity of nc-Si:H with increasing hydrogen dilution during the deposition [12].

Hydrogenated nanocrystalline silicon (nc-Si:H) material consists of small crystalline lattice grains embedded in a-Si:H matrix. Depending on the deposition conditions, the crystalline volume fraction in nc-Si:H can altered; thus, the material's bandgap can be adjusted between 1.1-1.6eV [13]. The crystalline grain growth within the material starts at the nucleation center and grows with a cone-like shape as illustrated in Figure 3. Depending on the deposition conditions, the space between the crystalline grains is filled with a-Si:H phase or voids. As the conical crystalline grains grow, eventually, they collide and form grain boundaries with disordered networks. Grain boundaries can act as defects in nc-Si:H material where recombination occurs. By optimizing the deposition parameters, it is possible to obtain crystalline grains with a larger diameter and fewer grain boundaries. The silane concentration can play a significant role on the degree of crystallinity in nc-Si:H. By increasing the hydrogen dilution while growing the nc-Si:H layer, it is possible to obtain higher crystallinity [13]. A detailed explanation on the influence of silane concentration on the crystallinity of nc-Si:H can be found in Chapter 3. In general, research has found that the best nc-Si:H bulk material is found with a crystallinity near the transition region near amorphous-nanocrystalline with a crystalline volume fraction of 60%.

Nc-Si:H offers less degradation at longer illumination when compared to hydrogenated amorphous silicon (a-Si:H) [14]. As nc-Si:H has a low bandgap of 1.1 eV, it can be used to generate energy from photons at larger wavelengths up to 1100 nm. However, due to the indirect bandgap of nc-Si:H materials, it has a lower absorption coefficient than a-Si:H and thus it needs to be deposited at a higher thickness to reduce the transmittance losses through it [9]. As nc-Si:H offer an extended spectral absorption, this makes them ideal to be used in a tandem cell with the top cell being the a-Si:H layer and the nc-Si: H layer as the bottom cell

Thin-film silicon solar cells design

As there is a large defect density and low carrier mobility in thin-film silicon solar cells, charge carrier transport cannot rely on diffusion due to the limited diffusion length. An intrinsic layer is used for a-Si:H and nc-Si:H in thin film silicon solar cells that are sandwiched between p and n-doped layers. The intrinsic layer between the p-doped and n-doped layers creates a built-in electric field, allowing for the drift of the excited charge carriers across it [9]. The p-layer and n-layers are usually made from a silicon oxide material with a higher bandgap than Si alloys as it has high transparency and lower energy losses due to parasitic absorption. Boron is usually used as a dopant for the p-layer, while Phosphorous is used as a dopant for the n-layer. During this project, a recipe developed by the PVMD group was used in which triple P-layer and N-layers were deposited. The triple P-layer and N-layers consist of a contact layer, a window layer, and a buffer layer. The contact layer provides low ohmic resistance and better contact between the TCO and the bulk layer. The window layer allows for better built-in voltage and high transparency. Lastly, the buffer layer ensures lesser recombination in the P-I interface.

To have a high spectral utilization, a combination of a-Si:H P-I-N layer and an nc-Si:H P-I-N layer needs to be used. In a micromorph tandem cell, a P-I-N layer of a-Si:H is placed at the top after the TCO layer, while the P-I-N layer of the nc-Si:H is placed at the bottom. In this way, the high bandgap of a-Si:H will absorb highly energetic photons with wavelengths up to 800nm while photons with longer wavelength ranges (800nm-1100nm) are transmitted deeper in the cell and are absorbed by the nc-Si:H. Due to the indirect nature of nc-Si:H, its intrinsic layer requires a larger thickness for effective photon absorption. A typical thickness of 1-3 μm is used for the intrinsic nc-Si:H layer while a smaller thickness of 0.3 μm is used for a-Si:H layer. Generally, an intermediate reflector layer (IRL) is placed between the a-Si:H and nc-Si:H layers. An IRL is characterised by having a low refractive index such as i-ZnO which creates a large difference in the refractive index with the top a-Si:H layer which causes light passing through the cell to be reflected into the top cell.

2.3 Silicon Deposition techniques

Plasma-enhanced chemical vapor deposition (PECVD)

Plasma-enhanced chemical vapor deposition (PECVD) is a key deposition technique for silicon in the solar industry. The working principle of PECVD involves applying high voltages to a gas (mainly hydrogen or helium) to create plasma through which ionization of precursor gases occurs. For the deposition process to occur, first the precursor gases (hydrogen and silane) are introduced into the chamber where they get ionized by the plasma into radicals, ions, and free electrons. The ionized precursor gases can then react and form silicon coating on the substrate in the chamber. By controlling the concentration and flow rate of silane and hydrogen in the chamber, the crystallinity of the silicon and optical properties can be altered. One of the main advantages of PECVD is that it offers silicon deposition at low temperatures maintaining dopant profiles [15]

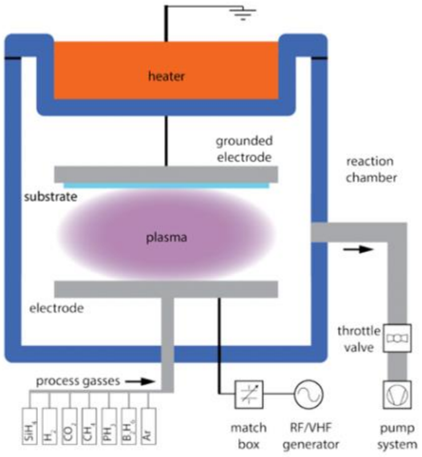

Figure 4 Schematic diagram of a PECVD machine [16]

Figure 4 illustrates the different parts involved in a typical PECVD device. The gas handling systems control the flow rate of the precursor gases into the chamber. The RF electrodes provide the electric energy for the ionization of the precursor gases in order for the deposition process to take place. Depending on the energy of the electrons from the RF electrodes, the interaction of the electrons with silane can occur in various forms including dissociation, attachment, ionization, etc. The substrate is held by the substrate holder which is usually heated to a temperature of 200 °C [17].

As the plasma contains a mixture of radicals, electrons, positive ions, photon metastables, etc, the deposition from the plasma to the substrate occurs in various forms. The radicals formed from silane (Si, SiH, SiH_2, SiH_3) can diffuse to the substrate while high-energy electrons can further promote the reaction. The plasma is charged, however, space charge regions are formed close to the walls between the plasma and the substrate through which positive ions are accelerated into the substrate's surface leading to ion bombardment [17]. The PECVD machine used during this project has six chambers dedicated to the deposition of i-a-Si:H, i-nc-Si:H, p-doped and n-doped depositions, as well as an AZO sputtering chamber.

Physical vapor deposition (PVD)

Physical vapor deposition with electron beam evaporation can be used for depositing metallic layers in thin-film silicon solar cells, including the front and back contacts. The process involves the use of a tungsten filament to provide a high electron beam to heat the source (evaporation material). The process is carried out under vacuum (10^{-3} to 10^{-6} Pa), and the source is typically mounted at the bottom of the chamber where the evaporated metal particles flow upwards [9]. The PVD machine used during this project is referred to as PROVAC. During the project, Al was used as the front contact, and a specific mask was used on which the sample was mounted on to define the deposition area of the front contact. Similarly, another mask was used to define the back contact of the samples in which three layers (Ag/Cr/Al) were used as the back reflector/contact. A detailed explanation on the back contact is presented later in Chapter 4.

Dry Etching (DE)

Dry etching (DE) is a technique used to improve the performance of thin-film silicon solar cells by removing the Si bulk layer that is not contributing in the generation of the charge carriers. This allows for eliminating defects and impurities in the cell that can reduce the mobility of the charge carrier. Dry etching relies on the use of plasma in a vacuum chamber to excite the process gas molecules and generate a mixture of reactive ions and radicals. The generated reactive mixture of ions and radicals can then react with the surface of the thin-film silicon sample that is not covered by a back contact and etch away the layer. Alternatively, highly active radicals can also physically displace and remove the exposed atoms from the surface of the samples [18]. Depending on the plasma power, pressure, and gas flow rates, the extent of etching on the sample can be controlled.

2.4 Characterization methods

The samples made were characterized by various techniques to determine their optical and electrical properties. This section will briefly discuss the methods that were used for the characterization of the fabricated samples.

Current-Voltage measurements (J-V)

One of the main ways of determining the electrical properties of the solar module is by doing the J-V measurement. Usually, the measurement is carried out under standard test conditions (STC) at an AM1.5 spectrum, an irradiance of 1000 W/m^2, and a cell temperature of 25 °C.

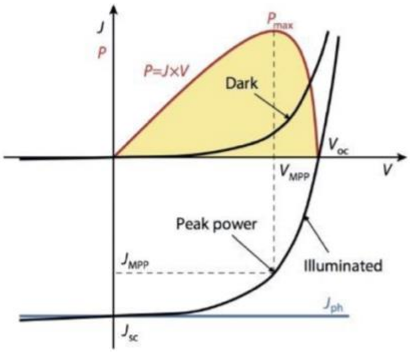

Figure 5 J-V plot under standard conditions (at bottom), Under dark measurement (top) [9]

Some of the main parameters that can be obtained from a J-V measurement include the open circuit voltage (Voc), the short circuit current density (Jsc), the Fill factor (FF), and the efficiency (η) as can be seen in Figure 5. The Voc is obtained at zero current while Jsc is obtained at zero voltage. Moreover, the FF and η can be obtained via the following equations:

$$FF = \frac{J_{mpp}V_{mpp}}{J_{sc}V_{oc}} \quad (3.2.1)$$

$$\eta = \frac{V_{oc}J_{sc}FF}{P_{in}} \quad (3.2.2)$$

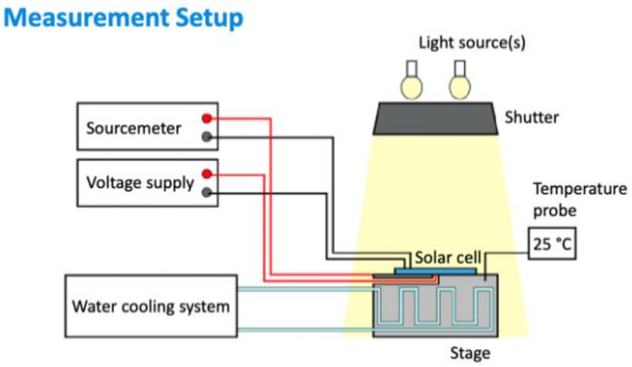

Figure 6 J-V measurement Setup [19]

The J-V setup that was used for measuring the PV modules for this thesis was the AAA WACOM solar simulator that offered the measurements under STC. The setup consisted of Xenon and halogen lamps that simulated the AM1.5 spectrum. The solar module sample is mounted on a stage, and the stage temperature is controlled at 25 °C using a water cooling system as illustrated in Figure 6. The source meter measures the JV properties of the solar module when it is illuminated. Before the measurement is carried out, the system is calibrated using a reference cell.

External Quantum Efficiency - EQE

The external quantum efficiency measurement is done on a solar cell, to measure the ratio of successfully collected electron-hole pairs to the fraction of incident photons. The EQE can be calculated using the following equation [9]

$$EQE\ (\lambda) = \frac{I_{ph}(\lambda)}{e\phi_{ph}(\lambda)} \qquad (3.2.3)$$

The EQE setup that was used for measuring the samples produced during the thesis consisted of an Xenon lamp providing a continuous even spectrum. The light from the xenon lamp is first filtered to prevent the interference of short-wavelength lights with longer wavelengths. As can be seen in Figure 7 the light then passes through a chopper wheel in order to achieve an approximate frequency of 123 Hz. The beam of light then goes through a monochromator which filters and selects the appropriate intensity of light with the desired wavelength for the measurement. The light is focused on the best-performing cell in the module and the measurement is carried out. The lock-in amplifier is used to filter the response of the solar cell's response to monochromatic light from the noise. Before the measurement is carried out, calibration is done using a reference diode. Generally, the short-circuit current density (J_{sc}) values obtained from the EQE measurements are more accurate than the ones obtained from J-V, as J_{sc} obtained from the EQE are not dependent on the incident photon flux.

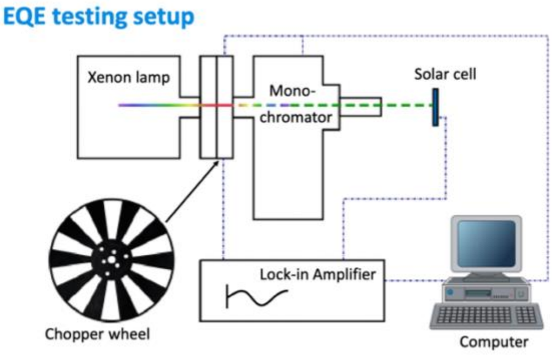

Figure 7 A typical EQE measurement setup [20]

When measuring the EQE of a top or bottom cell in a tandem PV module, biased illumination has to be used in order to make the desired cell current limiting. Let's take for example the measurement of a top cell in a tandem PV module, biased illuminated (red) light should be used to saturate the bottom cell in order to make the top cell current limiting and measure the EQE of the top cell accurately.

Reflectance and Transmittance (RT)

To measure the optical characterizations of the PV module samples, it is important to measure the reflectance and transmittance of the cell. The RT results can give us an indication of how well the texturing on the solar module is and estimate the absorption rate in the cell. Moreover, the reflectance results along with the EQE can be used to measure the internal quantum efficiency of the cell. The device that was used to carry out RT measurement is the Perkin Elmer spectrometer. This spectrometer consisted of tungsten-halogen lamp and a deuterium lamp along with many filters, mirrors, and lenses to focus the beam of light on the solar cell in the sample and carry out the measurement at the desired light intensity. Generally, a testing range of 175-3300nm can be done using the spectrometer.

Raman spectroscopy

Raman spectroscopy is a widely used chemical analysis technique that uses the principle of inelastic scattering of photons to determine the sample's crystallinity, molecular interactions, and chemical structure. When the high-intensity laser from the Raman emitter hits the sample, some of the light is scattered at a different wavelength than the laser source (the Raman scatter) based on the chemical bonds of the sample. The obtained Raman spectrum features different Gaussian photon bands corresponding to the specific bond vibrations. An important characterization from the Raman analysis that was used in this project is the crystalline volume fraction (X).

Generally, the Gaussian photon bands for amorphous and crystalline materials exhibit distinct Raman vibrational modes. By measuring the area of the Gaussian photon bands and obtaining a ratio of the vibrational modes for the crystalline and amorphous fractions in a sample, the crystalline volume fraction can be determined [20]. More information on the type of vibrational mode and crystalline volume fraction calculation method is presented in section 4.2.

Scanning Electron Microscopy (SEM)

Scanning electron microscopy is a technique that relies mainly on a beam of moving electrons to scan the samples and produces images with sample features in the order of nanometers. The emitted electrons from the machine emitter (mainly the tungsten filament lamp) pass through different lenses and apertures to focus the beam on the surface of the sample. When the electron beam touches the surface of the sample, the electrons get scattered and secondary electrons are emitted from the sample making. The interaction of these electrons generates signals through the detector of the SEM machine and the sample's morphology and topology can be determined [21].

2.5 Cell Architecture

The solar cells made for all experiments in this thesis are P-I-N superstrate configuration of area 16mm^2 or 25mm^2. The definition of cell area is done by back contact deposition. Figure 8 shows a representation of the samples. Step by step procedure in the fabrication of samples are as given below.

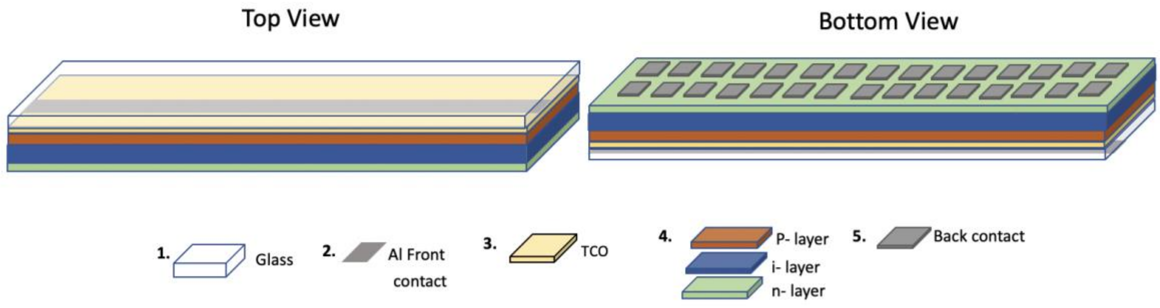

Figure 8 Schematic representation of the device architecture

Glass Substrate

To prepare the substrate for deposition, corning glass with thickness 0.7mm is used. The Corning glass is cut into 2.5cm x 10cm stripes. These stripes are cleaned using ultrasonic cleaning bath where the sample was first dipped in acetone for five minutes followed by another five minutes in isopropanol.

Texturing

The type of texturing used on a glass sample can influence the rate of reflectance at the surface of the cell and affect the light trapping. As the textures in a glass sample scatter the light entering the solar cell, the path length of the light in the active region is increased and a larger rate of the carriers are generated and collected. This in general increases the current generated by the solar cell and improves its overall performance [9].

The texturing on the glass was done using by depositing a sacrificial layer on the glass sample which was then etched using a chemical solution to create textures on the glass while the sacrificial layer was removed over time. Depending on the material used for the sacrificial texturing, textures with different crater sizes were created on the glass sample. For nc:Si-H samples, the effect of texturing using Indium Tin Oxide (ITO) sacrificial layer, Aluminum doped Zinc Oxide (AZO) sacrificial layer, and Intrinsic Zinc Oxide (i-ZnO) sacrificial layer were examined. For micromorph samples, the effect of ITO sacrificial layer, AZO sacrificial layer, and Modulated Surface Textures (MST) combining ITO and AZO texturing and ITO and i-ZnO texturing were examined. For more details about the properties of the textures created by different sacrificial layers refer to the literature review in section 4.1.

Transparent conductive oxide layer (TCO)

TCO needs to be highly transparent and conductive to work efficiently in a solar cell, which is why it is important to optimize its thickness and deposition conditions. A suitable candidate for the TCO layer is indium tin oxide (ITO) thanks to its photoelectrical properties. ITO can provide good electron mobility, tunable carrier density, and high transparency in the visual and infrared region [22]. In this project, ITO was deposited through sputtering using the PECVD machine. The effect of having a bilayer as TCO was also investigated in this project in order to have better opto-electrical properties. The hydrogenated indium oxide layer (IOH) is known to have high transparency in the near-infrared region with low parasitic absorption losses and high electron mobility leading to higher conductivity [23]. By using a bilayer of i-ZnO on top of IOH, we ensure that we combine the benefit of i-ZnO with low parasitic absorption in the near-infrared region with the good lateral conductivity of the IOH

Front contact

The front contact of the solar cell was deposited after depositing the TCO layer. The Al front contact layer was deposited through vapor deposition using the PVD machine. The samples are first kept in a mask that holds the samples and defines the region where the front contact strip is deposited. The masks are then loaded into the PVD machine where an electrical beam evaporates the silver and deposit it into on to the mask.

Silicon layer

During this project, a P-I-N superstrate configuration was used where the p-layer was deposited first as illustrated in Figure 8. The deposition of a P-I-N cell is more challenging compared to N-I-P configuration as the first layer deposited is boron doped and further plasma depositions are done above this layer. The P-I-N layer was deposited using the PECVD machine. The machine consist of 6 deposition chambers (DPC) and each chamber is dedicated for depositing a certain layer depending on the desired properties of the sample.

The samples with TCO and front contact layers are first loaded in the LLC chamber. Using a robotic arm the samples in a single holder are picked from the LLC and placed in DPC1. DPC1 is responsible for P-doping as it's precursor gas is B_2H_6. Depending on the desired sample properties, the sample is then picked from DPC1 and placed into DPC3 to deposit intrinsic amorphous silicon or DPC4 to deposit intrinsic nanocrystalline silicon layer. For n-doping, the sample is placed in DPC2 with the PH_3 precursor gas. Once the P-I-N layer deposition is complete, the samples are unloaded from the PECVD machine. The deposition parameters used can be found in Table 1.

Back reflector and Back contact

During this project, the back reflector used was made up of a combined triple layer of Silver (Ag), Chromium (Cr), and Aluminum (Al). The metal back reflector also served as a back contact for the solar cell. By using a triple-layer back reflector, a combined benefit of optical and electrical properties can be achieved. In order to optimize the back reflector further, an additional i-ZnO layer can be used between the silicon layer and the back contact.

To deposit the back contacts, the samples are first fitted in a mask to define the area for the deposition of the back contact and hold the samples. The samples are then loaded into the PVD machine to deposit the back contacts. Before the deposition process begins, the chamber is loaded with Ag, Cr, and Al as the back contacts of the samples consist of these three materials. The deposition of the i-ZnO layer was done by sputtering using the PECVD machine. A detailed explanation of the different properties of the metal back reflector and the i-ZnO back reflector can be found in the literature review in section 4.2.

Dry Etching (DE)

For a better definition of cell areas Dry etching is used for some samples for this thesis. This help in avoiding overestimation of current and improvement in short circuit resistance of the solar cells. Depending on the plasma power, pressure, and gas flow rates, the extent of etching on the sample can be controlled. During this project, a plasma power of 100W and a pressure of 0.3 mbar, along with H_2 (100sccm) and SF_6 (40sccm) were used for the process of dry etching.

Table 1 Standard deposition parameters for fabricating the Solar Cell

Layer	Power [W]	Pressure [mbar]	Temperature [C]	Gas	Flow rate [sccm]
AZO	300	2.6	300	Ar	20
μc−SiO_x(p)	12	2.2	300	SiH_4	0.8
				H_2	170
				CO_2	2.3
				B_2H_6/ H_2	20
a-Si:H (i)	2.8	0.7	300	SiH_4	40
				H_2	0
μc−SiO_x(n)	11	1.6	300	SiH_4	1
				PH_3/ H_2	1.2
				CO_2	2
				H_2	170
μc−SiO_x(p)	12	2.2	300	SiH_4	0.8
				B_2H_6/ H_2	60
				CO_2	1.6
				H_2	170
μcSi : H (i)	40	4	180	SiH_4	3.5
				H_2	120
μc−SiO_x(n)	11	1.6	300	SiH_4	1
				PH_3	1.2
				CO_2	1.6
				H_2	170
a-Si:H (n)	4	0.6	300	SiH_4	40
				PH_3/ H_2	11
				CO_2	0

Chapter 3. nc-Si:H bulk layer - A Preliminary Study

3.1 Introduction: Crystallinity versus Flow parameters

Obtaining an optimal crystallinity for the nc-Si:H layer is essential for achieving a high charge carrier generation and extraction in a tandem cell of a thin film silicon solar cell. A seed layer approach can be used for the growth of nc-Si:H layer as it has been shown to enhance the uniformity and improve the crystallinity of the nc-Si: H. The process involves the use of a highly crystalline foundation (seed layer) on top of which the bulk layer of nc-Si:H is grown. The seed layer is made up of an i-nc-Si:H layer that is usually grown under high hydrogen dilution. It serves as a nucleation layer on which the bulk layer is grown [24]. The focus of this experiment was to determine the influence of growth parameters on the Si bulk layer since the parameters of the seed layer are already known. To optimize the nc-Si:H layer for the highest efficiency, it should be aimed to reach a crystallinity with a volume fraction ranging from 60-70% [25]. An important parameter affecting the crystallinity of the nc-Si:H layer is the silane concentration (SC). As the silane concentration increases, the crystallinity of the nc-Si:H layer decreases, and the silicon material amorphous lattice increases [26]. This, in turn, affects the material's electrical and optical properties, as having a low SC results in the formation of nc-Si:H crystals with larger grain sizes characterized by lower absorption coefficients. The enhanced crystallinity achieved with lower SC improves the dark conductivity of the sample as lower defects are present at higher crystallinity which promotes the charge conductivity in the sample [26]. The silane concentration is dependent on the flowrates of the silane and hydrogen in the chamber and can be calculated using the following equation:

$$SC = \frac{SiH_4}{SiH_4 + H_2} \qquad (4.1.1)$$

To determine the crystallinity of the sample, Raman spectral analysis can be done in which the photon bands obtained are used to calculate the crystallinity of the sample. Three prominent Gaussian photon bands are relevant for nc-Si:H: The crystalline Si transverse optical band (520 cm^{-1}), the grain boundary band (510 cm^{-1}), and the amorphous Si optical band (480 cm^{-1}) [26]. By analyzing the peaks of the Raman Spectrum, the crystalline volume fraction (*X*) can be determined using the following equation:

$$X = \frac{I_{510} + I_{520}}{I_{480} + I_{510} + I_{520}} \qquad (4.1.2)$$

Based on the literature on nc-Si:H, the best nc-Si:H bulk material can be obtained near the amorphous-nanocrystalline silicon transition region, as at that point, a combination of the highest FF, Jsc, and Voc can be achieved [14]. When examining the effect of the silane concentration (SC) on the efficiency of the nc-Si:H layer, it was determined that increasing the SC was beneficial (increase in Voc, Jsc, and FF) to a certain point after which a sudden decrease in FF and Jsc was observed. This was correlated to the decrease in the crystallinity of the nc-Si:H layer and the growth of amorphous volume fraction in the layer as the SC increased [14].

Experimental Details

During this experiment, the effect of varying the silane and hydrogen flow rates on the quality of the nc-Si:H was observed. Moreover, an estimate on the Silane concentration (SC) range for growing the nanocrystalline silicon bulk layer was determined. In total, ten samples were made, five of which the silane flow rate was varied while the hydrogen flow rate was maintained relatively constant. The other five samples were made by maintaining the silane flow rate and varying the hydrogen flow rate.

It was aimed to achieve a similar range of silane concentrations for both of the sample batches in which the silane and hydrogen flow rates were increased. All samples were grown on glass with AZO sacrificial texturing and a TCO layer made of ITO (150 nm thick). An overview of the samples cell architecture can be seen in Figure 9 below. The conditions for growing the nano-crystalline seed layer in all the samples were constant (SiH_4 flowrate of 1.1 sccm and H_2 flowrate of 120 sccm) and were chosen based on the results obtained during previous experiments in the PVMD group. Once the sample were made, the crystallinity of the samples were determined using Raman spectroscopy. The optical and electrical performance of the samples were also measured using EQE and J-V analysis respectively.

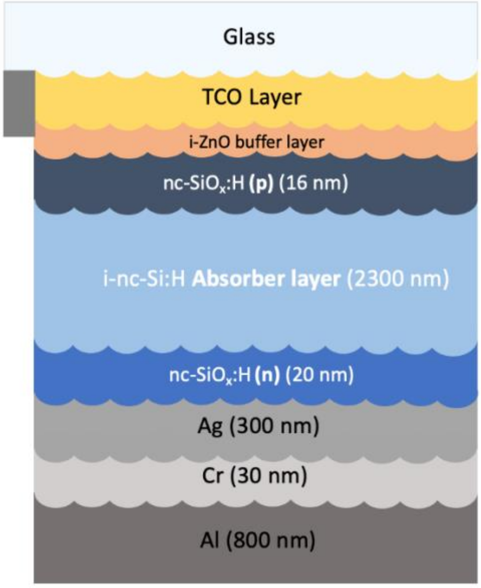

Figure 9 Cross-section of the single junction nc-Si:H cell architecture

3.1.1 Silane flow varied at constant hydrogen flow rate

Table 2 shows the silane flow rate used in each sample while maintaining the hydrogen flow rate relatively constant. The hydrogen flow rate was changed slightly in some samples to achieve consistent silane concentration with the samples in which the hydrogen flowrate was varied.

Table 2: Overview of the silane and hydrogen flowrate in each sample

Silane flow (sccm)	Hydrogen Flow (sccm)	Silane Concentration (SC)
2.3	120	1.9
2.4	117	2
2.6	120	2.12
2.7	120	2.2
2.8	119	2.3

Results and Discussion

To determine the crystallinity of the samples, the area of the optical bands in the Raman spectrum results were analyzed.

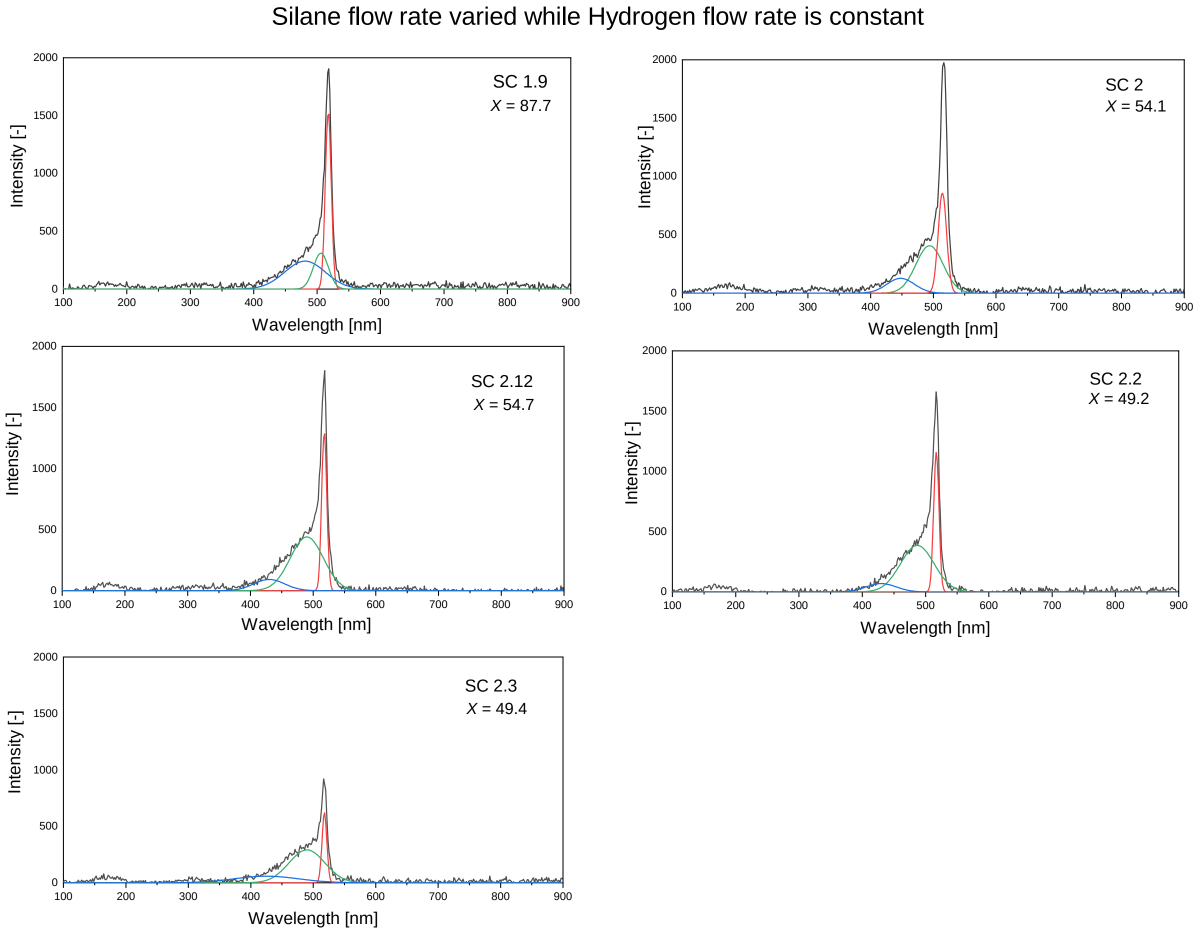

Figure 10 Raman spectrum of the samples in which the silane flowrate was varied.

In Figure 10, the spectrum of each sample has three main optical bands. The red band at 520 cm^{-1} corresponds to the crystalline Si, while the green band at 510 cm^{-1} corresponds to the grain boundary in the sample. Finally, the blue band at 480 cm^{-1} corresponds to the amorphous region in the sample. The area of these bands was used to calculate the samples' crystallinity using the previously introduced equation. As the SC increases, the sample's crystallinity decreases gradually and then shifts at an SC of 2.2, which is related to the transition point towards amorphous. As the experiment is conducted with SC close to the amorphous-nanocrystalline silicon transition region, increasing the silane flow rate beyond a certain point (2.6 sccm) increases the amorphous region in the sample and decreases its crystallinity. But here it shall be noted that the variation in crystallinity is very less than the expected values for a change over a range of 1.9% to 2.2% silane concentration. The crystallinity of the samples achieved was generally low and the change in crystallinity is not consistent which raises a suspicion that the silane flow is not controlled properly.

Inspecting the optical performance of the samples gives an idea of the influence of the nc-Si:H crystallinity on the spectral utilization of the sample. Any interference with the incident photons can also be observed which can be used to optimize the samples further.

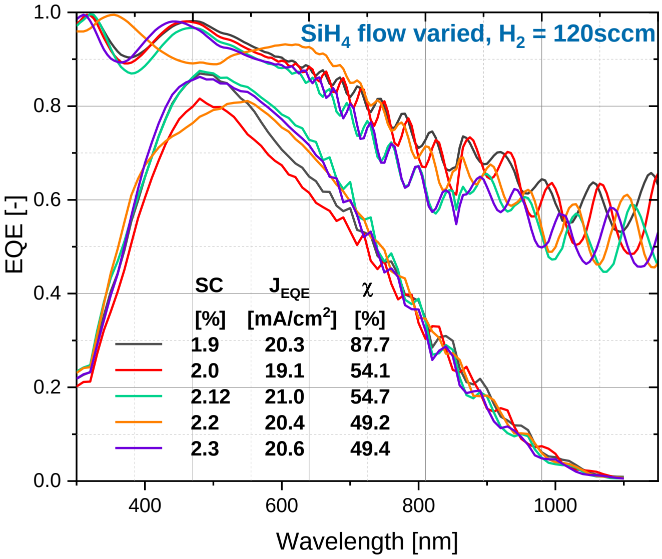

Figure 11 EQE plots of the samples with varying silane flow rate

In Figure11, the sample with the highest spectral utilization was with SC of 2.12%, generating a Jsc of 21 mA/cm^2. The crystallinity of 54.7% achieved with SC 2.12 sample seems to have a decent ratio of crystalline and amorphous regions in the lattice to generate and extract charge carriers effectively. When comparing the Jsc values, it is expected that the Jsc generated increases with the SC to a maximum point and then drops as the crystallinity of the sample decreases. However, this trend cannot be seen in this run, as the samples with SC 2 and SC 2.2 had lower spectral utilization. A possible reason could be an inconsistency with the quality of the deposition by the PECVD machine that these samples have faced. The J-V results should be analyzed to inspect if that was the case. The absorptance plots of the samples had high fringes, mainly in the high-wavelength region (700nm-1000nm). This indicates the presence of interference with the TCO layer of the sample and can be attributed to the type of sacrificial texturing used in the glass sample. The effect of texturing on the performance of the sample will be studied in detail in Chapter 4.

Analyzing the electrical performance of the sample can give an idea of the effect of the crystallinity on the performance of the sample. Moreover, the quality of the deposition of the sample can also be observed by inspecting the series and shunt resistance values.

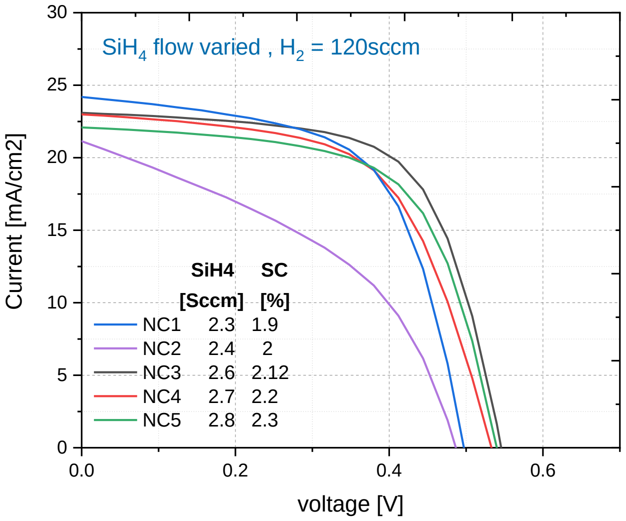

Figure 12 J-V plots of the samples with varying silane flow rate

Table 3 J-V Results of the samples with varying silane flowrate

SC [%]	1.9	2	2.12	2.2	2.3
Voc [V]	0.49	0.44	0.54	0.52	0.54
Jsc EQE[mA/cm^2]	20.3	19.1	21	20.4	20.6
Roc [ohm·cm^2]	11.4	14.5	17.2	16.5	15.2
Rsc [ohm·cm^2]	986	237	2235	874	1792
FF [-]	0.6	0.34	0.63	0.49	0.61
η[%]	5.97	2.86	7.14	5.2	6.79

In Table 3, the sample with SC 2.12 had the highest FF (0.63), Voc (0.54 V), and overall efficiency (7.14%). Moreover, the sample also had the highest shunt and series resistance as compared to the other samples. The shunt resistance values varied significantly in each sample and did not follow a trend. The samples that had a lower optical performance from the EQE analysis (SC 2 and SC 2.2) also had the lowest shunt resistance indicating that there has been an issue with their deposition. The presence of low shunt resistance can be attributed to defects in the silicon layer or the presence of contamination while carrying out the deposition. The highest series resistance was observed in the sample with SC 2.12, which is unexpected as the sample had the highest shunt resistance and overall performance. The presence of the high series resistance can be related to an improper deposition of the back contacts of the sample or the presence of contaminants that hindered the flow of current.

3.1.2 Hydrogen flow rate varied at constant silane flow rate

The following table illustrates how the hydrogen flow rate was varied in each sample while maintaining a constant silane flow rate.

Table 4 Overview of the silane and hydrogen flowrate in each sample

Silane flow [sccm]	Hydrogen Flow [sccm]	Silane Concentration (SC)
2.6	134	1.9
2.6	127	2
2.6	115	2.21
2.6	110	2.3
2.6	105	2.41

Results and Discussion

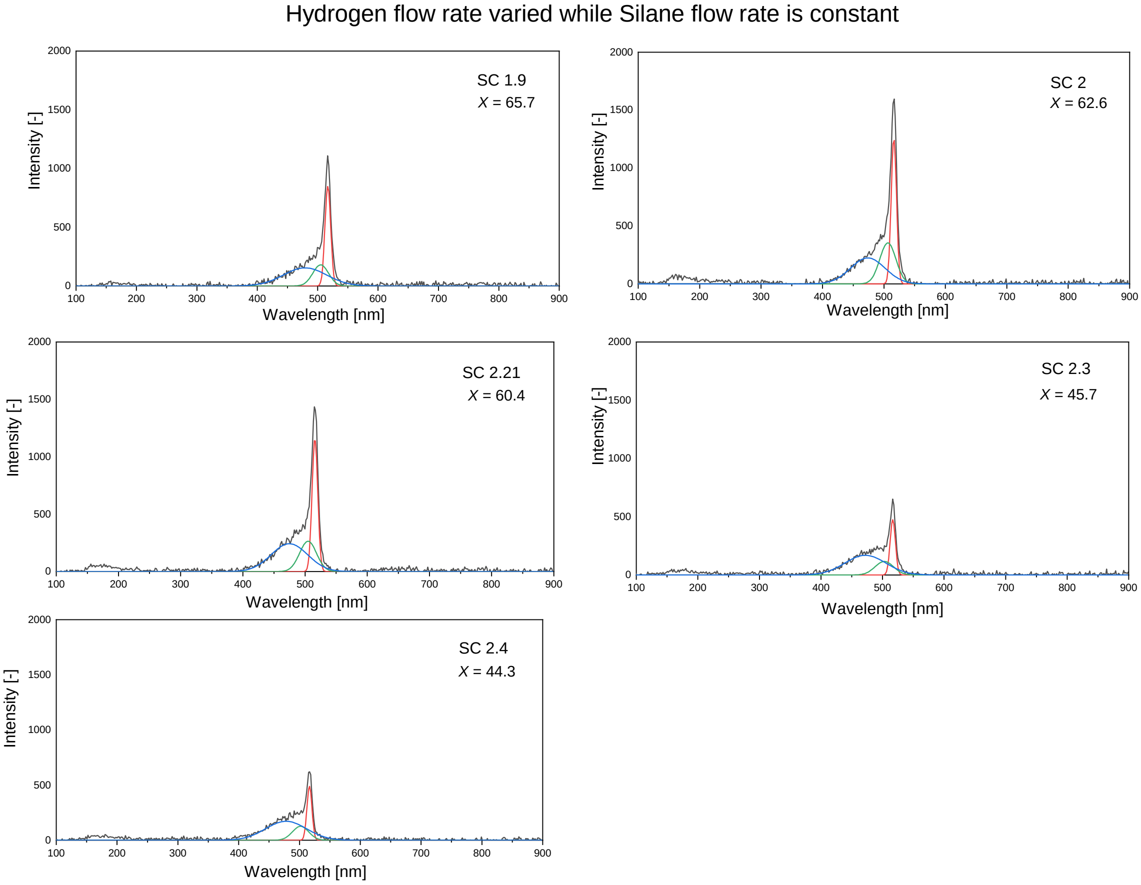

Figure 13 Raman spectrum of the samples in which the hydrogen flowrate was varied.

In Figure 13, A similar trend in the crystallinity of the samples with the increase in SC can be seen. A significant drop in the crystallinity was observed in the sample with SC 2.3, indicating that at a hydrogen flow rate of 110 sccm the transition towards an amorphous occurred in the sample. The SC 2.2 sample had a crystallinity of 61.6% which was much higher compared to a crystallinity of 49.2% in the SC 2.2 sample in which the silane flow rate was varied. The large difference in the crystallinity can be attributed to the nature of hydrogen gas and its effect in diluting the reactive silane precursor gas. It is possible that varying the hydrogen flow rate instead of silane played a role in obtaining higher crystallinity due to the hydrogen gas capability of passivating the dangling bonds and defects in the nc-Si:H, which enhances the crystallinity of the sample.

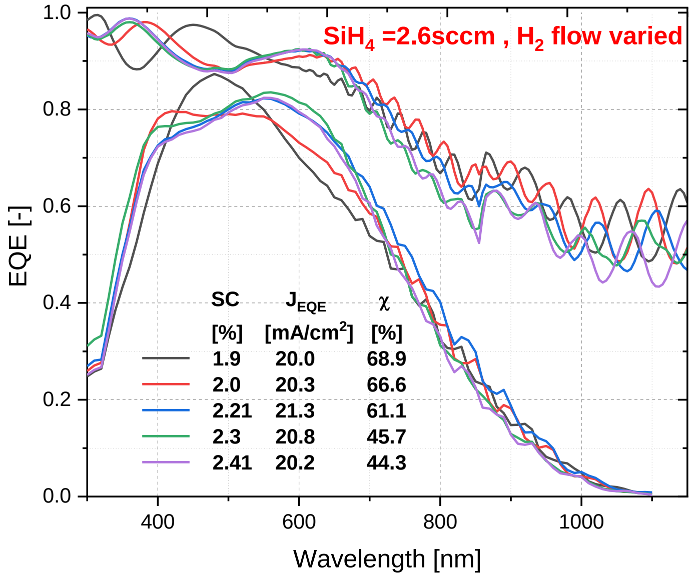

Figure 14 EQE plots of the samples with varying hydrogen flowrate

In Figure 14, the sample with SC 2.21 had the highest spectral utilization generating a Jsc of 21.3 mA/cm^2 with a crystallinity of 61.6%. This result aligns with the literature, which suggests that the best-performing nc-Si:H material is near the amorphous-nanocrystalline transition with a crystalline volume fraction of 60-70%. A significant drop in the crystallinity of the sample with SC 2.3 can be observed, indicating that at an SC higher than 2.21, the transition of the nc-Si:H crystal lattice towards amorphous occurs.

Inspecting the absorptance plots of the samples, a dip in the absorptance values at a wavelength range of 480nm can be observed in all the samples except for SC 1.9%. The decrease in the absorptance values lowered the EQE of the samples at that range. The lower absorptance at a wavelength range of 480 nm can be correlated to an interference with the TCO layer of the samples. The TCO layer in the samples that showed lower absorbance might not have been deposited ideally by the PECVD machine and thus had a different thickness. Altering the thickness of the TCO layer can significantly affect the solar cell's performance as it can reduce the amount of light transmitted into the active layer of the solar cell and thus lower its performance. A similar trend with fringes in the absorptance plots at larger wavelengths that was seen in the sample with varying silane flow rates can also be seen here. All the samples had AZO sacrificial texturing, which was inefficient in texturing the ITO layer as the TCO layer interacted poorly with photons at larger wavelengths. As will be seen later in Chapter 4, nano-sized textures are created with AZO sacrificial texturing, which can be inefficient in scattering photons at larger wavelengths.

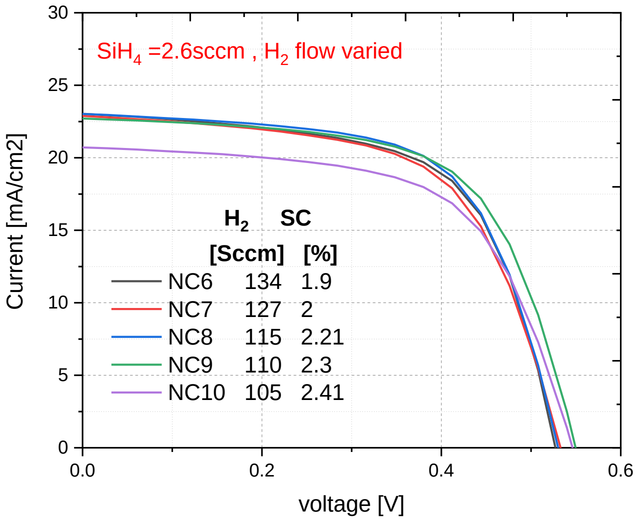

Figure 15 J-V Plots of the samples with varying hydrogen flow rate

Table 5 J-V Results of the samples with varying hydrogen flow rate

SC [%]	1.9	2	2.21	2.3	2.41
Voc [V]	0.52	0.53	0.53	0.55	0.54
JscEQE[mA/cm²]	20	20.3	21.3	20.8	20.2
Roc [ohm·cm²]	13.1	14.5	15.9	13.9	14.5
Rsc [ohm·cm²]	1476	237	1893	3497	1781
FF [-]	0.61	0.6	0.62	0.64	0.6
η[%]	6.34	6.46	7	7.32	6.54

In Table 5, the sample with SC 2.3% had the highest FF (0.64), Voc (0.55V), and overall efficiency (7.32%). However, the performance of the sample with SC 2.12% was comparable as it had the highest Jsc and the difference in FF between the two samples can be explained by the higher shunt resistance in the sample with SC 2.3%. The shunt resistance difference was significant between the samples and was much higher in the sample with SC 2.3%. The difference in shunt resistances can be correlated with the quality of the deposition of the Si bulk layer and the presence of defects. However, since the shunt resistance was remarkably higher in the sample with SC 2.3%, it can also be an outlier in the measurement. The series resistance values of the samples were comparable and overall are in an acceptable range. Generally, the sample in this batch showed more consistent results with slight variations in their Voc and FF.

3.1.3 Comparison of the two sample batches

By comparing the external parameters of the two experiments - the silane flow rate variation, the hydrogen flow variation, we can determine which approach gives consistent results.

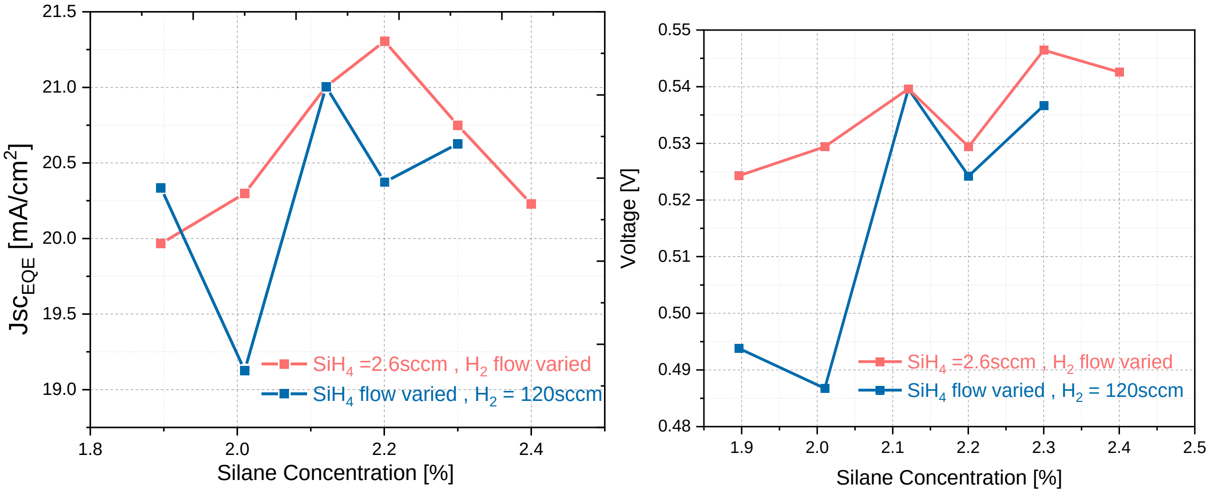

Figure 16 Comparison of the Jsc results (on left) and Voltage results (on right) from the two batches of samples.

In Figure 16, the J-V results of the samples in which the hydrogen flow rate was varied followed a trend in which the Jsc generated increased with SC to a certain point (SC2.2), after which the Jsc dropped with the increase in SC. The observed trend can be correlated to the change in crystallinity with the SC that was previously explained. On the other hand, no clear trend can be observed in the samples in which the silane flow rate was varied. However, these samples also showed low shunt resistances and there is a high possibility that their deposition was inconsistent. This observation extends to FF and efficiency curves too. Moreover, this could be due to an issue with the silane flow panels in the PECVD as previously discussed.

The samples in which the hydrogen flow rate was varied showed an increase in voltage with SC. However, at an SC 2.2 a drop in the voltage can be observed, which could be an outlier since it was the only sample that showed a lower voltage even though it had the highest generated Jsc.

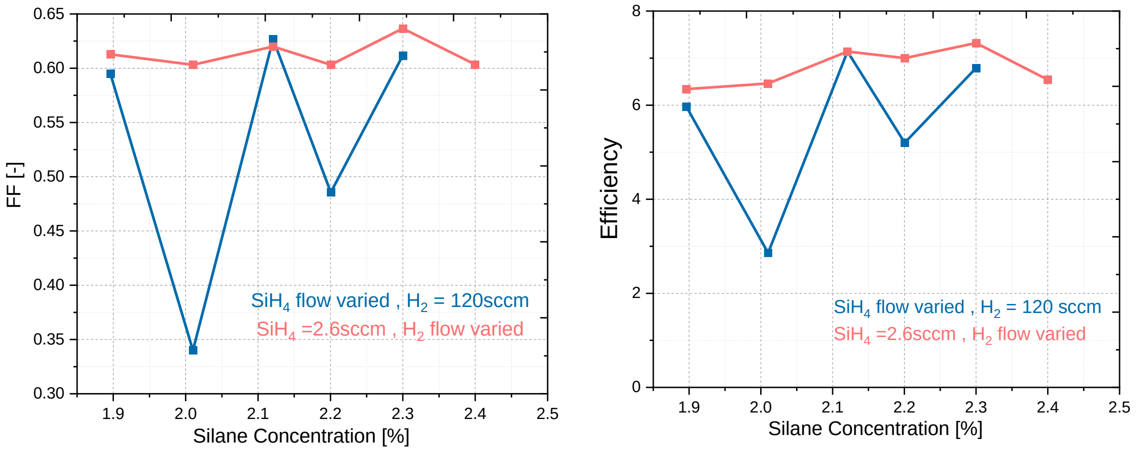

Figure 17 Comparison of the FF results (on left) and efficiency results (on right) from the two batches of samples.

In Figure 17, the samples in which the hydrogen flow rate was varied showed consistent results, and the FF and their efficiency values were comparable. On the other hand, the samples in which the silane flow rate was varied showed very fluctuating results and inconsistent results in the FF and efficiency values which can be attributed to larger defects and lower quality of nc-Si:H. Overall, the performance of the samples in which the hydrogen flow rate was altered was better than the samples in which the silane flow rate was altered. The samples had lower fluctuations and more consistent results, indicating a higher quality of the nc-Si:H bulk layer when varying the hydrogen flow rate. A possible reason for the higher quality of nc-Si:H bulk layer when varying the hydrogen flow rate can be attributed to the hydrogen dilution effect. When the hydrogen gas flow rate is varied, better control over the hydrogen dilution on the silane gas is achieved in which the concentration of the hydrogen gas in the plasma is higher than the silane precursor gas. This promotes the growth of nc-Si:H bulk layer with higher crystallinity and larger grain size as higher hydrogen concentration aids in the nucleation and growth of the nanocrystalline region in the bulk layer [12]. Moreover, hydrogen gas has a passivating effect which can reduce the surface dangling bonds and defects when growing the nc-Si:H layer, and thus a higher quality of the nc-Si:H layer is achieved. The results from the samples in which the hydrogen flow rate was varied suggested that a crystallinity of 60% lead to the highest performance which is inline with the literature [25]. Lastly, as hydrogen is varied over a larger flow rate range (5-10sccm) as compared to silane that is varied over a smaller flow rate range (0.1sccm). It is easier to have better control over the flow rate from the hydrogen flow panel as compared to the silane flow panel that needs to be very precise to fluctuations.

Based on the results obtained, varying the hydrogen flow rate instead of the silane flow rate results in more consistent quality of samples and higher performing samples. Moreover, a higher crystallinity was achieved in samples in which the hydrogen flow rate was varied and more consistent shift in the crystallinity was observed when the SC of the samples was increased. The inconsistent results obtained with the samples in which the silane flow rate was altered can be due the difficulty in controlling the silane flow rate over smaller flow ranges and can also be an indication of the presence of a defect in the flow panels. Upon further inspection, it was indeed concluded that the silane flow panels of the PECVD machine were defective and had to be replaced.

As the silane flow panels were replaced, a new calibration needs to be done to obtain the optimal SC for achieving a sample with a crystallinity of 60%. To determine the exact flow rate of hydrogen and silane, a similar experiment needs to be conducted in which the SC is varied at smaller intervals around the transition point of amorphous to nanocrystalline silicon.

3.2 Calibrating the PECVD machine for optimal SC

As the silane flow panels in the PECVD machine were replaced due to a defect, the calibration of the machine needs to be redone to obtain the optimal flow rate for the SC. Based on the results of the previous experiment, a nc-Si:H crystallinity of approx. 60% resulted in achieving the highest performance. This result was in line with the known literature that suggests the highest nc-Si:H performing material is found near the transition from amorphous to nanocrystalline. To re-calibrate the PECVD machine and obtain the optimal flow rate that results in a nc-Si:H sample with a crystallinity of 60% the following experiment was done.

Experimental Details

A similar approach was used in this experiment to the one previously done however this time only the silane flow rate was varied as the optimal hydrogen flow rate was known to be 120sccm. By conducting this experiment, it is possible to observe if the silane flow panels are functioning properly by inspecting the consistency and the gradual change in the crystallinity of the samples. Five samples were made in total with the same deposition conditions that were used in the previous experiment discussed earlier in this chapter. It is worth noting that complete working cells were not made during this experiment and only nc-Si:H layers on glass samples were made to calibrate the PECVD machine for future experiments. The crystallinity of the samples were determined using Raman spectroscopy.

Silane flow varied at constant hydrogen flow rate

Table 6 Overview of the silane and hydrogen flowrate in each sample

Silane flow [sccm]	Hydrogen Flow [sccm]	Silane Concentration (SC)
2.4	120	2
2.6	120	2.1
2.8	120	2.3
3	120	2.4
3.2	120	2.6

Results and Discussion

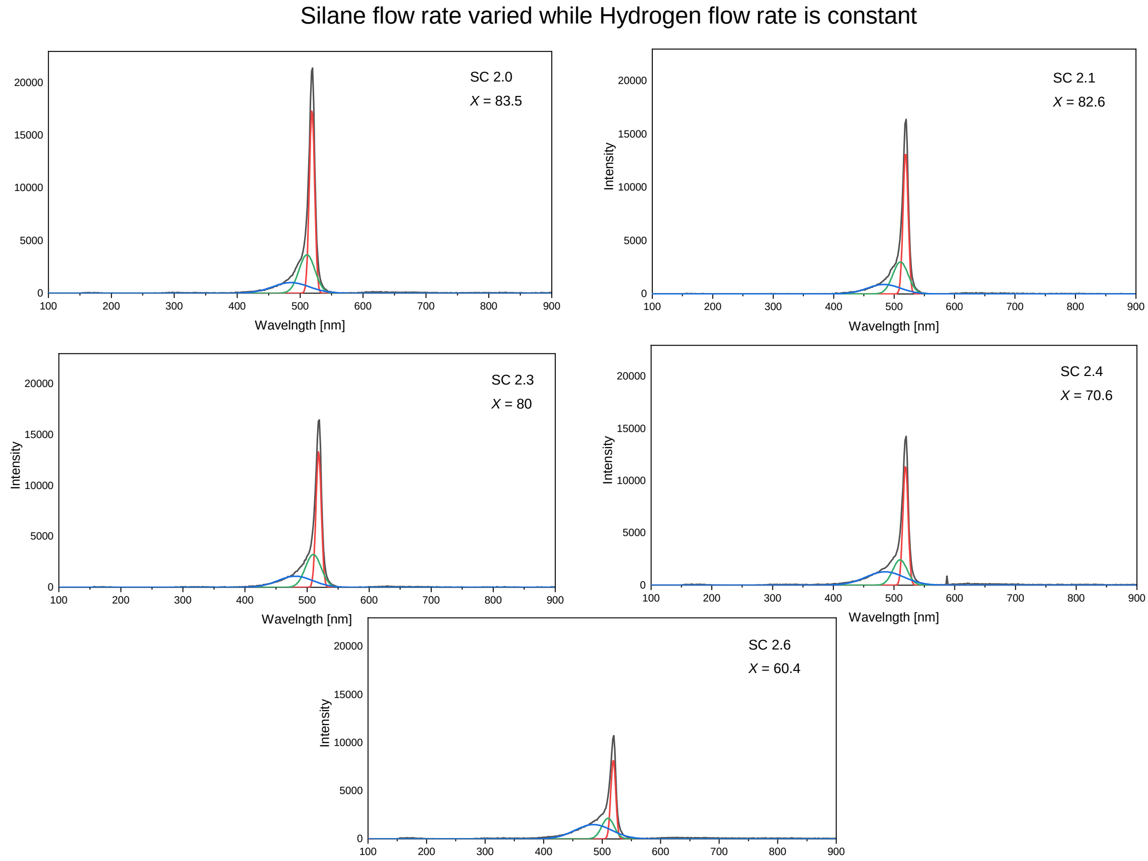

Figure 18 Raman spectrum of the samples in which the silane flow rate was varied.

In Figure 18, the crystallinity of the samples decreased with an increase in the SC. This can clearly be seen by the red band at 520 cm^{-1} corresponds to the crystalline Si that is decreasing with the increase in the SC. A gradual change in the crystalline volume fraction can be observed indicating that the silane flow rate panels were working as intended since there weren't any significant changes between the samples. A crystallinity of 60% was achieved in the sample with the SC of 2.6. This indicates that a silane flow rate of 3.2 sccm and a hydrogen flow rate of 120 sccm can be used in future experiment to achieve nc-Si:H samples with a of crystallinity of 60%.

For further research, it is possible to inspect the effect of plasma power on the deposition time by conducting another experiment in which the plasma power is increased while maintaining a constant SC. It is expected that the deposition rate will increase using a higher plasma power, as it has been seen in a similar experiment [13]. Having a higher deposition rate can speed up and optimise the process of manufacturing the samples.

Deposition Rates

The sample was observed under SEM and the result was 1554nm thickness at 3600 seconds.

This translates to a deposition rate of 0.43nm/s.

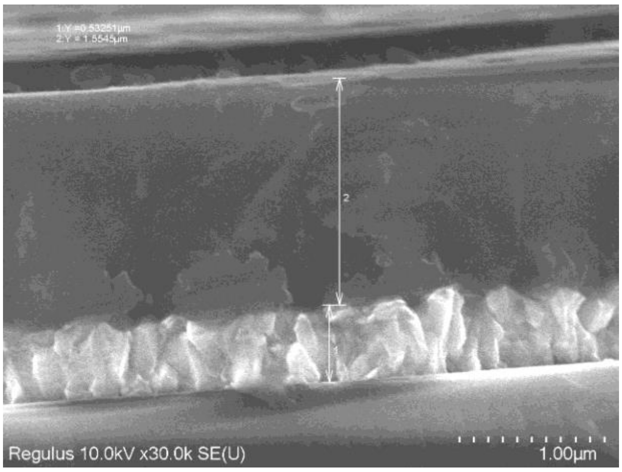

Figure 19 SEM of the nc-Si:H sample deposited on glass + ITO for 36000s.

Chapter 4: Performance improvements of Nc:Si-H

To optimize a micromorph solar cell, different layers in the cell need to be improved and utilized together. In this chapter, different parameters for improving the nc-Si:H will be discussed and the effect of utilizing these parameters in a micromorph layer will be inspected further. The chapter begins with a introduction about texturing and the effect of using different textures on the performance of nc-Si:H and micromorph cells is examined later in the section. Next in section 4.2 the concept of utilizing a back reflector is introduced and the effect of using an additional i-ZnO back reflector on the performance of a nc-Si:H is examined. Lastly, in section 4.3 the properties of a TCO layer are introduced and the effect of using a TCO bilayer on the performance of nc-Si:H and micromorph cells is inspected.

4.1 Texturing

Literature Review

The type of texturing used on a glass sample can have a significant influence on the performance of the solar cell as it affects the scattering of light in the solar cell. The textures used on a glass sample introduce irregularities on the glass which scatter the light entering the solar cell and increase its path length in the active region of the cell. This improves the light trapping and the EQE of the solar cell as more photons interact with the active layer and a larger number of carriers are generated and collected in the cell. As a result, a larger current output is generated and the overall efficiency of the solar cell is improved [9].

To texture the glass samples, sacrificial texturing approach is used as it has been proven to be an effective method. A thin sacrificial layer is deposited through sputtering on the glass. This layer acts as a mask, which when etched with a chemical solution, the glass underneath the layer is etched over time, creating textures on the glass while the sacrificial layer is removed during the process. Depending on the type of material used for the sacrificial layer, different chemical solution are used for etching and textures with different properties are created.

Indium tin oxide (ITO) and aluminum-doped zinc oxide (AZO) are both heterogeneous polycrystalline materials. This means that when etched, their layers do not etch homogeneously as some regions etch faster than others. As a result, random textures are obtained when using ITO and AZO sacrificial texturing. Parameters such as temperature, pressure, and deposition power of the sacrificial layer can influence the quality of the sacrificial layer, which along with the etching time can influence the characteristics of the craters obtained [27]. The analysis of the effect of different parameters on the textures is out of the scope of this thesis project, for a detailed explanation of the parameters and conditions used to create the textures used during this project refer to Criel [28]. To create the textures on an ITO sacrificial layer, wet etching was done using an aqueous solution of HF and H_2O_2 [29] while the wet etching of the AZO sacrificial layer was done using a dilute solution of HNO_3 and HF [8:1] [30].

Parameters such as root mean square roughness value (*Sq*) and the texture aspect ratio (*Str*) are used when describing the characteristics of the textures. The *Sq* value gives insight on the root mean square height of the texture over the entire length of the sample. The *Str* value describes the depth of the texture divided by its width [31]. Using ITO sacrificial texturing, micro-sized crater-shaped textures can be created on a glass sample as compared to nano-sized craters obtained using AZO sacrificial texturing. The craters obtained with ITO sacrificial texturing have in general a higher *Sq* and *Str* than craters obtained with AZO sacrificial texturing. This indicates that craters formed using ITO sacrificial texturing have on average larger features and deeper craters as compared to craters formed with AZO sacrificial texturing. Having larger crater-size textures created by ITO sacrificial texturing can be beneficial in effectively scattering photons at larger wavelengths. That is because the textures roughness size is comparable to the wavelength in the IR-region which can improve the EQE of the cell in that region. When comparing samples with ITO and AZO sacrificial texturing, it was found that the diffuse transmittance with ITO processed sample is higher than the AZO processed sample. That is due to the increased optical path length of light at higher wavelengths caused by the micro-textures of the ITO sacrificial texturing which increase the diffusivity of light in that region [28]. The use of nano-textures created by using AZO sacrificial texturing are necessary to achieve high light trapping and light in-coupling in a-Si:H as nano textures can help in scattering photons at shorter wavelengths. However, when nano-textures are used in micromorph cells the electrical performance of the cell deteriorate. That is because nc-Si:H cells grown on top of the a-Si:H are sensitive to surface morphology and the sharp nano-textures reduce the electrical performance of nc-Si:H (mainly Voc and FF) [29]. Thus, further optimization to the surface texturing is necessary to scatter the light effectively in micromorph cells without influencing the quality of the nc-Si:H. A possible solution to scatter light at a larger wavelength range in a micromorph cell is to combine ITO and AZO sacrificial texturing to create modulated surface texturing (MST).

Using an MST, a combined benefit of ITO and AZO sacrificial texturing can be obtained. First, the ITO layer is deposited and etched to obtain larger micro-sized craters on top of which smaller nano-sized craters are created using AZO sacrificial texturing. By doing so, better light trapping can be achieved and the overall electrical performance of the cell can be improved. That is because using MST light can be scattered better at a wider range of wavelengths allowing for better light trapping in the top and bottom cells of a micromorph cell and a larger number of electrons and hole pairs to be generated [29]. Moreover, the deteriorating electrical performance of the micromorph cell that was faced with AZO sacrificial texturing is mitigated. The effect of using i-ZnO sacrificial texturing was also examined during this project. Due to the lack of literature on i-ZnO material, there is no concrete explanation on the effectiveness and the type of texturing that can be created using i-ZnO. The results from the experiments will be used to give a better understanding of the material.

Experimental Details

To study the effect of texturing on the performance of nc-Si:H cells, samples were made with AZO sacrificial texturing, ITO sacrificial texturing, and i-ZnO sacrificial texturing. The device architecture can be seen in Figure 20. The TCO layer for all the samples was the same and was made from ITO that was deposited through sputtering with a thickness of 150 nm. At the back of the cell, a back reflector of i-ZnO with a thickness of 60 nm was deposited on top of which the back contact (Ag/Cr/Al) was deposited to reduce the transmittance and enhance the absorption in the bottom cell. Before the deposition was done, SEM and AFM scans of the textured glass samples were done to observe and compare the properties of the crater-shaped textures. After depositing the nc-Si:H cell, J-V, and EQE measurements were done to determine the electrical and optical properties of the samples.

To inspect the effect of texturing on micromorph cells, samples with AZO sacrificial texturing, ITO sacrificial texturing, MST containing a combination of ITO and AZO sacrificial texturing, and MST containing ITO and i-ZnO sacrificial texturing were made. All the samples had a TCO Bilayer containing IOH and i-ZnO with a thickness of 100 nm and 500 nm respectively. The samples also contained a back reflector of i-ZnO on top of which the back contact (Ag/Cr/Al) was deposited. Similar to what was done with the nc-Si:H samples, the micromorph samples were measured for J-V and EQE. The samples then went through dry etching to observe any improvements in the performance of the samples.

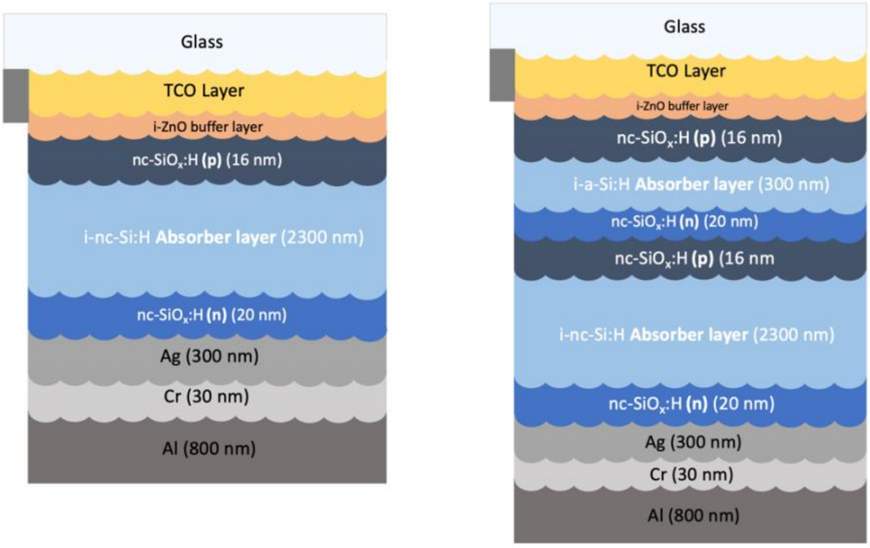

Figure 20 Cross section of solar cell architecture of single junction nc-Si:H sample (on the left) and micromorph sample (on the right)

Results and Discussion

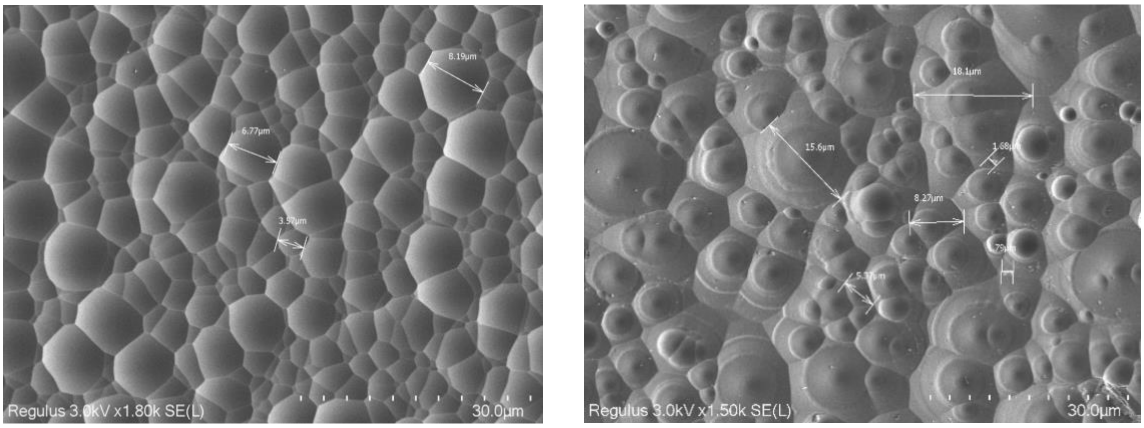

Figure 21 SEM image ITO sacrificial texture on the left and AZO sacrificial texture on the right

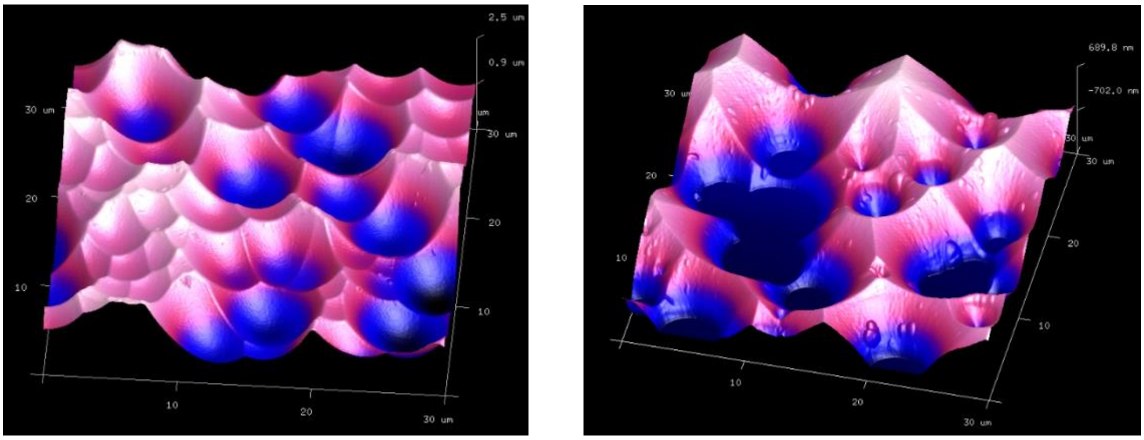

Figure 22 AFM figure of ITO sacrificial texture on the left and AZO sacrificial texture on the right

In Figure 21 the SEM images of the ITO and AZO sacrificial textures can be compared. Although ITO sacrificial textures create micro-sized craters while AZO sacrificial textures create nano-sized craters, the craters of the AZO sacrificial texture seem to look larger than the ITO sacrificial texture. However, when inspecting the AFM images in Figure 22, it can clearly be seen that the craters made with the ITO sacrificial texture have deeper craters with hemispherical character. The craters made with AZO sacrificial texture have craters that are shallower with a non-hemispherical character. The difference in the crater shapes obtained with ITO and AZO sacrificial textures can significantly influence the range and extent to which the incident photons are scattered in the sample. To observe the effect of texturing on the performance of the nc-Si:H and micromorph tandem cells, the optical performance of the samples with different textures should be compared.

Nc-Si:H Samples

AZO vs ITO vs i-ZnO sacrificial texturing for nc-Si:H cells

The texturing used in a glass sample mainly influences the optical properties of the sample. Using the results of the EQE measurements, the total spectral utilization of the cell can be observed, and the influence of the different glass texturing can be determined. The electrical properties of the samples are obtained from the J-V measurements and can give more information on how well the samples were deposited.

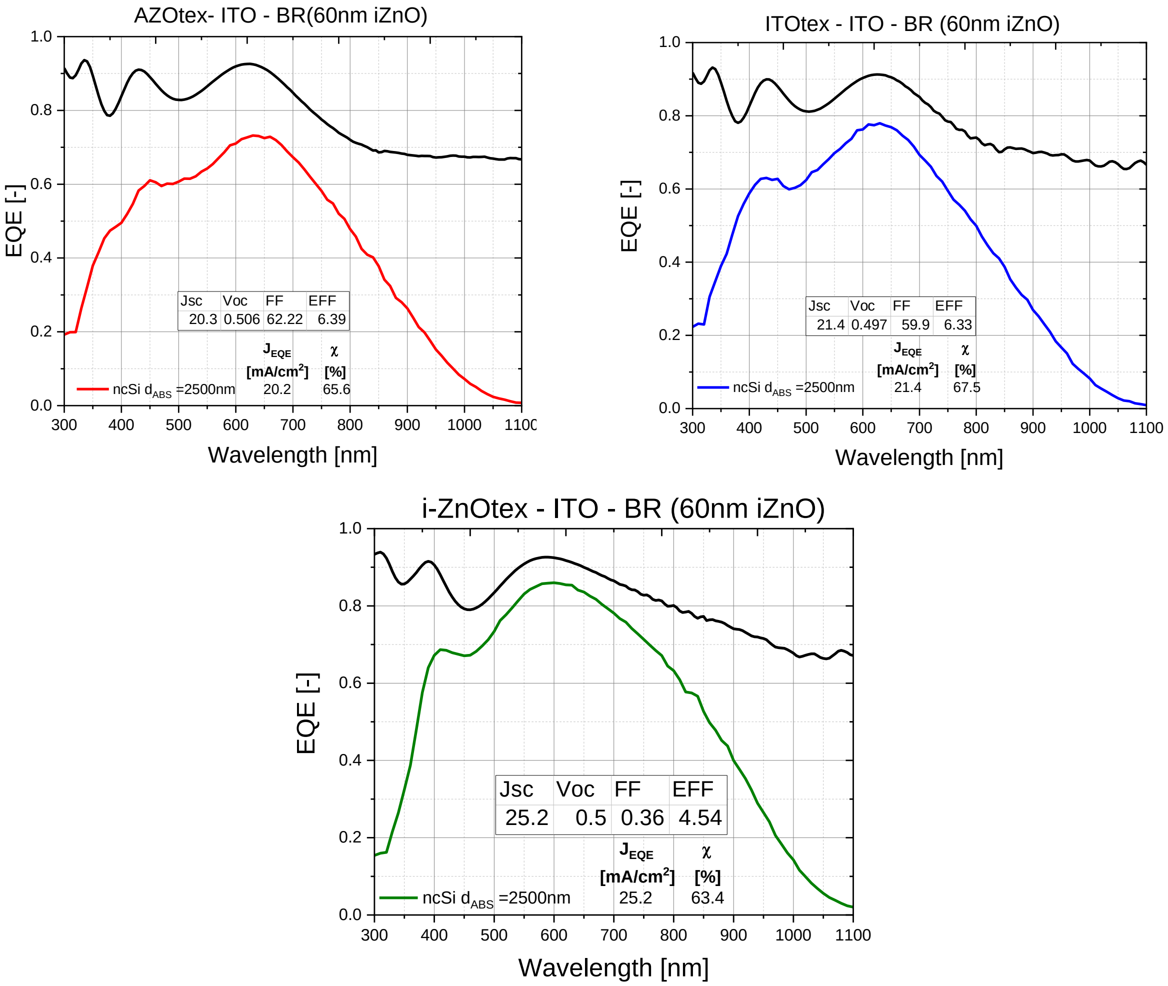

Figure 23 EQE results of the samples with AZO, ITO, and i-ZnO sacrificial texturing, with BR referring the use of additional i-ZnO back reflector.

In Figure 23, the sample with i-ZnO sacrificial texturing generated the highest Jsc of 25.2 mA/cm^2 as compared to a Jsc of 20.3 mA/cm^2 and 21.4 mA/cm^2 in the samples containing AZO and ITO sacrificial texturing. The sample with the i-ZnO sacrificial texturing seemed to have in general higher absorptance when compared to the other samples. At a wavelength range of 400nm to 600nm, the gap between the absorbance and EQE in the samples containing AZO and ITO sacrificial texturing is larger compared to i-ZnO sacrificial textured sample, indicating larger parasitic absorption. This can be attributed to the thickness of the TCO layer. Upon further inspection, the TCO layer in the samples containing AZO and ITO sacrificial texturing had a thickness of 150nm while sample containing i-ZnO sacrificial texturing had a TCO layer with a thickness of 120nm which was evident in the transmission curve fringes. The larger TCO thickness can cause larger parasitic absorption in the samples as compared to the thinner TCO thickness. The thickness difference was due to unstable deposition conditions in the sputtering chamber.

A dip in the absorptance values at wavelength ranges of approx. 370nm and 500nm can be seen in both the AZO and ITO sacrificial textured samples while compared to the sample with i-ZnO sacrificial texturing the magnitude of the fringes were smaller and slightly shifted towards lower wavelengths. The presence of the fringes is an indication of the interference of the photons with the TCO layer. To reduce the influence of interference in the TCO layer, the texturing in the TCO layer needs to be optimized further. The better performance seen with absorptance values of the sample with the i-ZnO sacrificial texturing is again related to the thinner TCO layer in that sample. At longer wavelength (900 nm), the sample with the i-ZnO sacrificial texturing had a better blue response with an EQE of 0.40 while the other two samples showed a low blue response with similar EQE values of 0.25. The presence of a higher blue response with the sample containing i-ZnO sacrificial texturing can indicate that craters made with the i-ZnO sacrificial layer are more effective in scattering photons at longer wavelengths and thus higher absorbance can be achieved. However, to examine if the better blue response was mainly due to the texturing generated with the i-ZnO sacrificial layer or if it was again related to the thin ITO layer in that sample, a comparison with another sample that was deposited along with the i-ZnO sacrificial texturing sample that had a different sacrificial texturing should be done.

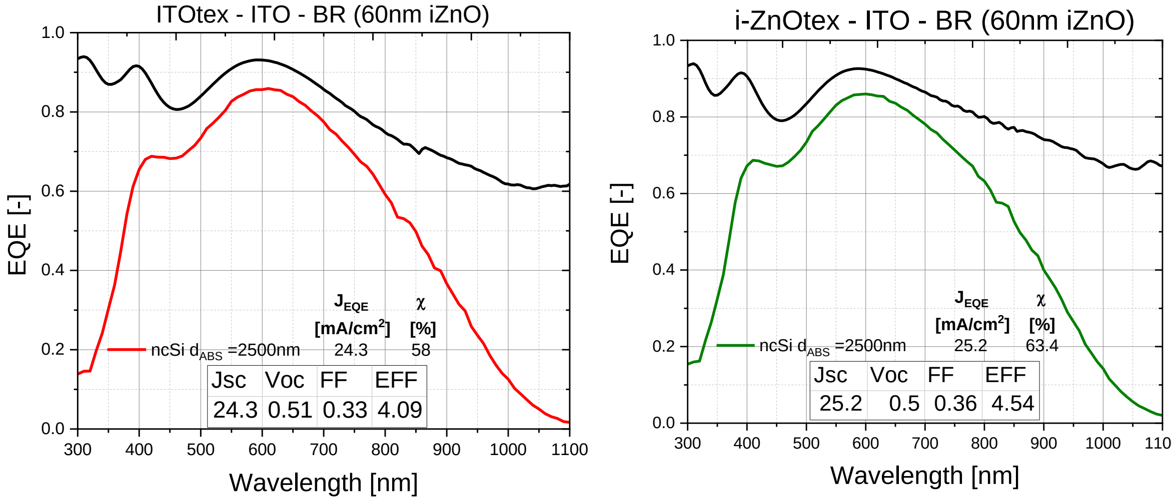

Figure 24 EQE results of samples with ITO and i-ZnO sacrificial texturing that were deposited during the same run.

For the sake of comparison, another sample was deposited with ITO sacrificial texturing during the run that the sample with i-ZnO sacrificial texturing was deposited and its optical performance can be compared in Figure 24. The samples seem to have comparable optical performances and the blue responses at a wavelength of 900 nm were quite similar, with the blue response in i-ZnO sacrificial textured sample being slightly higher. Comparing the blue response of the ITO sacrificial textured sample in this run to the sample with the ITO sacrificial texturing that was previously analyzed (TCO thickness 150nm), at a wavelength range of 900nm, the sample with the ITO sacrificial texturing in this run had a higher EQE (0.40) while the sample with the thicker TCO had a lower EQE (0.25). Since both the samples had the same ITO sacrificial texturing and the main difference between the two samples was the thickness of the TCO layer, it can be concluded that the better blue response of the i-ZnO sacrificial textured sample that was previously analyzed was due to the thinner TCO of the sample. The sample with i-ZnO sacrificial texturing, however, had a better spectral utilization as it generated a Jsc of 25.2 mA/cm^2 as compared to the sample with the ITO sacrificial texturing that had a Jsc of 24.3 mA/cm^2. For a full comparison between the electrical properties of the two samples please refer to the appendix section. Overall, it can be concluded that the use of i-ZnO sacrificial texturing resulted in a higher performance in nc-Si:H samples as compared to ITO sacrificial texturing.

To reduce the parasitic absorption in the TCO layer, the thickness of the TCO layer needs to be optimized and the texturing in the TCO layer needs to be improved further. Moreover, using an anti-reflection coating on the TCO sample can also be beneficial as it reduces the reflection in the TCO/Si interface and increases the amount of light transmitted into the cell. A study on the effect of using an anti-reflection coating (ARC) on a TCO layer claimed that using an ARC on a TCO layer can reduce the reflection at the TCO/Si interface to nearly zero. During the study, an ARC made up of TiO_2 was deposited on a ZnO TCO layer which helped in reducing the reflectance at a wavelength range of 550nm from 10.2% to 6.4% and thereby improving the Jsc of the nc-Si:H by 3.8% [32]. The use on an ARC on the TCO layer can be utilized in future experiments. Depending on the TCO layer used, an ARC material should be chosen with the appropriate refractive index between that of the TCO and Si layer to minimize the reflection at the TCO/Si interface through refractive index grading.

Although the use of different textures mainly influences the optical performance of the samples. It is beneficial to go through the J-V results of the samples to determine if there have been any issues with their deposition by inspecting the series and shunt resistance values.

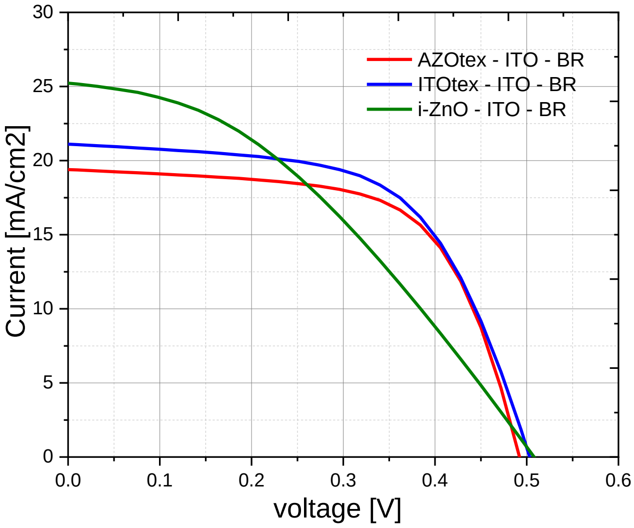

Figure 25 J-V plots of the samples with AZO, ITO, and i-ZnO sacrificial texturing

Table 7 J-V Results of the AZO and ITO nc-Si:H samples

	AZO	ITO	i-ZnO
Voc [V]	0.51	0.49	0.5
Jsc EQE [mA/cm^2]	20.2	21.4	25.2
Roc [$ohm \cdot cm^2$]	12	10.1	45.3
Rsc [$ohm \cdot cm^2$]	1398	1052	372
FF [-]	0.61	0.6	0.36
η[%]	6.32	6.3	4.54

In Figure 25, the samples with AZO and ITO sacrificial texturing had a lower series resistance (Roc) while the sample with i-ZnO sacrificial texturing had a much higher Roc. Moreover, the shunt resistance (Rsc) values of the AZO and ITO samples were much higher than the i-ZnO textured sample. It is worth noting that the AZO and ITO samples were made during the same run while the i-ZnO sample was done in a separate run. Upon further inspection, all of the nc-Si:H samples that were processed along with the i-ZnO textured sample suffered from high series resistance and low shunt resistances mainly due to an issue with the deposition of the ITO TCO layer. The deposited ITO layer had a lower thickness (120nm) and a higher sheet resistance than expected. The lower thickness of the ITO layer and higher sheet resistance reduces the conductivity in the TCO layer and thereby increases the series resistance. Moreover, the poor shunt resistance in the i-ZnO textured sample is an indication that there have been defects that have been most likely caused by the TCO layer. Defects in a sample lead to localized low resistance regions which provide a non-desirable current pathway and leakage in the sample. The higher series resistance and lower shunt resistance of the i-ZnO sample led to a significantly lower FF which reduced its overall efficiency. Comparing the performance of the two samples with AZO and ITO sacrificial texturing, it can be seen that the Voc, FF, and overall efficiency of the two samples are very comparable, with the AZO sample having a slightly better performance mainly due to the higher shunt resistance.

Key takeaways

Overall, the sample with the ITO sacrificial texturing that was deposited along with the sample with AZO sacrificial texturing showed a higher optical performance. The sample with i-ZnO sacrificial texturing showed an even higher optical performance. To allow for a fair comparison, it is advised to repeat the deposition on the three different sacrificial layer textured samples at the same time to ensure that differences in deposition quality is not faced and a consistent TCO thickness is obtained. Moreover, it is also important to monitor the deposition parameters before carrying out the deposition to ensure that everything goes smoothly. Inspecting the crater size and depth of i-ZnO sacrificial texturing can help in verifying the size of the textures and their comparability to ITO sacrificial texturing. Thus, it is suggested to perform SEM and AFM analysis on the craters of i-ZnO sacrificial textures.

Nc-Si:H subcells in Micromorph Tandem solar cells

Based on the literature review, the optical performance of Modulated surface texturing (MST) which is a combination of micro and nano sized features, is expected to be superior to samples with AZO or ITO sacrificial texturing, as the texturing in MST's is expected to scatter incident photons over large range of the spectrum. The ITO sacrificial texturing is also expected to perform better than the AZO sacrificial texturing since micromorph samples grown on AZO sacrificial texturing have been shown to experience deteriorating performance due to the reduced quality of the nc-Si:H layer grown.

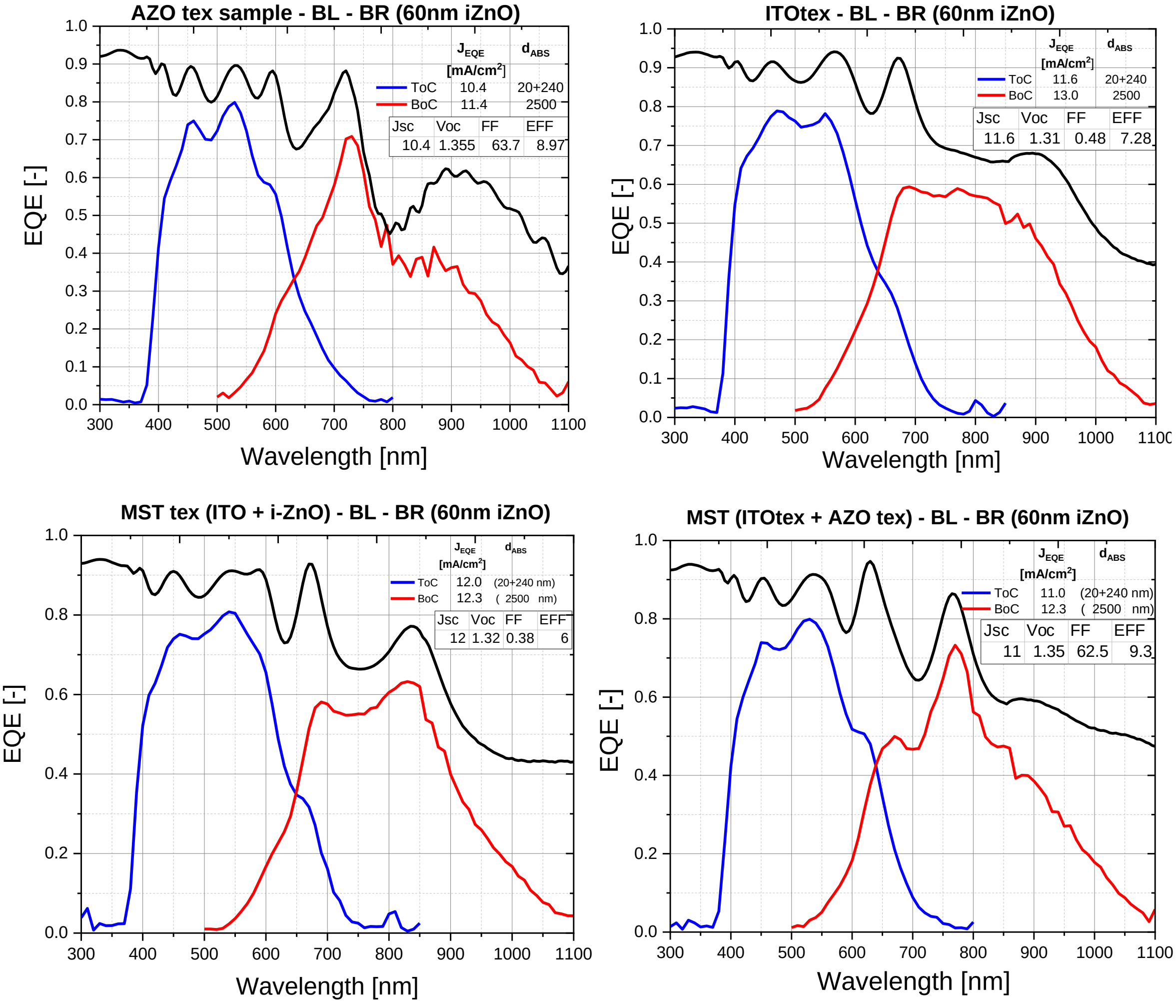

Figure 26 EQE measurement results of the AZO (top left), ITO (top right), MST with ITO +i-ZnO (bottom left), and MST with ITO + AZO (Bottom right), with BL referring to the TCO bilayer and BR to i-ZnO back reflector.

In Figure 26, the micromorph sample with the highest spectral utilization was the one with ITO sacrificial texturing with a total generated Jsc of 24.6 mA/cm^2 and the second highest was the sample with MST (ITO + i-ZnO) with a Jsc of 24.3 mA/cm^2. A lower Jsc of 23.3 mA/cm^2 was generated with the MST (ITO + AZO) micromorph sample and the least Jsc was generated by the AZO-processed sample (21.8 mA/cm^2). The higher spectral utilization of the ITO-processed micromorph sample was impressive, as it indicates that the micro-sized craters generated by the ITO sacrificial texturing were even more effective in scattering the incident light than the MST textured samples.

Looking closer at the EQE of the bottom cell in the ITO textured sample, we can see that in general there are lower fringes in the absorptance plot and higher blue response at a wavelength range of 900nm compared to the other samples. The lower rate of fringes in the absorptance value indicates that the ITO sacrificial texturing was able to scatter incident photons at higher wavelengths more effectively due to the larger size of carters obtained. Moreover, the higher performance with the ITO-processed sample can also be due to the higher quality of the nc-Si:H grown in the micromorph cell as the Jsc generated by the bottom cell of the ITO-processed sample was higher than all the other samples. This can imply that the micro-sized textures produced through ITO sacrificial texturing can be ideal for growing a higher quality nc-Si:H layer with larger grain size and fewer cracks than nc-Si:H layer grown in samples with other types of sacrificial texturing. However, the effect of the sacrificial texturing on the quality of the nc-Si:H needs to be inspected further using SEM.

Comparing the absorptance graphs of the four samples can give an idea of the effectiveness of the craters in scattering the incident light into the sample. By optimizing the textures in the TCO layer, incident photons are scattered more effectively which increases the path length of light in the active layers of the micromorph sample resulting in generating a higher current output. In all of the four samples, fringes in the absorptance plots can be seen which indicates that further optimization in the texturing of the TCO layer is necessary in order to improve the scattering of light in the TCO. The fringes in the absorbance plots of the ITO processed and the MST (ITO + i-ZnO) samples were lower which resulted in generating higher current in the top cells of these two samples. At a wavelength of 470nm, the ITO processed sample had the highest EQE value for its top cell reaching approx. 0.79 while at the wavelength range of 540nm the EQE performance of the top cell in the MST (ITO + i-ZnO) sample was the highest reaching approx. 0.81. The higher EQE performance of these two samples compared to the other samples indicates that the texturing used was more effective in scattering the incident light. Moving forward, a large fringe can be seen in the absorptance plot of all the samples at a wavelength range of 600nm to 700nm which can be related to the optical cavity formed at the top cell. Lastly, apart from the ITO-processed sample, large fringes in the absorptance values at wavelength ranges of 800nm to 1000nm can be seen in the samples. This affects the performance of the bottom layer in the micromorph cell. Both the above scenarios indicate insufficient scattering of photons at larger wavelengths. At a wavelength range of 750nm-780nm a peak can be seen in the EQE plots of the bottom cells in the AZO textured sample and the MST (ITO+AZO) sample which cannot be seen in the other two samples. The absorbance can also be seen to be higher in these two samples which was not expected. A possible explanation to higher absorbance can be related to the constructive interference of the reflected light by the metal back reflector in these two samples. It can be that due to the use of AZO sacrificial texturing, the light is scattered in a way that causes interference when reflected by the back contact.

Overall, losses due to parasitic absorption in the TCO bilayer of all four samples can be observed. That is mainly the infrared – far infrared region between the absorptance and EQE plots in the graphs of the samples. To reduce the effect of parasitic absorption in the TCO layer, the thickness of the TCO layer needs to be optimized along with optimizing the texturing in the TCO layer to obtain better optical performance and higher current generation. The optical performance of the AZO-processed sample was the lowest compared to the other samples. The amplitude of the fringes in the absorptance plot was higher and the current generated by the top and bottom layers of the sample were the lower when compared to all the other samples. This indicates that the nano-sized craters generated by using AZO sacrificial texturing were inefficient in scattering the incident photons and a lower overall performance was achieved. This also caused in the presence fringes at the longer wavelength range (red region) of the spectrum as the nano-sized textures cannot scatter photons at larger wavelengths effectively unlike micro-sized textures.

Inspecting the external parameters of the samples can give an idea of how well the samples performed in general. The samples were measured for J-V after dry etching to observe if there have been any improvements in the series and shunt resistances of the samples.

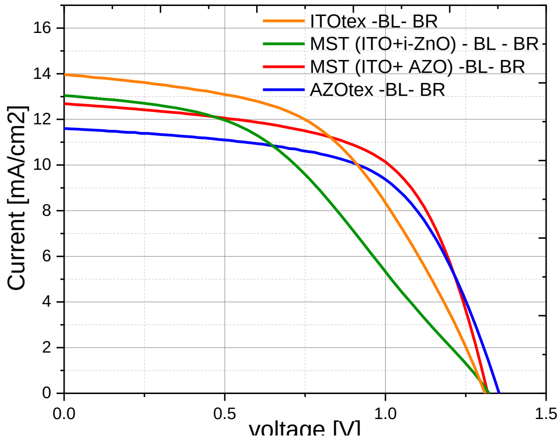

Figure 27 J-V plots of the micromorph samples before DE

Table 8 J-V results of the micromorph samples with different textures

	ITO	MST (ITO+ i-ZnO)	MST (ITO+AZO)	AZO
Voc [V]	1.31	1.32	1.34	1.35
Jsc EQE [mA/cm²]	11.6	12	11	10.4
Roc [ohm·cm²]	69.4	109	66.92	80.66
Rsc [ohm·cm²]	2857	2482	4303	5146
FF [-]	0.48	0.378	0.583	0.591
η[%]	7.28	5.99	8.59	8.3

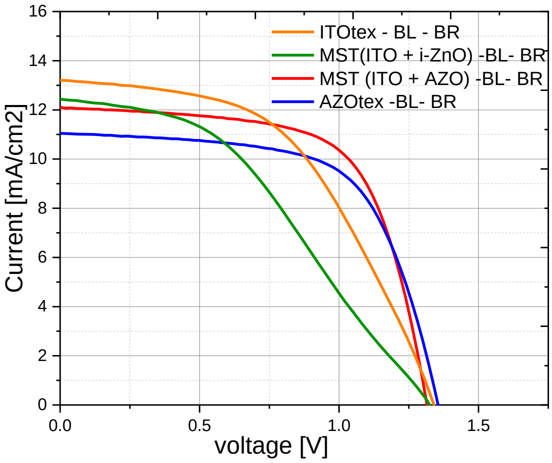

Figure 28 J-V plots of the micromorph samples after DE

Table 9 J-V results of the micromorph samples with different textures after DE

	ITO	MST (ITO + i-ZnO)	MST (ITO +AZO)	AZO
Voc [V]	1.34	1.33	1.34	1.35
Roc [ohm·cm²]	96.9	102	53.3	56.3
Rsc [ohm·cm²]	3758	4052	9057	8680
FF [-]	0.452	0.404	0.619	0.637

From the results displayed in Figure 27 and Table 8, the samples with the AZO sacrificial texturing and MST(ITO+AZO) showed a higher FF and overall efficiency than the samples with ITO sacrificial texturing and MST(ITO+i-ZnO). This was not expected as the EQE results have shown that the ITO sacrificial textured and MST(ITO+i-ZnO) samples had higher optical performances and a higher Jsc values. Looking closer at the shunt resistance values, it can be seen the AZO sacrificial textured and MST(ITO+AZO) samples had a higher Rsc values while the other two samples had a much lower Rsc values. It is important to note that the AZO sacrificial textured, and MST(ITO+AZO) samples were deposited together during the same run while the ITO sacrificial textured and MST(ITO+i-ZnO) samples were deposited together in another run. This indicates that the higher Rsc and electrical performance of the AZO sacrificial textured and MST(ITO+AZO) samples were mainly due to the better deposition quality during that run. The lower shunt resistance values of the ITO sacrificial textured and MST(ITO+i-ZnO) samples can be due to the poor TCO layer deposition during that run. Upon further inspection, the ITO TCO layer that was deposited during that run was thinner with a thickness of 120nm as compared to 150nm. The lower thickness of the TCO layer can limit the current flow and increase the sheet resistance. Similarly, the deposited TCO layer might have also had defects in its structure that act as a leakage path reducing the shunt resistance. Lastly, a lower shunt resistance can also be due to contaminants such as dust in the deposition chamber that lower the quality of the deposition on the samples and reduce their Rsc value.

In Table 9 the Rsc values of all the samples have improved significantly. As dry etching removes the Si bulk layer that does not contribute to generating current, it removes all the defects and impurities in the Si layer that can create a leakage path and reduce the shunt resistance. This also results in improving the series resistance of the samples as it decreases the contaminants and defects that can hinder the flow of current in the sample. Although in general, the samples showed a lower series resistance after dry etching, the ITO sacrificial textured sample was an exception as it had a higher series resistance. A possible reason could be that the sample might have been over-etched or a defect might have been introduced while etching which hindered the flow of current and increased the series resistance.

Key takeaways

ITO and MST (ITO+i-ZnO) sacrificial texturing resulted in the highest optical utilization for micromorph samples. The samples produced had less interference with the incident photons which resulted in transmitting a larger portion of the incident light into the active layers of the solar cell. The ITO textured sample resulted in a higher Jsc, while the MST (ITO+i-ZnO) textured sample had a better current matching between its top and bottom cells. The presence of fringes in the absorptance plots indicates that there is interference with the TCO layer due to inefficient texturing. Thus, further optimisation in the texturing of the TCO layer is required to obtain better scattering of light and higher transmittance.

4.2 Back Reflector

Literature Review

Back reflectors are mainly used in thin-film silicon solar cells to reduce transmissive losses. The back reflector for thin-film silicon solar cells used in the PVMD group also acts as a back contact and is made up of three layers consisting of silver (Ag), Chromium (Cr), and Aluminum (Al) with thicknesses of 300nm, 30nm, and 800nm respectively. By using a combination of the three metals, different properties of the metals can provide a combined benefit on the overall function of the back reflector. The high reflectivity of Ag is ideal for reflecting light in the visible and near-infrared region (400-700nm) back into the active layer of the cell [33]. Moreover, the high electrical conductivity of Ag provides excellent charge carrier collection and transport by providing a low resistance pathway at the back contact. However, Ag has a limitation as it can reduce the performance of the solar cell over the long term as it can diffuse into the active layer of the cell. To prevent this issue, a Cr layer is used to increase the stability of the back contact by impeding the diffusion of Ag into the active layer while providing adhesion to the layer underneath [33]. Lastly, an Al layer is used as a back surface field to aid in reducing charge carrier recombination. Combining the three layers results in generating a stable back contact that has good conductivity and reflectivity in thin-film silicon solar cells.

To improve the reflectivity of the back reflector further, an i-ZnO layer can be used as an optical buffer between the semiconductor and the metal back reflector [34]. As the i-ZnO layer has a relatively low refractive index (n=1.8) and a high bandgap of 3.3 eV, it promotes reflection in the infrared region when it is placed between the metal back contact and the silicon layer. This allows in reflecting photons at longer wavelengths (780nm-1100nm) that are not reflected by the metal back reflector into the nc-Si:H of a tandem micromorph cell which overall increase the performance of the cell [35]. Moreover, the i-ZnO layer can also reduce absorption losses in the metal back contact as it reduces the rate of plasmonic excitation in the metal [36]. Added to that, the i-ZnO layer can also inhibit the diffusion of the Ag back contact into the Si which overall improves the performance of the solar cell over the long term. Furthermore, the i-ZnO layer can help in reducing the contact resistance between the silicon layer and the metal back contact thanks to its high electron mobility [37]. By using an i-ZnO layer, the thickness of the active intrinsic nc-Si:H can be made thinner which can benefit the solar cell as it reduces the rate of recombination [34]. It is expected that pre-heating the i-ZnO before deposition can improve the performance of the i-ZnO back reflector. Using a higher pre-heating temperature allows in complete evaporation of organics and the initiation of the crystallization of the i-ZnO layer with larger grain size and higher uniformity which overall improves the quality of the deposited i-ZnO as fewer cracks are formed [35].

Experimental Details

To inspect the effect of having an additional i-ZnO layer back reflector on top of the metal (Ag/Cr/Al) back reflector, nc-Si:H samples were used during this run with the device architecture illustrated in Figure 29. Two of the nc-Si:H samples were made with AZO sacrificial texturing while the other two nc-Si:H samples had ITO sacrificial texturing. In each pair of samples with the same texture, one sample had an additional i-ZnO back reflector with a thickness of 60nm. All samples were made with a TCO bilayer made from IOH/i-ZnO (100nm+500nm) and had a metal (Ag/Cr/Al) back reflector. Additionally, to inspect the effect of heating temperature on the performance of the i-ZnO back reflector, a pair of AZO sacrificial textured nc-Si:H samples were deposited. One of the samples had an i-ZnO layer deposited with a heater temperature of 25°C while the other sample had an i-ZnO layer deposited with a heater temperature of 300°C.

It is important to note that in the first four samples, the deposition of the i-ZnO layer was done using a mask with a cell size of 5x5 mm in the PECVD machine while the depositions of the back contact were carried out using a mask with a cell size of 4x4mm in the PVD machine. The difference in the mask sizes used during the run resulted in high Jsc values from the J-V measurements due to the larger area of the i-ZnO layer. An additional dry etching step was done to remove the excess area of the i-ZnO and to inspect the effect of removing impurities that may be found in the Si bulk layer on the overall performance of the solar cell.

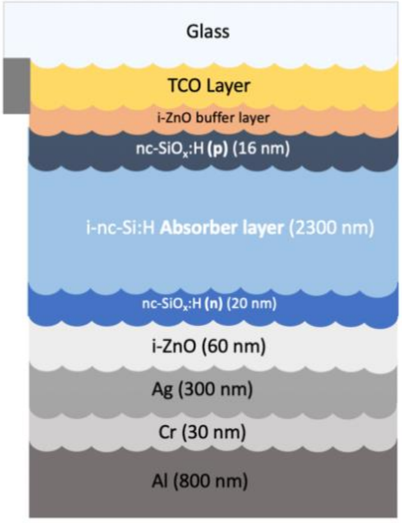

Figure 29 Cross-section of the single junction nc-Si:H cell architecture with an additional i-ZnO back reflector

Results and Discussion

ITO textured samples with i-ZnO and without i-ZnO layer

To determine the effect of having an additional i-ZnO back reflector layer, the optical performance of the two ITO textured samples with and without the i-ZnO layer can be compared.

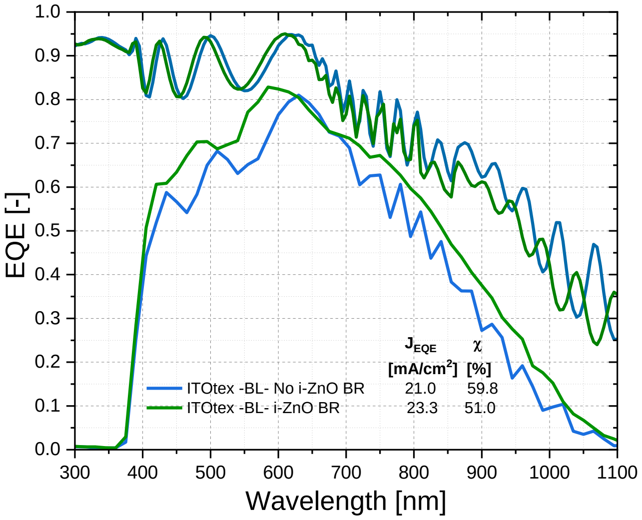

Figure 30 EQE plots of the ITO textured samples with and without an additional i-ZnO layer

From Figure 30, the optical performance of the ITO textured sample with the additional i-ZnO back reflector was higher. The overall spectral utilization of the sample with the additional back reflector resulted in a Jsc of 23.3 mA/cm^2 while a lower Jsc of 21 mA/cm^2 was obtained with the sample without the i-ZnO back reflector. This indicates that the use of i-ZnO improved the Jsc of the sample by approx.11%. Moreover, at higher wavelength ranges (700-1100nm), a higher EQE was achieved with the sample containing the i-ZnO back reflector. This can be correlated to the fact that the i-ZnO layer can reflect photons in the infrared region which are not reflected by the metal (Ag/Cr/Al) back reflector which improves the performance of the nc-Si:H sample in the red region. At a wavelength of 600nm, a maximum EQE value of approx. 0.83 was achieved with the sample containing the i-ZnO back reflector layer. While the maximum EQE achieved with the sample without the i-ZnO back reflector was approx. 0.80 at a wavelength of 640nm. Furthermore, the optical response at shorter wavelengths (400nm-600nm) has improved with the sample containing the i-ZnO layer as fewer fringes and a higher EQE plot were achieved. This can be due to the fact that having an additional i-ZnO back reflector layer on top of the metal back contact can enhance the scattering of the light that is reflected by the metal back contact into the solar cell. Thus, the scattering of the photons at shorter wavelengths is improved and the efficiency of converting shorter wavelength photons is increased due to higher absorption correlated with improved optical path length. The absorbance plots obtained for the two samples were comparable, although the sample i-ZnO showed less interference and higher EQE performance at longer wavelengths. It might be that the reflectance measurement was done on a different cell than the cell in which the EQE measurement was done which resulted in giving a misleading absorption result.

Inspecting the J-V results of the samples can give an idea on how well the deposition of the samples was done and whether utilizing an additional i-ZnO layer can improve the electrical performance of the solar cell.

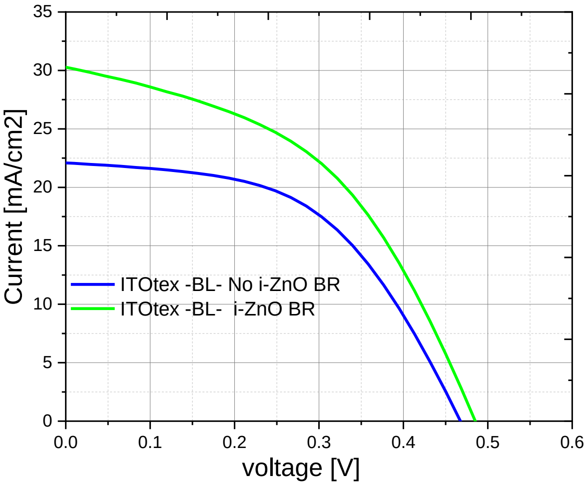

Figure 31 J-V plots of the ITO textured samples with i-ZnO back reflector and without i-ZnO back reflector

Table 10 J-V Results of the ITO textured samples with i-ZnO back reflector and without i-ZnO back reflector

	ITO-No BR	ITO-BR
Voc [V]	0.467	0.484
Jsc EQE [mA/cm²]	20.98	23.3
Roc [ohm·cm²]	32.3	25.9
Rsc [ohm·cm²]	1299	380
FF [-]	0.506	0.46
η[%]	4.96	5.18

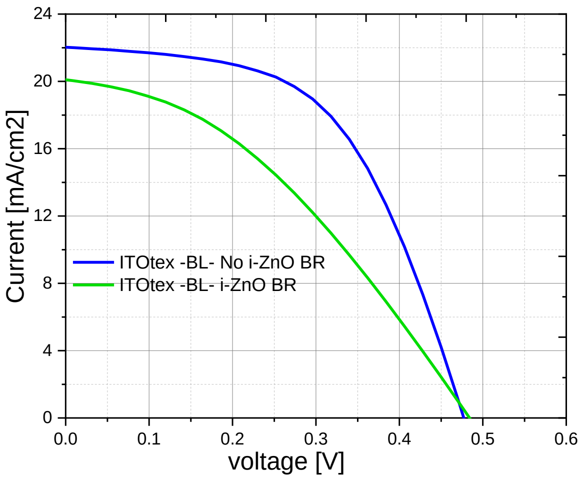

Figure 32 J-V plots of the ITO textured samples with i-ZnO back reflector and without i-ZnO back reflector after DE

Table 11 J-V Results of the ITO textured samples with i-ZnO back reflector and without i-ZnO back reflector after DE

	ITO-No BR	ITO-BR
Voc [V]	0.494	0.467
Roc [ohm·cm²]	31.9	34.9
Rsc [ohm·cm²]	1715	680
FF [-]	0.508	0.417

In Figure 31, the Jsc values in the graph are higher than the ones obtained from the EQE measurements. This is due to the difference in the size of the mask that was used in depositing the i-ZnO layer and the back contact. As the area of the i-ZnO was larger, it could have contributed to the additional current during the J-V measurement. Looking at the Voc and Jsc values, the ITO textured sample with the additional i-ZnO back reflector performed better than the sample without the i-ZnO layer. The sample had a higher Jsc and Voc which overall resulted in obtaining a higher efficiency (5.18% as compared to 4.96%). However, the shunt resistance value measured for the sample with the i-ZnO back reflector layer was much lower than the sample without the i-ZnO back reflector layer. Having a low shunt resistance indicates that there might have been some defects in the sample or contamination during its deposition. The series resistance of the sample with the i-ZnO layer was lower, this can be due to the better ohmic contact between the silicon layer and the back contact that is achieved when utilizing an i-ZnO layer.

In Figure 32, the Jsc values decreased after dry etching and are in a similar range to the Jsc values obtained from the EQE measurement. This can justify that having a larger area for the i-ZnO layer did indeed contribute in additional current during the JV measurement and resulted in getting inaccurate results. Moving forward, the shunt resistance values of both samples improved, which can be due to the dry etching process removing defects and impurities that can be found in the Si bulk layer. The series resistance of the sample with the i-ZnO layer did also increase which was not expected. Added to that, the Jsc of the sample with the additional i-ZnO layer can be seen to drop and become lower than the sample without the i-ZnO back reflector. A possible explanation is that the dry etching conditions were not feasible for the layer or the dry etching was not done properly which could have caused additional damage to the cells of the sample.

AZO textured samples with i-ZnO and without i-ZnO layer

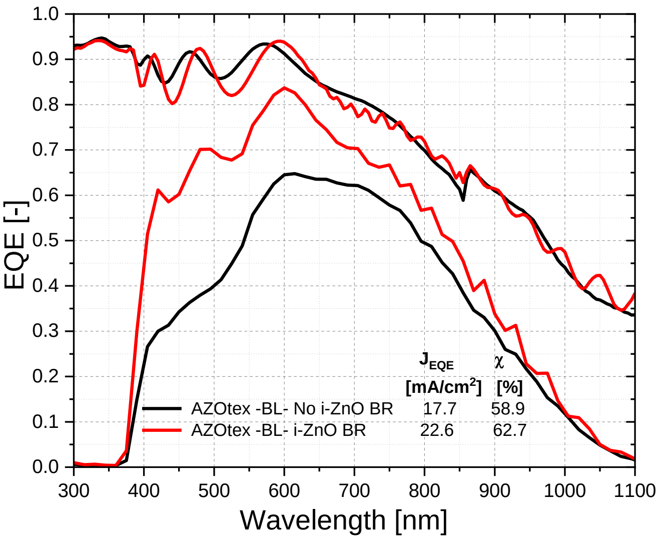

Figure 33 EQE plots of the AZO textured samples with and without an additional i-ZnO back reflector layer

From Figure 33, the optical performance of the AZO textured sample without the i-ZnO layer seems to be much lower than the sample with the additional i-ZnO back reflector. Although the sample without the i-ZnO was expected to have a lower performance, the dramatic decrease in the performance can be attributed to an issue with the deposition of the sample itself. While carrying out the experiments, some of the samples that were deposited showed lower performances than the others and there has been an ongoing issue with the quality consistency of the deposition by the PECVD machine. Thus, although having an additional i-ZnO back reflector layer is expected to benefit the optical performance of the sample, a fair comparison can not be done due to the lower deposition quality of the sample without the i-ZnO back reflector layer. Nevertheless, an interesting result can be seen in the EQE plot of the AZO textured sample with the i-ZnO back reflector layer. When compared to the ITO textured sample containing the i-ZnO layer back reflector that was previously analyzed, the optical performance of the AZO textured sample was relatively lower. There seem to be more fringes in the EQE spectrum of the AZO textured sample at a longer wavelength (700nm to 1100nm) as compared to the ITO textured sample. The presence of fringes at long wavelengths can be correlated with the type of sacrificial texturing used in the sample. As AZO sacrificial texturing creates smaller textures than ITO sacrificial texturing, the deposited i-ZnO back reflector can also have relatively smaller textures as compared to the ITO textured sample. Thus, the i-ZnO back reflector of the ITO textured sample can scatter photons at larger wavelengths more effectively and thus have a higher performance and lower fringes. In addition to that, the fringes in EQE plot at longer wavelengths of the AZO textured sample can also be due to interference with the spectral component of the thick nc-Si:H layer. A possible explanation to the better EQE performance of the ITO textured sample as compared to the AZO textured sample is that a better texturing in the i-ZnO back reflector layer might be achieved with the ITO sacrificial texturing that is able to reflect light better and mitigate the interference with spectral component of the nc-Si:H layer. To verify wither the type of texturing is indeed influencing the performance of the i-ZnO back reflector, an SEM on the samples can be done to observe any differences in the textures of the i-ZnO layer.

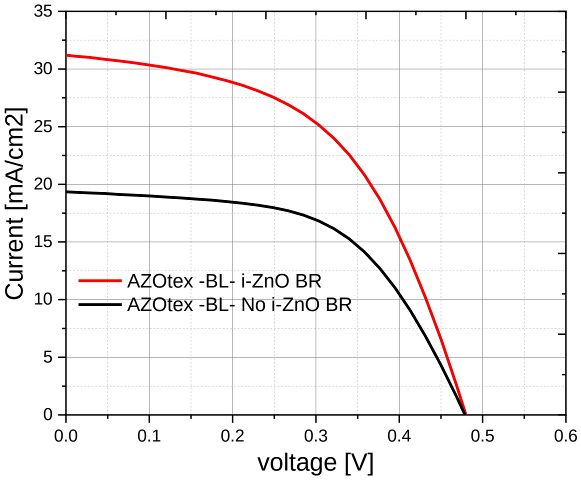

Figure 34 J-V plots of the AZO textured samples with and without an i-ZnO back reflector

Table 12 J-V Results of the AZO textured samples with and without an i-ZnO back reflector

	AZO-BR	AZO-No BR
Voc [V]	0.477	0.478
Jsc EQE [mA/cm²]	22.73	17.6
Roc [ohm·cm²]	21.6	31.3
Rsc [ohm·cm²]	690	1699
FF [-]	0.495	0.545
η[%]	5.36	4.58

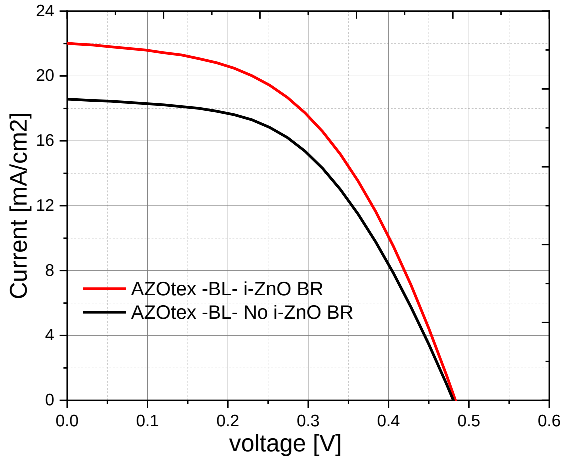

Figure 35 J-V plots of the AZO textured samples with and without an i-ZnO back reflector after DE

Table 13 J-V Results of the AZO textured samples with and without an i-ZnO back reflector after DE

	AZO-BR	AZO-No BR
Voc [V]	0.49	0.474
Roc [ohm·cm²]	30.5	36.7
Rsc [ohm·cm²]	1259	1683
FF [-]	0.512	0.484

From Figure 34, Similar results can be seen from the J-V's of the AZO textured samples as compared to the previously analyzed ITO textured samples. The Jsc results in the plot seem to be much higher compared to the Jsc results from the EQE measurements. This can be attributed to the larger mask size issue of the i-ZnO layer that was explained previously. The presence of an additional i-ZnO back reflector resulted in improving the Jsc and overall efficiency of the cell. The shunt resistance of the sample with the i-ZnO layer was lower, which was also the case with the ITO textured sample. This indicates that the deposition of the i-ZnO layer during this run was not ideal and further optimization of the i-ZnO deposition is needed to produce better cells with fewer contaminations and defects. The series resistance of the sample with the i-ZnO layer was higher, this was expected due to the better ohmic contact and higher electron mobility that can be achieved using an i-ZnO layer.

In Figure 35, the values of the Jsc obtained after dry etching were more comparable with the Jsc values obtained from the EQE results in which was again due to the dry etching process removing the excess area of the i-ZnO layer that was larger than the back contact. The shunt resistance of the sample with the i-ZnO layer seems to have improved significantly while the series resistances of the two samples also seem to have increased. This indicates that the dry etching process needs better control as currently it is likely that the dry etching is damaging the cells while removing the defects in the Si bulk layer.

ITO textured with i-ZnO layer deposited at 25°C vs 300°C

To determine whether the pre-heating temperature influences the performance of the i-ZnO back reflector, an EQE measurement was done on the two ITO textured samples with one sample having its i-ZnO deposited with a heater temperature of 25°C and the other sample with an i-ZnO deposited with a heater temperature of 300°C.

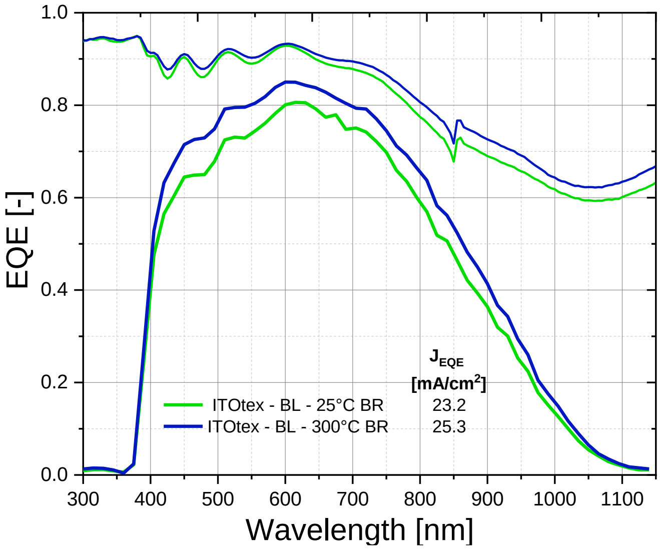

Figure 36 EQE plots of the ITO textured samples with an additional i-ZnO back reflector layer deposited with a heater temperature of 25°C vs 300°C

From Figure 36, the overall spectral utilization of the sample with the i-ZnO layer deposited at a higher heater temperature was better than the other sample. A Jsc of 25.3 mA/cm^2 was generated with the sample processed at a higher heater temperature, while a Jsc of 23.2 mA/cm^2

was generated with the sample processed at a lower heater temperature. Indicating that the use of a higher heater temperature boosted the Jsc of the sample further by 9%. The largest improvement in the EQE can be seen at shorter wavelength ranges between 400nm-900nm in the sample processed with a higher heater temperature. A possible explanation for the overall higher EQE performance with increasing the heater temperature of the i-ZnO layer is that at a higher temperature, complete evaporation of the deposition material occurs, and a higher crystallization and uniformity of the i-ZnO is achieved. The higher crystallization means that the i-ZnO layer is deposited with larger grain size and fewer grain boundaries in the back reflector layer which can improve the natural surface texturing of the i-ZnO layer. Larger surface textures can be achieved resulting in better reflection by the back reflector. Moreover, the improved quality of deposition of the i-ZnO layer allows for better scattering of a larger portion of light that that is reflected by the metal back reflector into the solar cell. Thus a higher portion of photons at shorter wavelengths are scattered and absorbed in the active region of the solar cell. Similarly, photons at larger wavelengths can be reflected better by the i-ZnO layer as fewer grain boundaries are present, which allows higher reflection. Furthermore, a lower parasitic absorption better overall performance can be achieved when depositing the i-ZnO layer using a higher heater temperature. This can be seen in the plot by the smaller gap between the absorption and the EQE plots of the sample processed with a higher heater temperature.

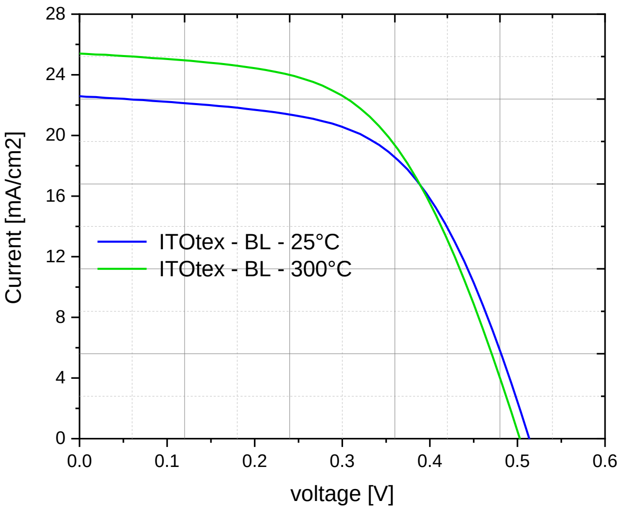

Figure 37 J-V Plots of the ITO textured samples with i-ZnO deposited at 25°C vs 300°C

Table 14 J-V Results of the ITO textured samples with i-ZnO deposited at 25°C vs 300°C

	25°C	300°C
Voc [V]	0.51	0.50
Jsc EQE [mA/cm²]	23.2	25.3
Roc [ohm·cm²]	20.5	14.3
Rsc [ohm·cm²]	807	1082
FF [-]	0.475	0.502
η[%]	5.62	6.35

In Figure 37 the sample with the i-ZnO layer deposited at a higher heater temperature showed a higher electrical performance than the sample in which the i-ZnO was deposited at a lower heater temperature. Using a heater temperature of 300°C resulted in obtaining a higher shunt resistance, which can be attributed to the higher deposition quality and larger crystal size of i-ZnO. This led to obtaining a better FF and higher overall efficiency. Higher series resistance and lower shunt resistance were observed in the sample deposited with a heater temperature of 25°C. This can be due to the larger number of defects and grain boundaries of the i-ZnO when depositing at lower heater temperatures. Moreover, it is also possible due to the presence of contaminants in the sample that hinders the flow of current.

The sample with the i-ZnO layer deposited with a heater temperature of 300°C showed a higher optical and electrical performance. This indicates that depositing an i-ZnO layer using a higher heater temperature has the potential to improve the performance of the cell. For future research, a structured experiment can be conducted with a gradual increase in the heater temperature at a wider range of temperatures. The results can help in determining the optimal heater temperature for depositing the i-ZnO back reflector layer. Furthermore, the influence of the heater temperature on the quality of the deposited i-ZnO layer can be verified by measuring the crystallinity of the deposited i-ZnO layer. For that, a separate experiment can be conducted in which an i-ZnO layer is deposited on a glass sample at different heater temperatures, and the sample is then measured for crystallinity. Another research area would be the influence of the i-ZnO back reflector thickness on the performance of the sample. By conducting an experiment in which the thickness of the i-ZnO layer is varied, it is possible to determine the optimal thickness of the i-ZnO layer.

Key takeaways

The results have suggested that having an additional i-ZnO back reflector can improve the optical performance of the sample further. The low refractive index of the i-ZnO layer promotes photon reflection in the infrared red region and improves the reflection of shorter wavelength photons by the metal back contacts due to better scattering. Depositing the i-ZnO back reflector at higher temperatures further improves the quality of the i-ZnO layer due to the formation of larger crystal sizes and lower grain boundaries.

4.3 TCO Layer

Literature Review

The transparent conductive oxide layer (TCO) serves as an electric front contact in thin-film solar cells by providing a low resistance path for collecting and transporting charge carriers. Moreover, it guides the incident light into the active layer of the solar cell, which is why it needs to be highly transparent in the active wavelength range of the electromagnetic spectrum [9]. To ensure that the TCO layer works efficiently, it must be highly conductive and have a low sheet resistance. Depending on the type of material used for the TCO layer, different surface textures can be made which enhance light scattering into the solar cell and reduce reflection losses. Based on the Drude absorption model, the incident photons at longer wavelengths can interact with the free carriers in the TCO layer resulting in free carrier absorption (FCA) which reduces the performance of the TCO layer. FCA can reduce the refractive index of the TCO at the visible and near-infrared (NIR) wavelength ranges resulting in higher reflection of the incident photons at the front of the solar cell between the TCO layer and Si layer underneath it [1][5]. Moreover, FCA can also increase the extinction coefficient of the TCO layer at the NIR wavelength ranges resulting in light absorption in the TCO layer. To mitigate the effect of FCA a higher refractive index and lower extinction coefficients need to be achieved by increasing the carrier mobility and decreasing the carrier density in the TCO layer [23]. Thus, depending on the TCO material, a trade-off between high transparency and good conductivity is usually present anticipated to the FCA in the TCO layer.

A suitable candidate for the TCO layer is indium tin oxide (ITO) due to its photoelectrical properties. ITO is made up of a mixture containing 90% indium oxide (In_2O_3) and 10% tin oxide (SnO_2) [9]. ITO can provide high electron mobility, a tunable carrier density, and high transparency in the visible and long wavelength regions of the electromagnetic spectrum [22]. Moreover, ITO is among the few TCO material to show a good trade-off between high conductivity and transparency. However, one of the limitations of ITO is that indium has a very low abundance in the earth's crust, with approximately 0.05 ppm. This limits its utilization on large-scale production and raises the cost of ITO as a TCO layer. Another limitation of using ITO as a TCO layer is that at high temperatures, the electrical conductivity of ITO decreases can affect the overall efficiency of the solar cell [22]. Lastly, ITO has been shown have to have low transmittance in the near infrared region (NIR), which limits its performance as a TCO layer [38].

Another promising candidate for a TCO material is hydrogenated indium oxide (IOH). IOH is known to have high electron mobility leading to high conductivity. It also has high transparency in the near-infrared region and low parasitic absorption losses comparable to ITO. Moreover, FCA's influence on IOH is lower compared to ITO thanks to its higher charge carrier mobility. Thus, a lower reflectance rate at the visible and NIR wavelength ranges is achieved when using IOH as a TCO layer compared to ITO. It is possible to achieve high electrical and optical performance in the TCO layer by making a bilayer of two materials. As i-ZnO is known to have higher transparency in the visible and NIR wavelength ranges than ITO, it is possible to use it in making a TCO bilayer along with IOH to achieve higher opto-electrical properties than ITO. Doing so can achieve a TCO with the combined benefit of i-ZnO's higher transparency/low parasitic absorption NIR wavelength ranges and IOH's higher lateral conductivity [39]. Furthermore, using a TCO bilayer (IOH/i-ZnO) can also have the benefit of producing a TCO layer with higher quality as it less prone to defect formation while depositing as compared to ITO. Optimizing the thickness of the TCO bilayer can further influence the performance of the solar cell. By using a thicker IOH layer in the TCO bilayer, it is possible to enhance the lateral conductivity in the TCO layer further as a lower sheet resistance can be achieved [40].

Experimental Details

To observe the effect of having a different TCO layer on the solar cell's performance, nc-Si:H and micromorph samples with different TCO layers were made. Four nc-Si:H samples were deposited, two of which had AZO sacrificial texturing and the other two had ITO sacrificial texturing. In each pair of samples with the same sacrificial texturing, one sample was made an ITO TCO layer (150nm), while the other had a TCO bilayer of IOH and i-ZnO (100nm + 500nm). The ITO was deposited through sputtering using the PECVD machine, by placing a glass sample with sacrificial texturing in the sputtering chamber a layer thickness of 150nm was deposited at a temperature of 206°C. For the TCO bilayer, the IOH layer was deposited at an atmospheric temperature, while the i-ZnO layer was deposited at a temperature of 200°C. All samples had an additional i-ZnO back reflector layer on top of their metal (Ag/Cr/Al) back contacts. A similar process was used in preparing the micromorph samples. To determine if the thickness of the TCO bilayer affects the performance of the solar cell, a micromorph sample with a thicker bilayer (100+1000nm) was made. Once all the samples were deposited, their optical and electrical properties were measured through EQE and J-V measurements. The samples then went through dry etching to observe any changes in the performances of the samples. The cell architecture of the nc-Si:H and micromorph is illustrated in the following figure.

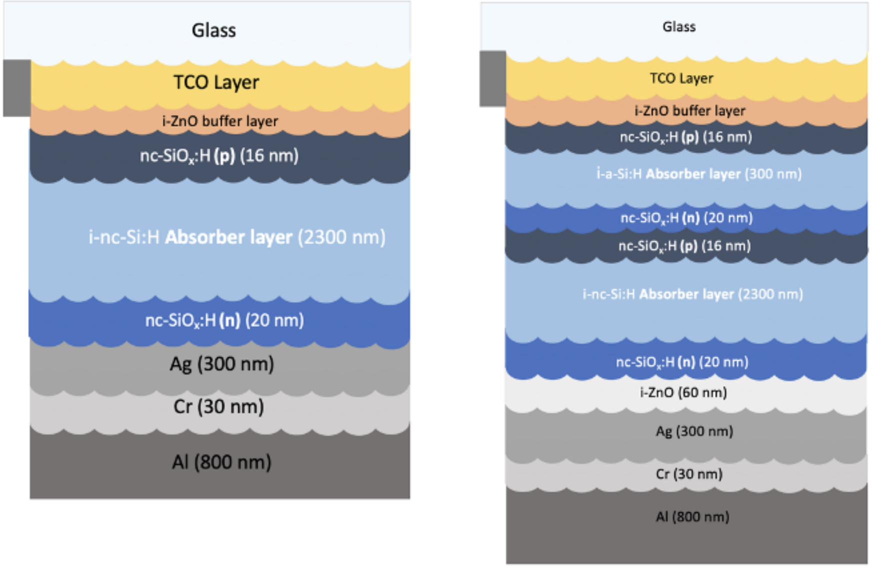

Figure 38 Cross-section of the single junction nc-Si:H cell (on left) and micromorph (on right) of cell architecture.

Results and Discussion

Nc-Si:H

AZO textured samples with ITO vs Bilayer TCO

Observing the optical and electrical performance of the samples can give an idea on how the TCO layer can influence the performance of the solar cell samples.

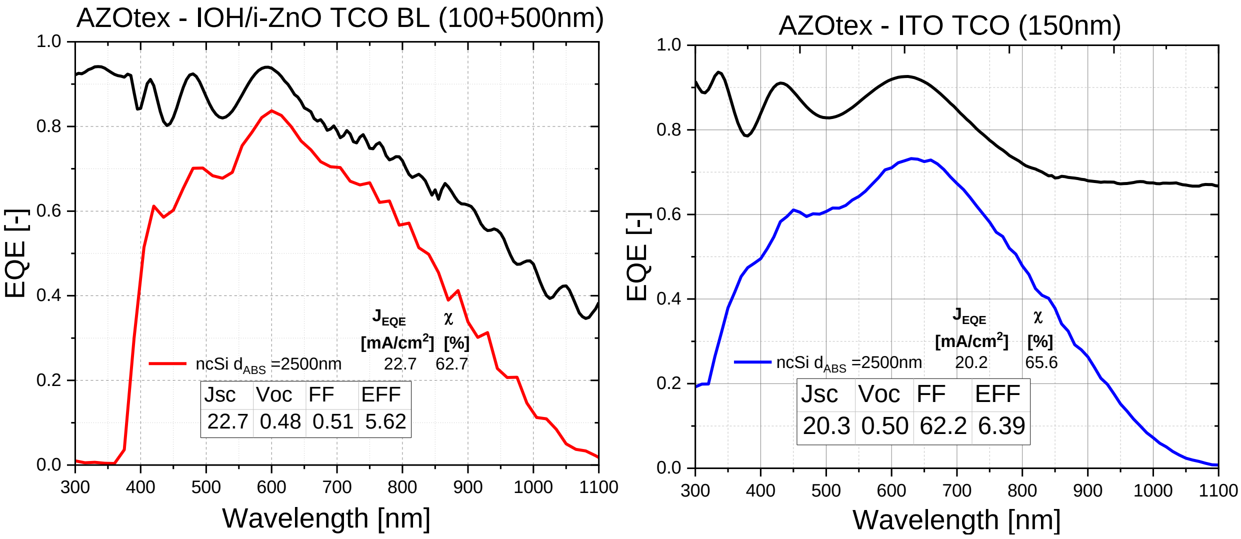

Figure 39 EQE results of the AZO textured samples with TCO BL (on left) and ITO TCO layer (on right)

From the EQE results in Figure 39, the optical performance sample with the TCO bilayer was higher than the sample with the ITO TCO layer. The better spectral utilization of the sample with the TCO bilayer resulted in generating a Jsc of 22.7 mA/cm^2 as compared to 20.3 mA/cm^2 in the sample with the ITO TCO layer, showing an improvement of 11.8% in the Jsc. At a wavelength range of 600nm, the sample with the TCO bilayer had a higher EQE (approx. 0.84) compared to the lower EQE (0.72) in the sample containing the ITO TCO layer at the same wavelength. This indicates that the TCO bilayer was able to transmit more light into the solar cell and have a higher efficiency in conducting the generated current in the sample. This was expected due to the fact that the TCO bilayer has a higher transmittance and higher carrier mobility than ITO TCO layer so it is able conduct the generated current better.

However, comparing the absorption plots in both of the samples, it can be seen that there is higher interference when using a TCO bilayer as compared to an ITO. At a wavelength range of 400-600nm, more fringes appear in the absorption plot of the sample with the TCO bilayer. This can be due to the innate nano texturing nature at the surface of the ITO when compared to the flat surface made by IOH/ iZnO of 500nm refer to Figure 51. This can enhance light scattering at shorter wavelengths in the ITO TCO layer as compared to the TCO bilayer. At larger wavelengths (700nm-1100nm) there seems to be a much larger interference in the absorptance of the sample with the TCO bilayer. This can be correlated to the fact that the ITO TCO layer can follow the texture of the glass underneath it better as compared to the TCO bilayer which has been shown to have non-conformal deposition on the textured glass resulting it to have a flatter surface. This can further indicate that the nano-sized textures created using AZO sacrificial texturing in combination with the TCO bilayer are not efficient in scattering photons at longer wavelengths and a poorer red response is achieved. Thus, to ensure better light scattering when using a TCO bilayer, the texturing in the bilayer needs to be enhanced further to ensure better scattering. Absorption in active layer of the sample with the ITO TCO layer starts at 300nm (approx. 0.20) while the bilayer TCO starts at 380nm which is a result of ITO Higher bandgap of TCO in comparison with bilayer.

Observing the electrical performance of the samples can help in determining wither using TCO bilayer does indeed improve the performance of the cell and can help in observing if the sample had issues during their deposition.

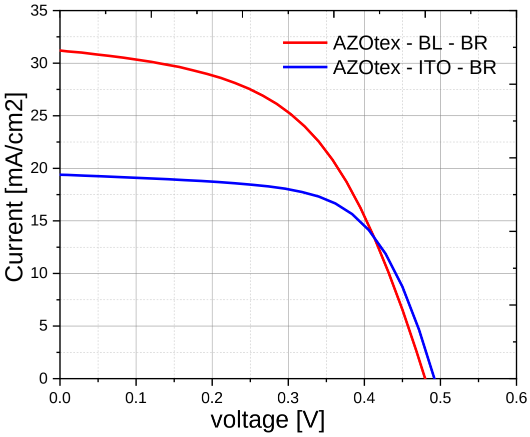

Figure 40 J-V plots of the AZO textured samples with TCO BL vs ITO TCO layer

Table 15 J-V Results of the AZO textured samples with TCO BL vs ITO TCO layer

	BL	ITO
Voc [V]	0.48	**0.51**
Jsc EQE [mA/cm²]	22.73	**20.2**
Roc [ohm·cm²]	17.88	**12.04**
Rsc [ohm·cm²]	758	**1398**
FF [-]	0.515	**0.613**
ŋ[%]	5.62	**6.32**

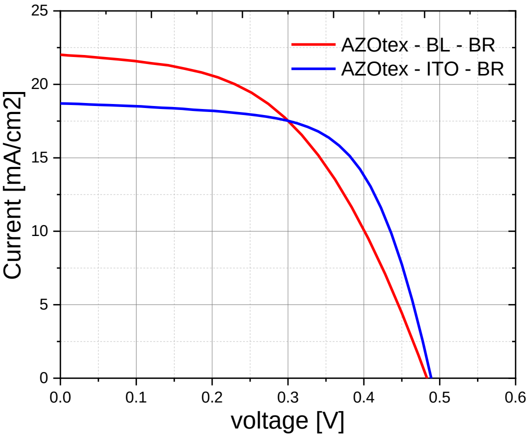

Figure 41 J-V plots of the AZO textured samples with TCO BL vs ITO TCO layer after DE

Table 16 J-V Results of the AZO textured samples after RIE

	BL	ITO
Voc [V]	0.49	**0.51**
Roc [ohm·cm²]	30.5	**12.4**
Rsc [ohm·cm²]	1258	**1741**
FF [-]	0.512	**0.622**

From the J-V results displayed in Figure 40, the sample with the ITO TCO layer had a better overall performance than the sample with the TCO bilayer. This result contradicts the literature, the use of the bilayer is expected to improve the conduction of the TCO and have a lower parasitic absorption, improving the cell's performance. The difference in the performance of the samples here may not be mainly due to the use of a different TCO layer but rather due to the deposition of the samples themselves. The samples were made during different runs, and there has been an ongoing issue with the consistency in the quality of the deposition by the PECVD machine. Thus, comparing the J-V results might not be a fair comparison as the sample with the TCO bilayer might have experienced a lower quality of deposition due the presence of contamination or poor control of the silane flow rate during the deposition.

Looking at the J-V plots, it can be seen that before dry etching, the sample with the TCO bilayer had a much higher Jsc in the J-V plot and after dry etching, the Jsc decreased and became lower than the sample with the ITO TCO layer. The considerable drop in Jsc from the J-V plots of the sample containing the TCO bilayer was mainly due to the processing difference that it went through. During the run in which the sample with the TCO bilayer was deposited, the i-ZnO back reflector was deposited with a mask size of 5x5mm, while the metal (Ag/Cr/Al) back reflector was deposited with a smaller mask size of 4x4mm. On the other hand, in the sample with the ITO TCO layer, the same mask (size 5x5mm) was used for depositing the i-ZnO back reflector layer and the metal (Ag/Cr/Al) back reflector layer. The larger area of the i-ZnO layer has contributed to inaccurate Jsc values when measured using Wacom. Nevertheless, from Table 16, it can be seen that dry etching did improve the shunt resistance values of the samples mainly due to removing impurities and defects in the bulk silicon layer. The increase in the series resistance of the sample with the TCO bilayer indicates that the dry etching process might have unintentionally damaged the cell, lowering the conductivity of the sample.

ITO textured samples with ITO vs Bilayer TCO

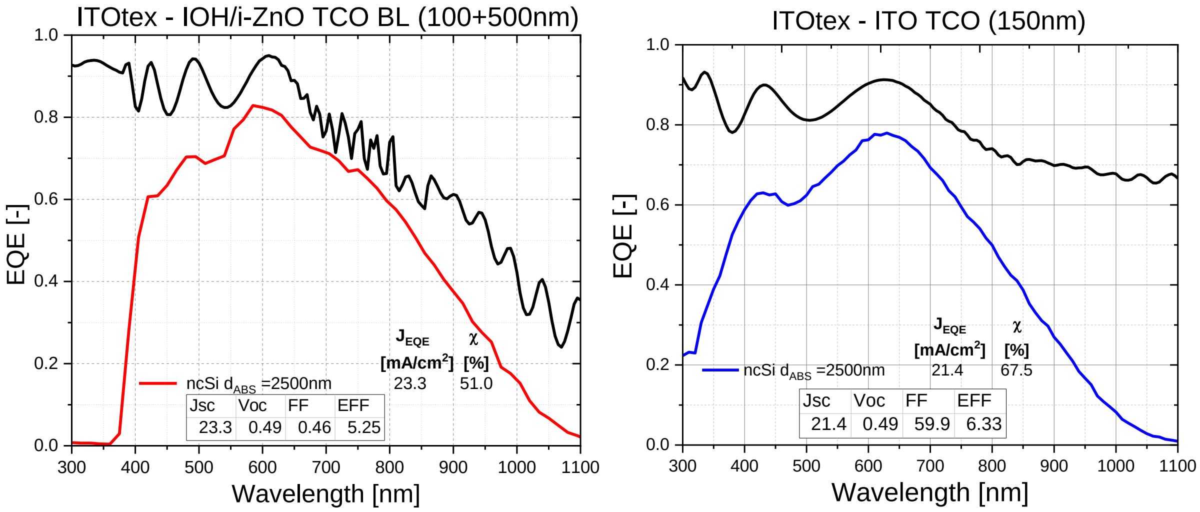

Figure 42 EQE results of the ITO textured samples with TCO BL (on left) and ITO TCO layer (on right)

In Figure 42, a similar optical performance trend can be seen with the ITO-processed samples to that of the AZO-processed samples that were previously analyzed. Overall, the optical performance of the sample with the TCO bilayer surpassed the optical performance of the sample with the TCO ITO layer. The highest EQE achieved in the sample with the TCO bilayer was 0.83 at a wavelength of 600nm, while the EQE was around 0.77 in the other sample at the same wavelength. The higher spectral utilization of the sample with bilayer resulted in generating a Jsc of 23.3 mA/cm^2 compared to 21.4 ma/cm^2 in the sample containing the ITO TCO layer resulting in an improvement of 8.9%. Comparing the ITO-processed sample with the TCO bilayer to the AZO-processed sample with the TCO bilayer that was previously analyzed, the ITO-processed sample had a higher spectral utilization. This can be attributed to the larger craters of the ITO sacrificial texturing, that is quite efficient to scatter light at longer wavelengths. The difference in the absorptance fringes in the TCO bilayer and the ITO TCO sample can be related to the natural surface texturing of the ITO layer and the non-conformal nature of deposition with the bilayer that was previously explained.

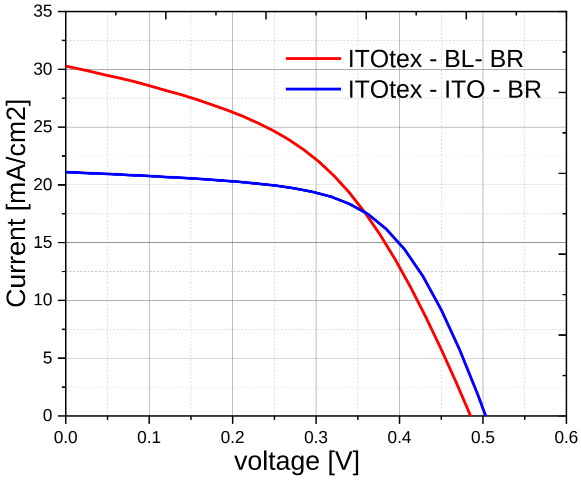

Figure 43 J-V plots of the ITO textured samples with TCO bilayer vs ITO TCO layer

Table 17J-V Results of the ITO textured samples with BL vs ITO TCO layer

	BL	ITO
Voc [V]	0.49	**0.49**
Jsc EQE [mA/cm²]	23.3	**21.4**
Roc [ohm·cm²]	25.9	**10.11**
Rsc [ohm·cm²]	380	**1052**
FF [-]	0.46	**0.601**
η[%]	5.25	**6.3**

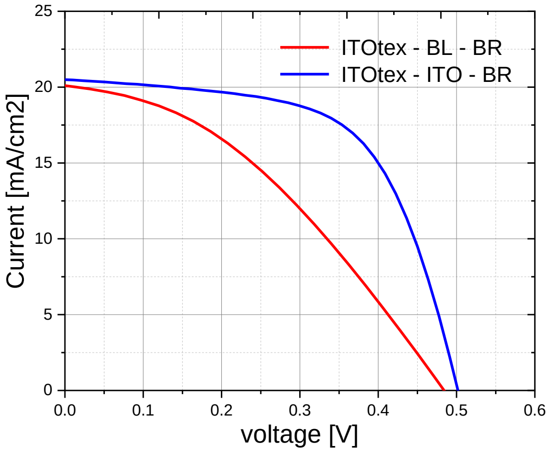

Figure 44 J-V plots of the ITO textured samples with TCO Bilayer vs ITO TCO layer after DE

Table 18 J-V Results of the ITO textured samples after dry etching

	BL	ITO
Voc [V]	0.467	**0.50**
Roc [ohm·cm²]	35	**13.6**
Rsc [ohm·cm²]	680	**1267**
FF [-]	0.42	**0.60**

As was seen in the results of the samples with the AZO sacrificial texturing, the samples with the ITO sacrificial texturing in Figure 43 and Figure 44 have shown a similar trend in the results. The sample containing the TCO bilayer had a lower overall performance than the sample with the ITO TCO layer. This was again due to the fact that these samples were deposited during separate runs, and there has been inconsistency with their deposition. To lower the chances of inconsistency with the quality of the deposition faced by the samples, it is important to check the deposition setup and ensure that the flow rate of gases in the deposition chambers is ideal before starting the deposition.

Micromorph

AZO textured samples with ITO vs Bilayer TCO.

Observing the optical performance of the micromorph samples can help in understanding the influence of the TCO layer on the spectral utilization of the sample.

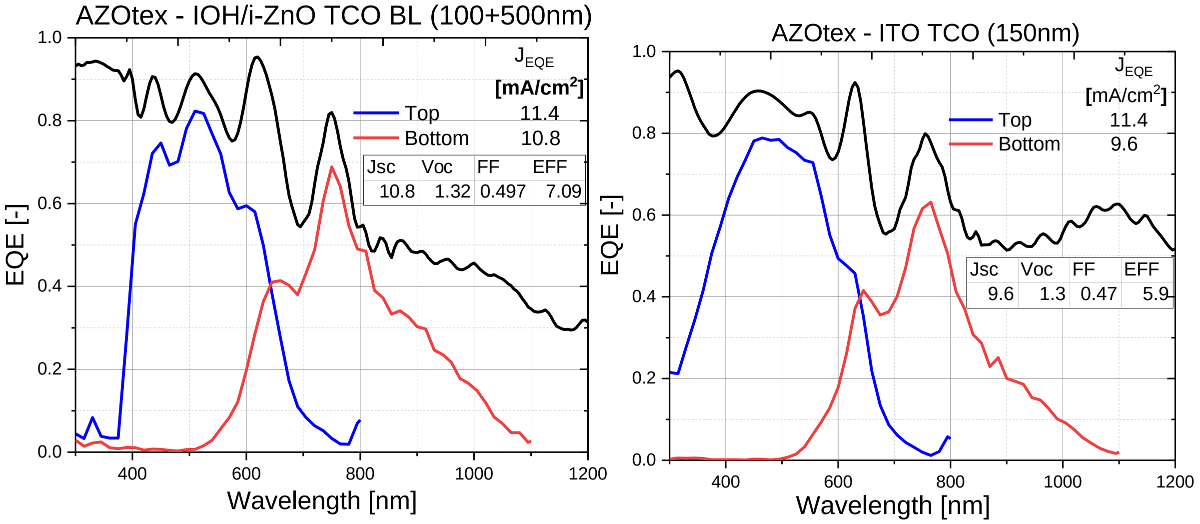

Figure 45 EQE results of the AZO textured micromorph samples with TCO BL (on left) and ITO TCO layer (on right)

In Figure 45, the sample with the TCO bilayer showed a higher spectral utilization with a total Jsc of 22.2 mA/cm^2 as compared to the sample with the TCO ITO layer with a Jsc of 21 mA/cm^2, resulting in an improvement of 5.71%. The higher performance of the sample with the TCO bilayer can be attributed to the higher transparency and lateral conductivity. However, when inspecting the absorptance plots, the sample with the ITO TCO layer seems to have lower fringes in the EQE plot of its top cell at a wavelength range of 400nm-600nm, which is correlated with the higher absorptance at that range as compared to the sample with TCO bilayer. This can be correlated to natural texture of the surface of the ITO material as compared to the bilayer.

Moving forward, at a wavelength range of 600-800nm, similar fringes can be seen in both of the samples related to the optical cavity of the top cell in a micromorph sample. When light passes through the a:Si-H top cell it can interfere and reduce the optical performance the solar cell. A possible way to mitigate this effect is by using an intermediate reflective layer (IRL). Lastly, at a wavelength range of 800-1100nm, better performance can be seen with the sample containing the TCO bilayer. This is explained with the fact that the free carrier absorption of doped tin oxide is higher than intrinsic zinc oxide.

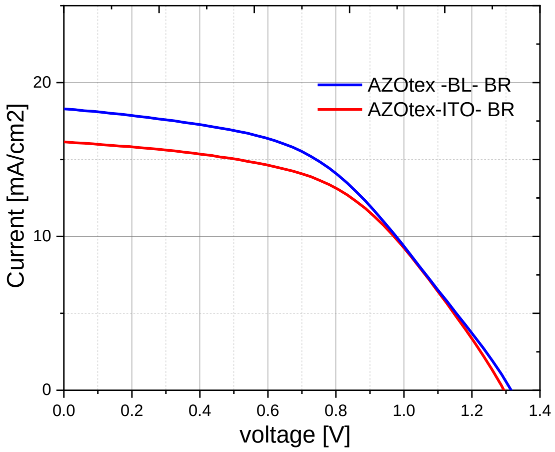

Figure 46 J-V plots of the AZO textured samples with the bilayer vs ITO TCO layer

Table 19 J-V Results of the AZO textured samples with Bilayer vs ITO TCO layer

	BL	ITO
Voc [V]	1.32	1.3
JscEQE TOP [mA/cm^2]	11.4	11.4
JscEQE Bottom [mA/cm^2]	10.8	9.6
Roc [ohm·m^2]	74.6	78.6
Rsc [ohm·m^2]	4021	4175
FF [-]	0.497	0.473
η[%]	7.09	5.90

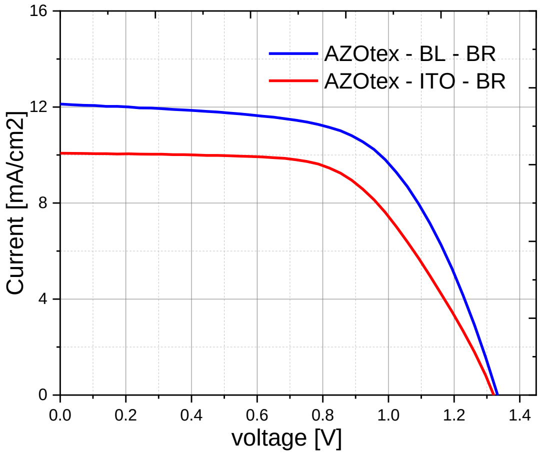

Figure 47 J-V plots of the AZO textured samples with Bilayer vs ITO TCO layer after DE

Table 20 J-V Results of the AZO textured samples with Bilayer vs ITO after DE

	BL	ITO
Roc [ohm·m^2]	88.9	100
Rsc [ohm·m^2]	9462	8890
FF [-]	0.612	0.561

In Figure 46, the sample with the TCO Bilayer had a higher performance than the sample with ITO TCO layer. This was expected as the TCO bilayer has low parasitic absorption and good lateral conductivity as compared to the ITO TCO layer. The FF of the sample with the bilayer was higher, which along with the slightly higher Voc and Jsc resulted in a higher overall efficiency of 7.09%. Overall the two samples showed a high series resistance, indicating that the deposition of the samples was not ideal as the flow of current is hindered in the sample. A possible reason for the high series resistance could be that the deposition of the absorber layer in the PECVD machine was not done properly due to the presence of dust particles or other contaminants in the chamber.

From the J-V plots after dry etching displayed in Figure 47, the Jsc values decreased and are comparable to the Jsc values obtained from the EQE measurement that were displayed in Table 19. This was mainly due to the fact that during this run, the i-ZnO back reflector layer was deposited with a larger mask size (5x5mm) than the back contact that was deposited with a mask size of (4x4mm). As was seen in the previous results, the larger area of the i-ZnO layer contributed in additional current during J-V measurements. Comparing the series resistance values before and after dry etching, it can be seen that the series resistance values increased and the shunt resistance values also increased significantly. Although dry etching has been shown to reduce series resistance by removing the contaminants and residues in the silicon layer that hinder the electrical conductivity. The increase in series resistance after dry etching indicates that the process might have unintentionally introduced factors that obstruct the flow of the current in the cell, such as damage to the cells due to over-etching. Even though dry etching is expected to increase the shunt resistance in the solar cell, the shunt resistance results were much higher than expected. As dry etching was carried out for the first time during that run, the process was not controlled optimally as many of the back contacts in the cells were also removed, indicating that the process led to over-etching refer to Figure 56. Thus the J-V results after etching are not precise as many of the cells were damaged during the dry etching process of that run.

ITO textured samples with ITO vs Bilayer TCO

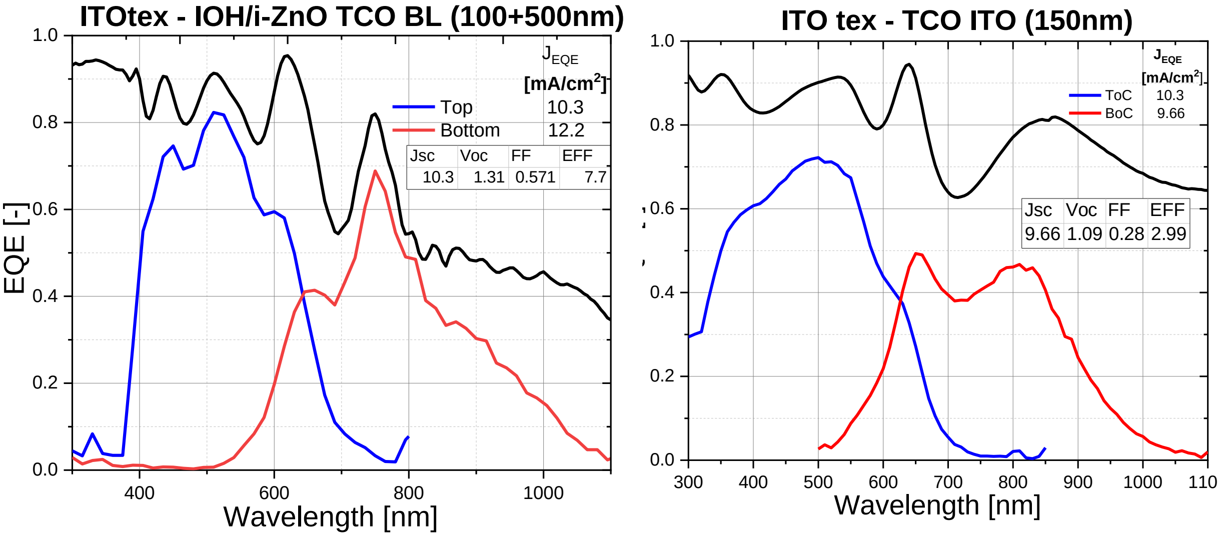

Figure 48 EQE results of the ITO textured micromorph samples with TCO Bilayer (on left) and ITO TCO layer (on right)

In Figure 48, the spectral utilization of the sample with the TCO bilayer is higher, generating a Jsc of 22.5 mA/cm^2 as compared to 21.1 mA/cm^2 in the ITO TCO. This is similar to what was observed in the AZO textured samples previously analyzed. Having a TCO made of a bilayer (IOH/i-ZnO) provides better transparency, higher lateral conductivity, and lower parasitic absorption than ITO, which overall improves the performance of the sample. Comparing the AZO textured sample with the TCO bilayer to the ITO textured sample with the bilayer, the ITO processed sample performed slightly better (Jsc of 22.5 mA/cm^2 compared to 22.2 mA/cm^2). The larger craters formed using ITO sacrificial texturing can improve the scattering of light at longer wavelengths.

A similar trend can be seen in the absorptance plot of the ITO-processed sample with the TCO bilayer that was also previously seen with the AZO-processed sample containing the TCO bilayer. The fringes in the absorptance plot indicate that further optimization in the texturing and thickness of the TCO bilayer are necessary in order to reduce the interference of the TCO layer with the incident photons. Looking closer at the absorptance plots at longer wavelengths, the sample with the ITO layer had a higher absorptance yet showed poorer performance in the EQE of its bottom cell. A possible reason could be due to an inconsistency with the deposition quality of the bottom cell. Looking at the gap between the absorptance plots and the EQE plots, the sample with the TCO ITO layer had a larger gap compared to the sample with the TCO bilayer, which indicates that the sample with the ITO TCO layer had a larger parasitic absorption. Although the ITO TCO layer had a lower thickness, it showed a larger parasitic absorption which can be attributed to the lower transparency and larger number of defects found in the ITO as compared to bilayer of IOH and i-ZnO.

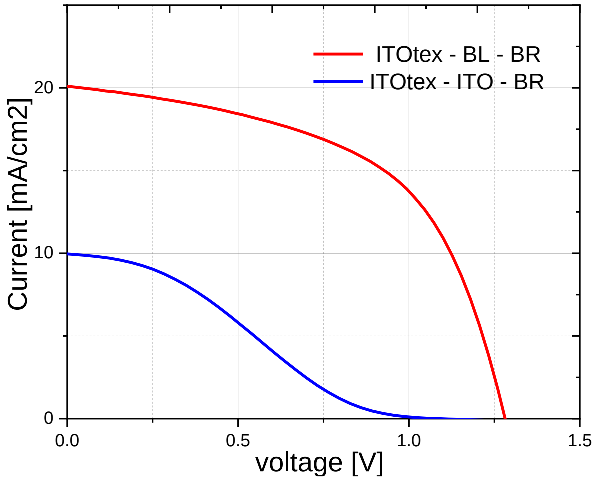

Figure 49 J-V plots of the ITO textured samples with Bilayer vs ITO TCO layer

Table 21 J-V Results of the ITO textured samples with Bilayer vs ITO TCO layer

	BL	ITO
Voc [V]	1.31	1.09
JscEQE TOP [mA/cm^2]	10.3	11.4
JscEQE Bottom [mA/cm^2]	12.2	9.66
Roc [ohm·m^2]	43.6	492
Rsc [ohm·m^2]	3492	2155
FF [-]	0.571	0.284
η[%]	7.70	2.99

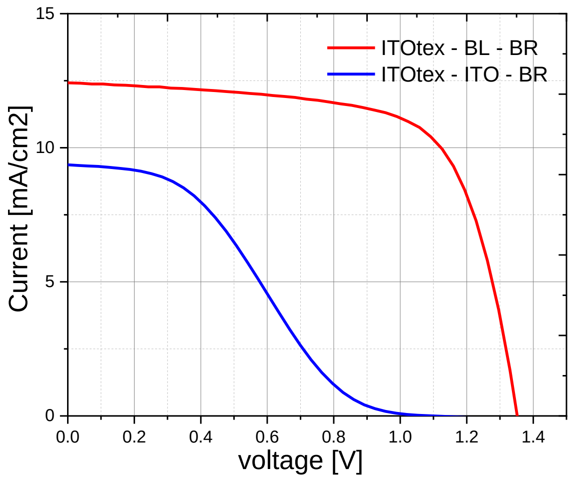

Figure 50 J-V plots of the ITO textured samples with Bilayer vs ITO TCO layer after DE

Table 22 J-V Results of the ITO textured samples with Bilayer vs ITO after DE

	BL	ITO
Voc [V]	1.34	1.1
Roc [ohm·m^2]	52.6	572
Rsc [ohm·m^2]	8755	5468
FF [-]	0.673	0.316

In Figure 50, the performance of the ITO textured sample with the ITO TCO layer was much lower than the other sample with the TCO Bilayer. It is worth noting that the two samples were deposited during different runs, and there has been an issue with the deposition of the ITO TCO layer. When the thickness of the ITO layer was inspected, it was seen to be thinner (120nm) than what was aimed for (150nm) and had high resistance. Thus, although it is expected that the sample with the TCO bilayer to have higher electrical performance, a fair comparison from the J-V results cannot be made as the sample with the ITO TCO layer faced issues with its deposition.

After dry etching, the shunt resistance and the series resistance values increased as displayed in Table 22. This trend was also seen in the samples that were previously analyzed. The increase in the series resistance can be due to the dry etching process unintentionally damaging the conductive layer in the cell refer to Figure 56. Although an increase in the shunt resistance is expected with dry etching, the sample with the TCO bilayer showed a much higher increase which can be inaccurate as the cells of the sample were damaged due to the dry etching.

ITO textured samples with Bilayer (100+500nm) vs (100+1000nm)

To determine the influence of the having a thicker bilayer on the performance of the sample, it is important to inspect the grain size and the crystal structure in the TCO bilayer on a molecular level. Thus, SEM images of the two bilayers were taken and are illustrated in Figure 51.

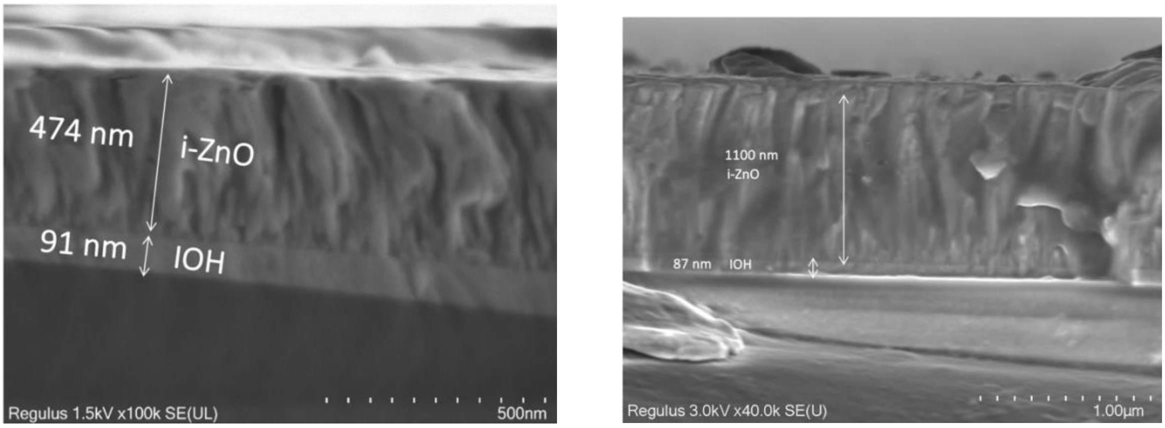

Figure 51 SEM images of the TCO BL (100+500nm) on the left and (100+1000nm) on the right

The thicker bilayer resulted in i-ZnO crystals with larger crystal grain sizes. Larger crystal grain sizes can reduce the interference of the TCO layer with incident light as there are smaller number of grain boundaries and defects that can interfere with the incident photon. This results in an increased transparency as the path length of light in the TCO layer is decreased, and lower absorption in the TCO layer occurs. Furthermore, another benefit that may be achieved when using a thicker bilayer is that the larger crystal sizes of the i-ZnO can be textured better as they are grown vertically on the glass sample. The extent to which the surface of the TCO layer is textured is higher with the thicker bilayer as the larger crystal sizes are affected to a larger extent by the texturing in the glass underneath them. This cannot be seen in the SEM images here, as the TCO bilayers were deposited on flat glass samples. In Figure 51, the samples have shown a slight deviation from the aimed thickness of 100nm+500nm in the sample on the left and the 100+1000nm in the sample on the right. This indicates that the flow rates used for the TCO deposition need further tuning to achieve the desired thicknesses.

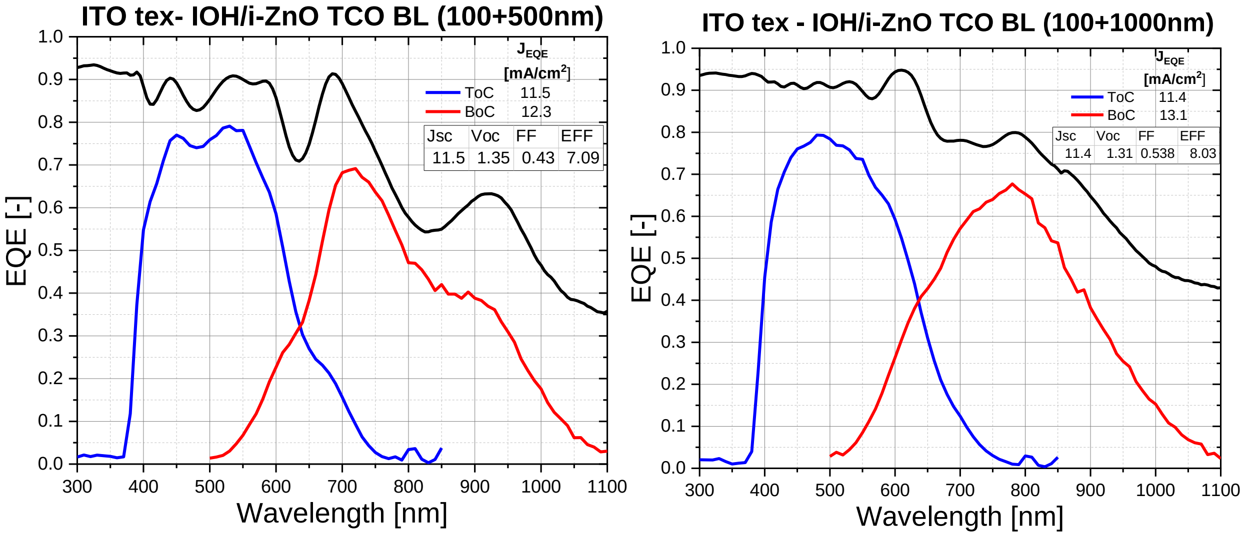

Figure 52 EQE results of the ITO textured micromorph samples with TCO Bilayer 100+500nm (on left) and TCO BL 100+1000nm (on right)

From the EQE results displayed in Figure 52, the spectral utilization of the sample with the thicker bilayer (100+1000nm) was higher, generating a total current of 24.5 mA/cm^2 as compared to 23.8 mA/cm^2 in the sample with a thinner bilayer (100+500nm). At a wavelength range of 400-500nm, the fringes in the absorptance values of the sample with the thinner bilayer were much more significant than in the sample with a thicker bilayer. This indicates that the effect of interference by the TCO layer seen in the samples from previous runs has been mitigated using a thicker bilayer. A possible explanation for the higher absorptance when using a thicker bilayer can be attributed to the grain size of the i-ZnO in the bilayer, which was inspected in the SEM images that were previously analyzed. Having larger crystals and fewer crystal grain boundaries in the sample with the thicker bilayer can increase the transparency and reduce the interference with incident photons. Thus, a more significant portion of the incident light passes into the solar cell's active layer, resulting in higher absorption and a higher current generation.

Inspecting the absorptance plots at a wavelength range of 600-700nm, the fringe related to the optical cavity of the top cell are much smaller in the sample with the thicker bilayer. A possible reason can be correlated to the higher scattering of light achieved with using the thicker bilayer as compared to the thinner bilayer which leads to higher absorptance of light in the a-Si:H top cell. This reduces the amount of light at short wavelength ranges reaching the tunnel recombination junction between the top and bottom cell and thus lower optical cavity effect is observed. At larger wavelength ranges (800nm-1100nm), the sample with the thinner bilayer showed a significantly large fringe in its absorptance plot, which reduced the performance in the bottom cell. Comparing the sample with the thicker bilayer, the fringe in the absorptance at larger wavelengths is absent, and the bottom cell performed much better. This can be due to the better surface texturing of the i-ZnO of the thicker bilayer. As larger crystal grain sizes are formed when depositing a thick bilayer, better surface texturing of the i-ZnO layer is achieved which can scatter light at long wavelength ranges more effectively.

As the current generated by the top cell of the sample is smaller than the current generated by the bottom cell of the sample, the cells current output is limited by the top cell due to the current mismatch. This reduces the potential of the total current that can be achieved by the sample. To optimize the cell with the ticker bilayer further, the top cell of the sample needs to be improved further in order to achieve current matching. Alternatively, an intermediate reflective layer can be utilized in order to increase the output current of the top cell.

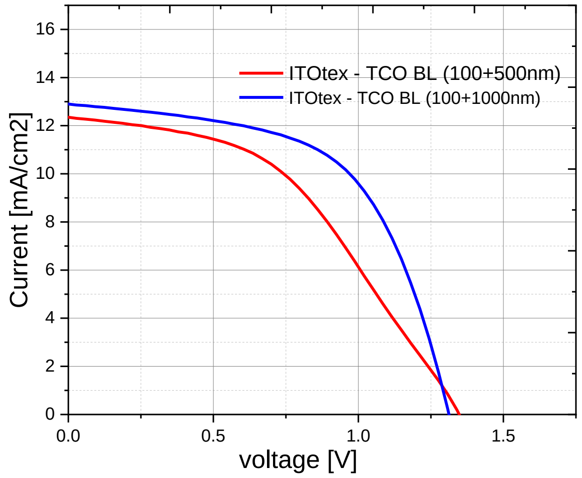

Figure 53 J-V plots of the ITO textured sample with Bilayer (100+500nm) vs Bilayer (100+1000nm)

Table 23 J-V Results of the ITO textured sample with Bilayer (100+500nm) vs Bilayer (100+1000nm)

	BL1	BL2
Voc [V]	**1.35**	**1.31**
JscEQE Top [mA/cm²]	**11.5**	**11.4**
JscEQE Bot [mA/cm²]	**12.3**	**13.1**
Roc [ohm·m²]	**103**	**57.7**
Rsc [ohm·m²]	**2989**	**3499**
FF [-]	**0.429**	**0.538**
η[%]	**6.66**	**8.03**

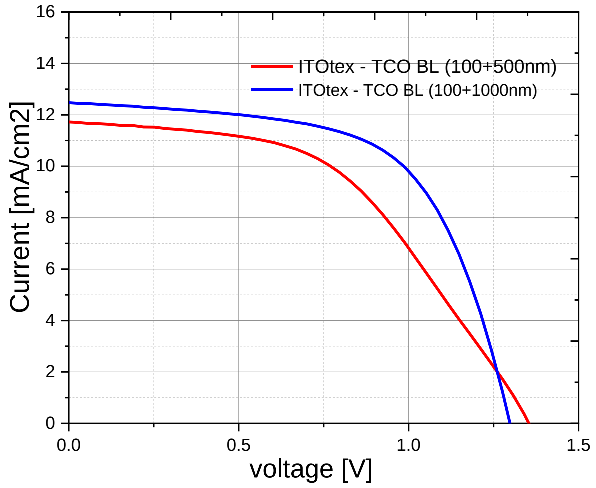

Figure 54 J-V plots of the ITO textured sample with Bilayer (100+500nm) vs Bilayer (100+1000nm) after DE

Table 24 J-V Results of the ITO textured sample with Bilayer (100+500nm) vs Bilayer (100+1000nm) after DE

	BL1	BL2
Voc [V]	**1.35**	**1.32**
JscEQE Top [mA/cm²]	**11.5**	**11.5**
JscEQE Bot [mA/cm²]	**11.8**	**12.4**
Roc [ohm·m²]	**90.2**	**53.3**
Rsc [ohm·m²]	**4499**	**5842**
FF [-]	**0.461**	**0.605**
η[%]	**7.16**	**9.18**

In Figure 53, the thinner bilayer (100+500nm) sample had much higher series resistance (almost double) than the sample with the thicker bilayer. This can be attributed to the lower sheet resistance achieved when using a thicker bilayer which improves the electrical conductivity in the layer. Moreover, the thicker bilayer's larger cross-sectional area enhances the layer's current collection, reducing the losses due to series resistance. The higher shunt resistance of the sample with the thicker bilayer resulted in a larger FF, which led to an overall higher efficiency of 8.03% compared to 6.66% in the sample with the thinner bilayer. The higher shunt resistance in the sample with the thicker bilayer can be attributed to reduced crystal grain boundaries and defects in i-ZnO crystals in the TCO layer.

After conducting dry etching, the results displayed in Table 24 have shown a decrease in the series resistance and an increase in the shunt resistance values. The parameters used during this run for dry etching were optimized based on the parameters used in the previous run in which over-etching occurred. As can be seen, the performance of the samples improved, and the results are in the expected range. The dry etching process can reduce the amount of contaminants and defects in the sample's silicon bulk layer, improving its shunt resistance. Similarly, as contaminants in the sample are reduced, the current flow within the cell can increase, reducing the series resistance.

Key takeaways

Based on the results obtained from this experiment, it can be concluded that the use of a TCO bilayer instead of an ITO layer has improved the performance of both nc-Si:H and micromorph samples. The TCO bilayer provided higher transmittance and carrier mobility than the ITO TCO layer, which mediated its higher interference due to inefficient texturing. Using a thicker bilayer (100+1000nm) resulted in improving the performance of the sample further and reduced the interference with incident photons as compared to a thinner bilayer (100+500nm). In order to determine the optimal thickness of the TCO Bilayer, a structured experiment needs to be conducted in which the thickness of the i-ZnO layer in the bilayer is increased gradually at smaller intervals (i.e. 100nm) at a range of 500nm-1500nm in order to determine an optimal thickness in which the sample has the highest performance.

Chapter 5: Conclusion

This project addressed four main research questions:

1. Which processing conditions in terms of precursor gas flow rate is ideal for hydrogenation of nc-Si:H deposition?
2. How does the texturing of superstrates influence the performance of nc-Si:H and micromorph tandem cells?
3. How will the solar cell benefit optically with an additional intrinsic Zinc Oxide layer back reflector layer?
4. Does a TCO bilayer improve the performance of nc-Si:H and micromorph cells?

Varying the hydrogen flow rate resulted in better control over the nc-Si:H deposition, as consistent quality and performance were observed in the samples. A crystalline volume fraction of approx.60% resulted in the highest performance of the nc-Si:H. By calibrating the PECVD machine, it was concluded that a silane concentration of 2.3 - obtained using a hydrogen flow rate of 120 sccm and a silane flow rate of 3.2 sccm, resulted in nc-Si:H with a crystalline volume fraction with sufficient passivation by amorphous tissue.

The use of i-ZnO and ITO sacrificial texturing resulted in comparably high optical performance in nc-Si:H samples. The lowest performance was obtained with AZO sacrificial texturing. The size and depth of the craters created by sacrificial texturing played an essential role in the effective scattering of photons with comparable wavelengths. Micro-sized craters with hemispherical characters were created by ITO sacrificial texturing, while nano-sized craters with non-hemispherical characters were created by AZO sacrificial texturing. Micromorph samples with ITO sacrificial texturing showed the highest optical utilization (Jsc 24.6 mA/cm^2). The micro-texturing obtained using ITO sacrificial layer was effective in scattering incident light and growing a sample with higher quality. Using an MST (ITO+i-ZnO) sacrificial texturing also resulted in a comparably high optical utilization (Jsc 24.3 mA/cm^2). Using MST (ITO+AZO) and AZO sacrificial texturing in micromorph samples resulted in lower optical utilization due to ineffective light scattering.

Using an additional i-ZnO back reflector layer boosted the solar cell's performance as it resulted in higher optical utilization. The high bandgap and low refractive index of i-ZnO promoted the reflection in the infrared region while the scattering of shorter wavelength photons by the metal back contact was also improved. An improvement of 11% in the spectral utilization (Jsc) of the ITO sacrificial textured sample was observed with the use of an additional i-ZnO back reflector. Using a higher heater temperature to deposit the i-ZnO back reflector improved the spectral utilization (Jsc) of the sample further by 9%.

Using a TCO bilayer of IOH and i-ZnO resulted in higher optical and electrical performance in both nc-Si:H and micromorph samples. A spectral utilization improvement of approx. 9-11% was observed in nc-Si:H samples, while the spectral utilization of micromorph samples improved by approx. 6-7%. The results showed higher transmittance and better conductivity in the samples with the TCO bilayer, although the texturing of the bilayer needs further optimization. Using a TCO Bilayer with a higher thickness (100+1000nm) instead of (100+500nm) offered an additional boost in the optical performance of the cell by 3% and resulted in lower interference.

The highest optical utilization in a micromorph sample during this project was 24.5 mA/cm^2, which was achieved using the combination of parameters explained in the above results. Using ITO sacrificial texturing for effective light scattering, a Thick TCO bilayer (100+1000nm) for better transmittance and conductivity, and an i-ZnO back reflector for higher reflection have resulted in a micromorph sample with the highest optical and electrical properties. By optimizing the texturing of the TCO layer, determining the optimal TCO BL thickness, and incorporating an additional intermediate reflective layer, it is possible to improve the performance of the micromorph sample further.

References

[1] "EIA projects 48% increase in world energy consumption by 2040." https://www.eia.gov/todayinenergy/detail.php?id=26212 (accessed Aug. 01, 2023).

[2] E. Institute, "Energy system struggles in face of geopolitical and environmental crises," *Energy Institute*. https://www.energyinst.org/exploring-energy/resources/news-centre/media-releases/ei-statistical-review-of-world-energy-energy-system-struggles-in-face-of-geopolitical-and-environmental-crises (accessed Aug. 01, 2023).

[3] "Key findings – World Energy Outlook 2022 – Analysis," *IEA*. https://www.iea.org/reports/world-energy-outlook-2022/key-findings (accessed Aug. 01, 2023).

[4] "2022 year-to-date temperatures versus previous years | Annual 2022 Global Climate Report | National Centers for Environmental Information (NCEI)." https://www.ncei.noaa.gov/access/monitoring/monthly-report/global/202213/supplemental/page-1 (accessed Aug. 01, 2023).

[5] "The Paris Agreement | UNFCCC." https://unfccc.int/process-and-meetings/the-paris-agreement (accessed Aug. 01, 2023).

[6] "Renewables - Energy System," *IEA*. https://www.iea.org/energy-system/renewables (accessed Aug. 01, 2023).

[7] T. Söderström, F.-J. Haug, V. Terrazzoni-Daudrix, and C. Ballif, "Flexible micromorph tandem a-Si/c-Si solar cells," *J. Appl. Phys.*, vol. 107, pp. 014507–014507, Feb. 2010, doi: 10.1063/1.3275860.

[8] M. A. Fazal and S. Rubaiee, "Progress of PV cell technology: Feasibility of building materials, cost, performance, and stability," *Sol. Energy*, vol. 258, pp. 203–219, Jul. 2023, doi: 10.1016/j.solener.2023.04.066.

[9] A. Smets, K. Jäger, O. Isabella, R. van Swaaij, and M. Zeman, *Solar Energy: The physics and engineering of photovoltaic conversion, technologies and systems*. Cambridge: UIT Cambridge Limited, 2016. Accessed: Mar. 07, 2023. [Online]. Available: https://www.amazon.com/Solar-Energy-Engineering-Photovoltaic-Technologies/dp/1906860327

[10] A. Goodrich *et al.*, "A wafer-based monocrystalline silicon photovoltaics road map: Utilizing known technology improvement opportunities for further reductions in manufacturing costs," *Sol. Energy Mater. Sol. Cells*, vol. 114, pp. 110–135, Jul. 2013, doi: 10.1016/j.solmat.2013.01.030.

[11] M. K. Hossain, "Hydrogenated Amorphous Silicon-Based Thin Film Solar Cell: Optical, Electrical and Structural Properties," *Adv. Mater. Res.*, vol. 1116, pp. 59–64, Jul. 2015, doi: 10.4028/www.scientific.net/AMR.1116.59.

[12] "Thin-Film Silicon Solar Cells," in *McEvoy's Handbook of Photovoltaics*, Academic Press, 2018, pp. 235–307. doi: 10.1016/B978-0-12-809921-6.00008-2.

[13] O. Vetterl *et al.*, "Intrinsic microcrystalline silicon: A new material for photovoltaics," *Sol. Energy Mater. Sol. Cells*, vol. 62, no. 1, pp. 97–108, Apr. 2000, doi: 10.1016/S0927-0248(99)00140-3.

[14] S. N. Agbo, J. Krč, R. A. C. M. M. van Swaaij, and M. Zeman, "Optimization of the p–i interface properties in thin film microcrystalline silicon solar cell," *Sol. Energy Mater. Sol. Cells*, vol. 94, no. 11, pp. 1864–1868, Nov. 2010, doi: 10.1016/j.solmat.2010.06.034.

[15] L. A. Chow, “Chapter 9 - Equipment and Manufacturability Issues in Chemical Vapor Deposition Processes,” in *Handbook of Thin Film Deposition (Fourth Edition)*, K. Seshan and D. Schepis, Eds., William Andrew Publishing, 2018, pp. 269–316. doi: 10.1016/B978-0-12-812311-9.00009-8.

[16] P. Babal, “Doped nanocrystalline silicon oxide for use as (intermediate) reflecting layers in thin-film silicon solar cells,” 2014, Accessed: Aug. 09, 2023. [Online]. Available: https://repository.tudelft.nl/islandora/object/uuid%3A448b63f4-2128-409e-bbd8-866e720116ed

[17] P. Roca i Cabarrocas, “Deposition Techniques and Processes Involved in the Growth of Amorphous and Microcrystalline Silicon Thin Films,” in *Physics and Technology of Amorphous-Crystalline Heterostructure Silicon Solar Cells*, W. G. J. H. M. van Sark, L. Korte, and F. Roca, Eds., in Engineering Materials. Berlin, Heidelberg: Springer, 2012, pp. 131–160. doi: 10.1007/978-3-642-22275-7_5.

[18] T. Doi, I. D. Marinescu, and S. Kurokawa, Eds., “Chapter 5 - Promising Future Processing Technology,” in *Advances in CMP Polishing Technologies*, Oxford: William Andrew Publishing, 2012, pp. 229–295. doi: 10.1016/B978-1-4377-7859-5.00005-3.

[19] “Illuminated J-V - Setup and Measurement,” *TU Delft OCW*. https://ocw.tudelft.nl/course-lectures/illuminated-j-v-setup-and-measurement/ (accessed Aug. 09, 2023).

[20] *External Quantum Efficiency*, (Jan. 03, 2021). Accessed: Aug. 09, 2023. [Online Video]. Available: https://www.youtube.com/watch?v=2FTsetJQIto

[21] “Scanning Electron Microscopy - Nanoscience Instruments.” https://www.nanoscience.com/techniques/scanning-electron-microscopy/ (accessed Apr. 26, 2023).

[22] C. Yuan *et al.*, “Stable Indium Tin Oxide with High Mobility,” *ACS Appl. Mater. Interfaces*, vol. 14, no. 44, pp. 49937–49944, Nov. 2022, doi: 10.1021/acsami.2c13312.

[23] T. Koida, H. Fujiwara, and M. Kondo, “Reduction of Optical Loss in Hydrogenated Amorphous Silicon/Crystalline Silicon Heterojunction Solar Cells by High-Mobility Hydrogen-Doped In2O3 Transparent Conductive Oxide,” *Appl. Phys. Express*, vol. 1, no. 4, p. 041501, Mar. 2008, doi: 10.1143/APEX.1.041501.

[24] M. Khelil, S. Kraiem, K. Khirouni, and S. Alaya, “Growth of crystalline silicon by a seed layer approach using plasma enhanced chemical vapor deposition,” *Phys. B Condens. Matter*, vol. 609, p. 412817, May 2021, doi: 10.1016/j.physb.2021.412817.

[25] M. N. van den Donker *et al.*, “Hidden parameters in the plasma deposition of microcrystalline silicon solar cells,” *J. Mater. Res.*, vol. 22, no. 7, pp. 1767–1774, Jul. 2007, doi: 10.1557/jmr.2007.0226.

[26] S. Peng, D. Wang, F. Yang, Z. Wang, and F. Ma, “Grown Low-Temperature Microcrystalline Silicon Thin Film by VHF PECVD for Thin Films Solar Cell,” *J. Nanomater.*, vol. 2015, Mar. 2015, doi: 10.1155/2015/327596.

[27] G. Yang, “High-efficient n-i-p thin-film silicon solar cells,” 2015, Accessed: May 25, 2023. [Online]. Available: https://repository.tudelft.nl/islandora/object/uuid%3A50a4a249-3373-48b4-90b9-5ed2b7098579

[28] M. Criel, “The art of texturing glass for Photovoltaics: Processing and optical characterisation,” 2023, Accessed: Jul. 06, 2023. [Online]. Available: https://repository.tudelft.nl/islandora/object/uuid%3Acf52ba61-201b-4869-a03c-09a25294af4c

[29] H. Tan *et al.*, “Highly transparent modulated surface textured front electrodes for high-efficiency multijunction thin-film silicon solar cells,” *Prog. Photovolt. Res. Appl.*, vol. 23, no. 8, pp. 949–963, 2015, doi: 10.1002/pip.2639.

[30] G. Yang, R. A. C. M. M. van Swaaij, H. Tan, O. Isabella, and M. Zeman, “Modulated surface textured glass as substrate for high efficiency microcrystalline silicon solar cells,” *Sol. Energy Mater. Sol. Cells*, vol. 133, pp. 156–162, Feb. 2015, doi: 10.1016/j.solmat.2014.11.013.

[31] R. Leach, *Fundamental Principles of Engineering Nanometrology, second edition*. 2014.

[32] P. Bühlmann, A. Billet, J. Bailat, and C. Ballif, “Anti-reflection layer at the TCO/Si interface for high efficiency thin-film solar cells deposited on rough LP-CVD front ZnO,” *Proc 22nd Eur. Photovolt. Sol. Energy Conf Exhib.*, Jan. 2007.

[33] G. H. Wang *et al.*, “Improved aluminum-doped ZnO/metal back reflector for p-i-n amorphous silicon germanium thin film solar cells,” *Thin Solid Films*, vol. 534, pp. 591–593, May 2013, doi: 10.1016/j.tsf.2013.01.059.

[34] G. Yue, L. Sivec, J. M. Owens, B. Yan, J. Yang, and S. Guha, “Optimization of back reflector for high efficiency hydrogenated nanocrystalline silicon solar cells,” *Appl. Phys. Lett.*, vol. 95, no. 26, p. 263501, Dec. 2009, doi: 10.1063/1.3279143.

[35] D. Raoufi and T. Raoufi, “The effect of heat treatment on the physical properties of sol–gel derived ZnO thin films,” *Appl. Surf. Sci.*, vol. 255, no. 11, pp. 5812–5817, Mar. 2009, doi: 10.1016/j.apsusc.2009.01.010.

[36] E. Moulin, U. Paetzold, H. Siekmann, J. Worbs, A. Bauer, and R. Carius, “Study of thin-film silicon solar cell back reflectors and potential of detached reflectors,” *Energy Procedia*, vol. 10, pp. 106–110, Dec. 2011, doi: 10.1016/j.egypro.2011.10.161.

[37] A. Janotti and C. G. V. de Walle, “Fundamentals of zinc oxide as a semiconductor,” *Rep. Prog. Phys.*, vol. 72, no. 12, p. 126501, Oct. 2009, doi: 10.1088/0034-4885/72/12/126501.

[38] D. Ananthanarayanan, J. J. Diaz Leon, J. Wong, S. Nicolay, A. G. Aberle, and J. W. Ho, “Mid-infrared characterization and modelling of transparent conductive oxides,” *Sol. Energy*, vol. 209, pp. 424–430, Oct. 2020, doi: 10.1016/j.solener.2020.09.020.

[39] P. Kalpoe, “Transparent conductive oxide bi-layer as front contact for multijunction thin film silicon photovoltaic cells,” 2023, Accessed: Jul. 19, 2023. [Online]. Available: https://repository.tudelft.nl/islandora/object/uuid%3Af487531b-685f-4f2a-b59e-cd66ae7082ed

[40] W. Böttler, V. Smirnov, A. Lambertz, J. Hüpkes, and F. Finger, “Front and Back Contacts for Microcrystalline Silicon Solar Cells in n-i-p Configuration,” Jan. 2010, pp. 3060–3063. doi: 10.4229/25thEUPVSEC2010-3AV.1.64.

Appendix

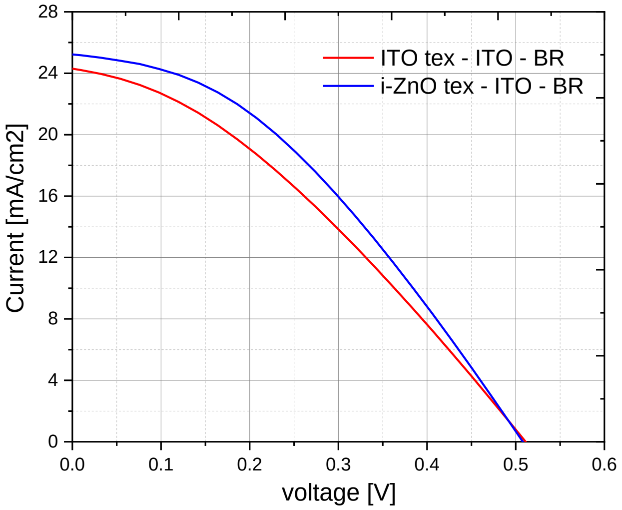

Figure 55 J-V plots of single junction nc-Si:H samples with ITO and i-ZnO sacrificial texturing

Table 25 J-V plots of single junction nc-Si:H samples with ITO and i-ZnO sacrificial texturing

	ITO	i-ZnO
Voc [V]	0.51	0.5
Jsc EQE [mA/cm²]	24.3	25.2
Roc [ohm·cm²]	36.9	45.3
Rsc [ohm·cm²]	281	372
FF [-]	0.33	0.36
η[%]	4.09	4.54

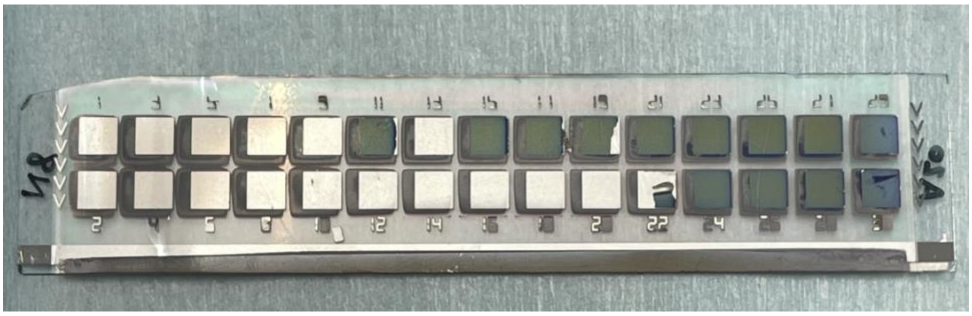

Figure 56 Over etched solar cell sample with damaged metal back reflector due to improper control over dry etching